

# Dynamical Systems Analysis of Intrinsic Excitability of Neural Cells

**Jakub Nowacki**

Department of Engineering Mathematics  
University of Bristol



A dissertation submitted to the University of Bristol in  
accordance with the requirements of the degree of  
Doctor of Philosophy in the Faculty of Engineering.

March 2012

Word count: 32,253



## Abstract

In this thesis we use tools provided by dynamical systems theory to analyse transient behaviour of neural cells. We study models in Hodgkin-Huxley formalism that have a natural time-scale separation, which allows us to apply concepts of geometrical singular perturbation theory. The analysis presented in this thesis is applied to physiologically-realistic models represented by high-dimensional systems with multiple time scales.

We construct a model of hippocampal pyramidal neurons and study after-depolarisation (ADP), which is a hallmark of excitability and precursor of transient bursting. Through careful analysis of the model we investigate the contribution of particular ionic currents to the excitability behaviour of the model. Furthermore using model simulations and experimental data we define ADP mathematically. Based on the essence of ADP and transient bursting we perform a reduction of the model, which enables an in-depth study of these phenomena. To understand spike adding during transient bursting we use a two-point boundary value formulation of the model, inspired by the experimental protocol. We show that the spikes are added through a canard-like transition, during which the orbit segment traces unstable sheets of a critical manifold up to a jump point. Our analysis suggests at least two mechanisms of spike adding: one is organised by a fold of the critical manifold and the other due to the presence of an additional unstable equilibria of the full system. The results of this study extend the definition of an excitability threshold and show that spikes can be added through a continuous deformation of an orbit segment, not by a discontinuous abrupt process.

We also apply the ideas of geometrical singular perturbation theory to study periodic bursting in a pituitary cell model. We use nullclines to investigate the nature of plateau bursting taking place below the branch of attracting equilibria in the fast subsystem. Moreover, we continue orbit segments in order to compute the stable manifolds of the branch of saddle equilibria, which plays a role of separatrix in this system. We show that seemingly premature termination of the active phase of the plateau burst is related to the orbit crossing this separatrix before reaching the end of the stable equilibrium branch.

Finally, we use numerical continuation to compute onsets of ADP and a spike in transient bursting. We show that these onsets correspond to extrema of slow variables of the full system. In our boundary value problem formation the onsets are detected as folds, which allows further continuation in two parameters to establish the boundaries of different model behaviours. This new technique is a form of parameter sensitivity analysis and, in principle, could be applied to other models.



## Acknowledgements

I would like to express my sincere gratitude to my PhD supervisors Prof Hinke Osinga and Dr Krasimira Tsaneva-Atanasova for their continuous support, patience and motivation to perform at my best. This thesis would not see the light of day without their guidance. I sincerely thank them for leading an engineer into the world of nonlinear dynamics and mathematical biology.

I wish to thank Prof Andrew Randall and members of his lab, especially Dr Jon Brown, for sharing their knowledge of neuroscience with me. Their generous assistance and productive scientific discussion greatly helped and shaped my understanding of the experimental sciences.

My appreciation goes to all current and past members of the Applied Nonlinear Mathematics group for creating an excellent working environment. The group provided me with a rare opportunity to apply mathematics to real-world problems and created a stimulating research environment.

Last but not least, I would like to thank my whole family for their support and confidence in me. Most of all, I would like to thank my wife Ewa and son Victor, for their patience and understanding during many turbulent times.



*“That’s mortals for you, Death continued. They’ve only got a few years in this world and they spend them all in making things complicated for themselves.”*

**Death in Mort (1987), Terry Pratchett.**



### **Author's Declaration**

I declare that the work in this dissertation was carried out in accordance with the regulations of the University of Bristol. The work is original except where indicated by special reference in the text and no part of the dissertation has been submitted for any other degree.

Any views expressed in the dissertation are those of the author and in no way represent those of the University of Bristol.

The dissertation has not been presented to any other University for examination either in the United Kingdom or overseas.

Signed:

Dated:



# Contents

<b>1</b>	<b>Introduction</b>	<b>1</b>
1.1	Excitability in neural cells . . . . .	1
1.1.1	Spiking and bursting . . . . .	2
1.1.2	Hodgkin-Huxley formalism . . . . .	4
1.2	Bifurcation analysis of slow-fast systems . . . . .	9
1.3	Transient bursting mechanisms . . . . .	12
1.4	Numerical methods and tools . . . . .	17
<b>2</b>	<b>A unified model of CA1/3 pyramidal cells: An investigation into excitability</b>	<b>19</b>
2.1	Background . . . . .	19
2.2	General single-compartment model for CA pyramidal neuron cells . . . . .	22
2.3	Model validation . . . . .	24
2.3.1	Long-stimulus experiment . . . . .	25
2.3.2	Short-stimulus experiment . . . . .	28
2.4	Excitability sensitivity analysis of the pyramidal neuron model . . . . .	30
2.4.1	Methods . . . . .	30
2.4.2	The $\text{Na}^+$ -channel currents . . . . .	31
2.4.3	The $\text{Ca}^{2+}$ -channel currents . . . . .	34
2.4.4	The $\text{K}^+$ -channel currents . . . . .	36
2.5	Identification of after-depolarisation and the initial burst . . . . .	38
2.5.1	Mathematical formulation of after-depolarisation . . . . .	38
2.5.2	The role of different ionic currents in shaping the after-depolarisation .	42
2.5.3	After-depolarisation and CA1/3 neural excitability . . . . .	44
2.6	Conclusion . . . . .	45
<b>3</b>	<b>The role of large-conductance Calcium-activated K<sup>+</sup> (BK) channels in shaping bursting oscillations of a somatotroph cell model</b>	<b>47</b>
3.1	Background . . . . .	47
3.2	The model . . . . .	48
3.3	Analysis of the model using the fast subsystem . . . . .	49

3.4	Oscillations during the active phase . . . . .	53
3.5	The end of the active phase . . . . .	55
3.6	Conclusion . . . . .	59
<b>4</b>	<b>Dynamical systems analysis of spike-adding mechanisms in transient bursts</b>	<b>61</b>
4.1	The model . . . . .	61
4.2	Identifying the spike-adding mechanism . . . . .	65
4.3	Spike adding organised by the critical manifold . . . . .	69
4.3.1	Slow flow on the critical manifold near $F_3$ . . . . .	75
4.3.2	Slow flow of the critical manifold near the folds $F_1$ and $F_2$ . . . . .	78
4.3.3	Spike adding when additional equilibria are present . . . . .	81
4.4	Conclusion . . . . .	83
<b>5</b>	<b>Continuation-based numerical analysis of after-depolarisation and spike-adding threshold</b>	<b>85</b>
5.1	ADP as a boundary value problem . . . . .	85
5.2	Identifying the onset of a spike in a transient burst . . . . .	89
5.3	Establishing the regions of model behaviour . . . . .	93
5.4	Conclusion . . . . .	98
<b>6</b>	<b>Conclusion and outlook</b>	<b>99</b>
6.1	Summary . . . . .	99
6.2	Future work . . . . .	100
<b>A</b>	<b>Summary of pituitary cell model equations</b>	<b>103</b>

# List of Tables

2.1	Parameter values of the pyramidal neuron model. . . . .	24
2.2	Maximal conductances (in $\text{mS}/\text{cm}^2$ ) used when modelling a CA1 or a CA3 neuron. . . . .	26
4.1	Parameter values for the simplified model (4.1) as defined in (4.2)–(4.4). . . . .	63
4.2	Overview of the different sheets and stability properties of the critical manifold $S$ and the manifold $P$ of periodic orbits for the simplified model (4.1), with $g_{\text{SI}} = 0.5615 \text{ mS}/\text{cm}^2$ ; the number of sheets, as well as their stability, does not change for any of the other choices of $g_{\text{SI}}$ considered in this chapter. . . . .	70
A.1	Parameter values used in the simulations. . . . .	104



# List of Figures

1.1	Example of spiking and bursting behaviour of a hippocampal pyramidal neuron; the time series of the membrane potential is shown in blue; the spike threshold of 20 V/s is shown in red and is different for every spike. . . . .	3
1.2	Example of steady-state (in)activation functions of a T-type $\text{Ca}^{2+}$ -current; the points are obtained from the voltage-clamp experiments and labelled with dots of the respective colours; the error bars indicate the standard deviation of the measurements; the activation and inactivation curves in the form of Boltzmann function fitted to the voltage clamp measurements are depicted in blue and red, respectively. . . . .	6
1.3	Example of spike in the Hodgkin-Huxley model (1.1)-(1.4); panel (a) shows the time trace of the responses of the membrane potential of the model to a brief current injection of 5, 6 and 7 $\mu\text{A}/\text{cm}^2$ depicted with the respective blue-gradient curves; panel (b) shows the time trace of the injected current. . . . .	8
1.4	Examples of periodic and transient bursting with the underlying critical manifold obtained from the bifurcation analysis of the fast subsystem, where the slow variable is a parameter; the branches of stable and unstable equilibria are coloured with black and red, respectively; the maximal and minimal values of stable and unstable families of periodic orbits are coloured with blue and magenta, respectively; fold and Hopf bifurcations are marked with labelled dots; panel (a) shows a trajectory of a periodic burst (grey) overlaid on the bifurcation diagram; panel (b) shows a trajectory of a transient burst overlaid on the bifurcation diagram with (light-grey) and without current injection (grey); panels (c) and (d) show time series of the trajectories of periodic and transient bursts, respectively. . . . .	13

- 2.1 Electrophysiological differences between CA1- and CA3-area neurons; in a long-stimulus experiment 100 pA current is injected into a cell for 500 ms; in a short-stimulus experiment 2 nA current is injected into a cell for 2 ms; panels (a) and (b) show the typical responses of a CA3-area neuron to long and short stimuli, respectively; similarly, panels (c) and (d) show the typical responses of a CA1-area neuron to these two stimuli, respectively; panels (e) and (f) show the time traces of the injected current for the long- and a short-stimulus experiments, respectively. All experiments were performed in a submerged recording chamber maintained at  $32 \pm 1^\circ\text{C}$ , perfused with an artificial cerebrospinal fluid. The synaptic transmission was blocked pharmacologically without the truncation of the dendrites; see (Brown and Randall, 2009) for details on these methods. . . . . 20
- 2.2 Channel kinetics used in the pyramidal neuron model; panels (a), (b) and (c) show (in)activation functions of  $\text{Na}^+$ -,  $\text{Ca}^{2+}$ - and  $\text{K}^+$ -channel currents, respectively; experimental measurements used to determine  $\text{Na}^+$ -current (in)activation parameters are depicted as blue dots in panel (a) with standard deviations marked by the error bars; panel (d) shows the time rate of the transient  $\text{Na}^+$ -channel. . . . . 25
- 2.3 Responses of a CA3 pyramidal neuron and our model to a 500 ms current injection; panel (a) shows experimental responses of a pyramidal cell, where the injected current has amplitudes 100, 200 and 300 pA; panel (b) shows the corresponding responses of the model to 1, 2 and  $3 \mu\text{A}/\text{cm}^2$  of injected current. 26
- 2.4 Responses of a CA1 pyramidal neuron and our model to a 500 ms current injection; panel (a) shows experimental responses of a pyramidal cell, where the injected current has amplitudes 100, 200 and 300 pA; panel (b) shows the corresponding responses of the model to 1, 2 and  $3 \mu\text{A}/\text{cm}^2$  of injected current. 27
- 2.5 Responses of the pyramidal neuron model to a 2 ms current injection of  $20 \mu\text{A}/\text{cm}^2$ ; panel (a) shows overlaid responses of the model with the CA3 parameter set to a stimulus with different (pre-stimulating) base currents, namely,  $0 \mu\text{A}/\text{cm}^2$  (blue),  $0.4 \mu\text{A}/\text{cm}^2$  (green) and  $0.8 \mu\text{A}/\text{cm}^2$  (red); similarly, panel (b) shows overlaid responses of the model with the CA1 parameter set to those same stimuli. . . . . 29
- 2.6 Sensitivity analysis of the maximal conductances of the  $\text{Na}^+$ -currents; panels (a) and (c) show the excitability measure for the ranges of  $g_{\text{Na}_T}$  and  $g_{\text{Na}_P}$  where the model produces an eight-spike response, respectively; panels (b) and (d) show the numbers of spikes in a spike train for  $g_{\text{Na}_T}$  and  $g_{\text{Na}_P}$ , respectively; the original values of the maximal conductances are marked by a (magenta) star. . . . . 32

2.7 Sensitivity analysis of the maximal conductance of the combined $\text{Na}^+$ -currents; panel (a) shows the excitability measure ranging over the given percentages of $g_{\text{Na}}$ ; the original value of the maximal conductance is marked by a (magenta) star. . . . .	33
2.8 Sensitivity analysis of the maximal conductances of the $\text{Ca}^{2+}$ -currents; panels (a) and (c) show the excitability measure for the ranges of $g_{\text{Ca}_T}$ and $g_{\text{Ca}_H}$ where the model produces an eight-spike response, respectively; panels (b) and (d) show the numbers of spikes in a spike train for $g_{\text{Ca}_T}$ and $g_{\text{Ca}_H}$ , respectively; the original values of the maximal conductances are marked by a (magenta) star. . . . .	34
2.9 Sensitivity analysis of the maximal conductances of the $\text{K}^+$ -currents; panels (a) and (c) show the excitability measure for the ranges of $g_{\text{K}_{\text{DR}}}$ and $g_{\text{K}_{\text{M}}}$ where the model produces an eight-spike response, respectively; panels (b) and (d) show the number of spikes in a spike train for $g_{\text{K}_{\text{DR}}}$ and $g_{\text{K}_{\text{M}}}$ , respectively; the original values of the maximal conductances are marked by a (magenta) star. . . . .	37
2.10 ADP in a CA3 pyramidal neuron for the model (first column) and the experiment (second column); panel (a) shows the time series of $V$ for the model with a holding current of $0.4 \mu\text{A}/\text{cm}^2$ ; panel (b) shows the time series of $V$ for an experimental sweep; panels (c) and (d) show the membrane potential $V$ versus $dV/dt$ ; the dashed line marks $dV/dt = 0$ ; panels (e) and (f) show an enlargement of the ADP region, with the beginning $B$ and peak $P$ of the ADP marked for the model in panel (e). . . . .	39
2.11 Bursting-threshold of the pyramidal neuron model; panel (a) shows trajectory segments of ADP without (blue) and with (green) a secondary spike in $(d^2V/dt^2, dV/dt, V)$ -space; the intersections of the trajectory segments with the planes $dV/dt = 0$ (cyan) and $d^2V/dt^2 = 0$ (red) are marked by dots and stars, respectively; panel (b) presents a top view, namely, the projection onto the $(dV/dt, d^2V/dt^2)$ -plane, with the projections of $dV/dt = 0$ (cyan) and $d^2V/dt^2 = 0$ (red) represented by dashed lines; panel (c) shows the time traces of the two trajectories. . . . .	41
2.12 The relation between inward and outward currents in the model during the ADP. Panel (a) shows a detailed view of the ADP from the time trace shown in Figure 2.10(a), with the beginning and the peak of ADP labelled as $B$ and $P$ , respectively. Panel (b) shows the time traces of the absolute values of the total inward (green) and outward (red) current presented on a $\log_2$ -scale. Vertical dashed (black) lines in panels (a) and (b) indicate the times $t_B$ and $t_P$ , respectively. . . . .	43

- 3.1 Bursting oscillations in system (3.1)–(3.3) with  $b_{BK} = 0$ . Panel (a) shows the periodic dynamics of  $V_m$  (blue) and  $c$  (red) versus time. One active phase is marked by black dashed lines. Panel (b) shows this same periodic orbit  $\Gamma$  (black) overlaid on the bifurcation diagram of the fast subsystem in the  $(c, V_m)$ -plane. The solid blue curves are branches of stable equilibria; the dashed green line consists of saddle equilibria; dashed red lines show the maxima and minima of the family of unstable periodic orbits that arises from the Hopf bifurcation point labeled H; this family ends in a homoclinic bifurcation marked HC; labels  $SN_L$  and  $SN_H$  indicate saddle-node bifurcations. . . . . 50
- 3.2 Bursting oscillations in system (3.1)–(3.3) with  $b_{BK} = 0.15$ . Panel (a) shows the periodic dynamics of  $V_m$  (blue) and  $c$  (red) versus time. One active phase is marked by black dashed lines. Panel (b) shows this same periodic orbit  $\Gamma$  (black) overlaid on the bifurcation diagram of the fast subsystem in the  $(c, V_m)$ -plane. The solid blue curves are branches of stable equilibria; the dashed green line consists of saddle equilibria; dashed red lines show the maxima and minima of the family of unstable periodic orbits that arises from the Hopf bifurcation point labelled H; this family ends in a homoclinic bifurcation marked HC; labels  $SN_L$  and  $SN_H$  indicate saddle-node bifurcations. . . . . 51
- 3.3 Eigenvalues of the fast subsystem with  $b_{BK} = 0$  (left column) and  $b_{BK} = 0.15$  (right column) as a function of  $V_m$  along the Z-shaped branch of equilibria  $e_L$ ,  $e_M$  and  $e_H$ ; panels (a) and (c) show the real parts and panels (b) and (d) the imaginary parts of the eigenvalues; the dotted vertical lines mark the bifurcation points  $SN_L$ ,  $SN_H$  and H, respectively. . . . . 52
- 3.4 Three-dimensional view of one oscillation of  $\Gamma$  during the active phase for  $b_{BK} = 0$  (a) and  $b_{BK} = 0.15$  (b). The two panels show how  $\Gamma$  (red) interacts with the  $V_m$ -nullcline surface (green to yellow gradient). The blue cloud of points are trajectories of the frozen system starting on  $\Gamma$  for different values of  $c$ ; all these trajectories converge to the family  $e_H$  (blue curve) on the  $V_m$ -nullcline. 53
- 3.5 Behaviour of trajectories of the fast subsystem with  $b_{BK} = 0$  starting at initial values  $\gamma_c$  (red dots) along the active phase of  $\Gamma$  for  $c = 0.541 \mu\text{M}$ ,  $c = 0.559 \mu\text{M}$  and  $c = 0.578 \mu\text{M}$ , where  $\gamma_c$  lies to the right of, precisely on, and to the left of the  $V_m$ -nullcline (green), respectively. . . . . 54
- 3.6 The active phase of  $\Gamma$  past the first overshoot for  $b_{BK} = 0$  (red curve) and  $b_{BK} = 0.15$  (cyan curve) plotted in  $(\dot{V}_m, \dot{n}_{dr}, c)$ -space (a) along with projections onto the  $(c, \dot{V}_m)$ - and  $(c, \dot{n}_{dr})$ -planes in panels (b) and (c), respectively. The nullclines  $\dot{V}_m = 0$  (green horizontal plane) and  $\dot{n}_{dr} = 0$  (blue vertical plane) in panel (a) project to the dashed lines in panels (b) and (c), respectively. 56

---

3.7	The value of $\dot{n}_{dr}$ at the peak of the second oscillation in the active phase of $\Gamma$ as a function of $b_{BK} \in [0, 0.15]$ . The crossing at $\dot{n}_{dr} = 0$ marks the transition from oscillations below $e_H$ to oscillations around $e_H$ in system (3.1)–(3.3). . . . .	57
3.8	Bursting oscillations in system (3.1)–(3.3) with $b_{BK} = 0.07$ . Panel (a) shows the periodic dynamics of $V_m$ (blue) and $c$ (red) versus time. Panel (b) shows this same periodic orbit $\Gamma$ (black) overlaid on the bifurcation diagram of the fast subsystem in the $(c, V_m)$ -plane. The solid blue curves are branches of stable equilibria; the dashed green line consists of saddle equilibria; dashed red lines show the maxima and minima of the family of unstable periodic orbits that arises from the Hopf bifurcation point labelled H; this family ends in a homoclinic bifurcation marked HC; labels $SN_L$ and $SN_H$ indicate saddle-node bifurcations. . . . .	57
3.9	The $c$ -dependent family $W^s(e_M)$ of one-dimensional stable manifolds of the saddle points along $e_M$ in between $SN_L$ and HC. Panel (a) shows the manifold for $b_{BK} = 0$ and panel (b) for $b_{BK} = 0.15$ along with the family $e_M$ of saddle equilibria (green dashed line). The manifold $W^s(e_M)$ is shown as a blue gradient surface with two solid (blue) lines marking the bounding manifolds at $SN_L$ and HC. The orbit $\Gamma$ is depicted as a solid (red) curve. . . . .	58
4.1	Responses of system (4.1) to a current injection of $I_{app} = 20\mu\text{A}/\text{cm}^2$ from $t = 20$ to $t = 23$ ; overlaid are the responses corresponding to different values of the maximal conductance $g_{SI}$ (in $\text{mS}/\text{cm}^2$ ) of the slow inward current, namely, $g_{SI} = 0.1$ , $g_{SI} = 0.5$ and $g_{SI} = 0.6$ , which are examples of responses with no ADP, with ADP and a (three-spike) burst with ADP, respectively. . . . .	64
4.2	Formulation of system (4.1) as the boundary value problem (4.5)–(4.8). The first (red) segment is the solution $\mathbf{u}_{ON}(t)$ of (4.1) with $I_{app} = 20\mu\text{A}/\text{cm}^2$ and $\mathbf{u}_{ON}(0)$ is at the resting potential $\mathbf{u}_{OFF}^*$ , which is an equilibrium of (4.1) with $I_{app} = 0$ (indicated by the horizontal black dashed line); the total integration time is $T_{ON} = 3\text{ms}$ , such that one action potential occurs. The second (blue) segment is the solution $\mathbf{u}_{OFF}(t)$ of (4.1) with $I_{app} = 0$ and $\mathbf{u}_{OFF}(0) = \mathbf{u}_{ON}(1)$ ; the integration time $T_{OFF}$ is fixed to a large enough value so that $\mathbf{u}_{OFF}(1) \approx \mathbf{u}_{OFF}^*$ . . . . .	66

- 
- |  |    |
|--|----|
| 4.3 Continuation for increasing $g_{\text{SI}}$ of solutions to system (4.5)–(4.8); panel (a) shows the AUTO (Doedel, 1981; Doedel and Oldeman, 2009) $L^2$ -norm of the solution branch versus $g_{\text{SI}}$ and illustrates that the spike-adding mechanism happens suddenly via a pronounced drop in norm; panels (b)–(f) show representative solutions along the branch, indicated by the correspondingly labelled dots in panel (a), and illustrate that solutions during a spike generation, i.e., panels (c) and (d), exhibit a stretched ADP that develops into a double step before relaxing back to the resting potential. . . . .   | 67 |
| 4.4 Critical manifolds for $g_{\text{SI}} = 0.5615 \text{ mS/cm}^2$ embedded in the five-dimensional phase space of system (4.1); shown are projections onto $(h_{\text{SI}}, m_{\text{SO}}, V)$ -space of the fast subsystem of (4.1), where the slow variables $m_{\text{SO}}$ and $h_{\text{SI}}$ are treated as parameters; panels (a) and (b) show two different view points of the surfaces of equilibria, coloured black when stable and red when not; from the same view points, panels (c) and (d) also show maxima and minima with respect to $V$ of the two-parameter families of periodic orbits, coloured blue when stable and magenta when not. The equilibrium manifold splits into six sheets labelled $S_1^a$ , $S_1^r$ , $S_2^a$ , $S_2^r$ , $S_3^r$ , and $S_3^a$ , that are separated by four fold curves $F_0$ (not shown), $F_1$ , $F_2$ , and $F_3$ , and a curve of Hopf bifurcations labelled $H$ ; the saddle and attracting families of periodic orbits are labelled $P^r$ and $P^a$ , respectively. See also Table 4.2 . . . . . | 71 |
| 4.5 Orbit segments $\mathbf{u}_{\text{OFF}}(t)$ of system (4.5)–(4.8) with $g_{\text{SI}} \approx 0.5615 \text{ mS/cm}^2$ overlaid on the critical manifolds of Figure 4.4 with $g_{\text{SI}} = 0.5615 \text{ mS/cm}^2$ . The orbit segments are selected along the first downward peak in Figure 4.3(a); panel (a) shows an orbit segment just before the minimum of the peak in Figure 4.3(a) is reached; panel (b) shows one shortly after; panel (c) shows the orbit segments labelled (d) in Figure 4.3(a); and panels (d)–(f) show the spike generation as the orbit segments are continued until the start of the next ‘plateau’ in Figure 4.3(a). . . . .   | 73 |
| 4.6 Phase portraits on the sheets $S_2^r$ and $S_3^r$ of the critical manifold $S$ near the fold $F_3$ ; panel (a) shows a trajectory of the desingularised slow flow (4.11), which converges to an attracting focus on $F_3$ (grey line); panel (b) shows projected trajectories of the slow flow (4.9); the repelling and attracting nature of $F_3$ is indicated by light- and dark-green colours, respectively. . . . .  | 76 |

- 
- |  |    |
|--|----|
| 4.7 Vectors of the slow flow on $S$ near the top fold $F_3$ together with the orbit segment from Figure 4.5(c); the direction of flow on $S$ is indicated by the arrows, where hotter colours correspond to vectors with larger magnitudes. The folded focus is the black dot on $F_3$ , with the uniformly repelling and attracting parts of $F_3$ coloured light and dark green, respectively. Panels (a) and (b) show the process from two different viewpoints, and panels (c) and (d) show corresponding close-up views near $F_3$ . . . . .  | 77 |
| 4.8 Vectors of the slow flow on $S$ in the vicinity of the two folds $F_1$ and $F_2$ that mark the transition of the orbit segment between the two unstable sheets $S_1^r$ and $S_2^r$ ; the direction of flow on $S$ is indicated by the arrows, where hotter colours correspond to vectors with larger magnitudes. The attracting fold $F_1$ is dark green and the repelling fold $F_2$ is light green. Panels (a)–(c) show the same perspective with orbit segments that almost reach $F_1$ , reach $F_1$ via the attracting sheet $S_2^a$ , and reach $F_2$ with a jump from $S_1^r$ to $S_2^r$ , respectively. . . .                                    | 79 |
| 4.9 The critical manifold calculated for $g_{FO} = 9.6 \text{ mS/cm}^2$ and $g_{SI} = 0.7842 \text{ mS/cm}^2$ projected onto $(h_{SI}, m_{SO}, V)$ -space; superimposed in the left and right column are orbit segments with $g_{SI} \approx 0.7842$ selected from the falling and rising slopes of the downward peak, respectively. Panels (a) and (b) show and overall view and panels (c) and (d) enlargements near $F_1$ and $F_2$ along with the associated slow flow. The two unstable equilibria $s_1$ and $s_2$ of the full system are marked with black and red dots, because they are an attractor and a saddle on $S_1^r$ , respectively. . . . . | 82 |

- 5.1 Illustration of the formulation of ADP in system (4.1) as a boundary value problem (4.5)–(4.8) with (5.1). Panel (a) shows orbit segments  $\mathbf{u}_{\text{ON}}$  and  $\mathbf{u}_{\text{OFF}}$  as time series of  $V$ . We assume that initially the system is at the resting potential  $\mathbf{u}_{\text{OFF}}^*$ , which is an equilibrium of (4.1) with  $I_{\text{app}} = 0$  (indicated by the horizontal dashed black line). The first (red) segment is the (scaled) solution  $\mathbf{u}_{\text{ON}}(t)$  of (4.1) with  $I_{\text{app}} = 20\mu\text{A}/\text{cm}^2$  and  $\mathbf{u}_{\text{ON}}(0) = \mathbf{u}_{\text{OFF}}^*$ ; the total integration time is  $T_{\text{ON}} = 3\text{ms}$ , such that one action potential occurs (its maximum is marked by a red star). Using the scaled Equation (4.5), this segment ends at  $\mathbf{u}_{\text{ON}}(1)$ . The second (blue) segment is the (scaled) solution  $\mathbf{u}_{\text{OFF}}(t)$  of (4.1) with  $I_{\text{app}} = 0$  and  $\mathbf{u}_{\text{OFF}}(0) = \mathbf{u}_{\text{ON}}(1)$ ; the total integration time  $T_{\text{OFF}}$  is such that  $\mathbf{u}_{\text{OFF}}(t)$  exhibits a local minimum, which marks the beginning of ADP (blue star labelled B), and ends at a local maximum, marking the peak of ADP (blue star labelled P). Using the scaled Equation (4.6), this segment ends at  $\mathbf{u}_{\text{ON}}(1) = \mathbf{P}$  when the combined trajectory is integrated up to time  $T_{\text{ON}} + T_{\text{OFF}}$ . Panel (b) shows the ADP in  $(dV/dt, V)$ -projection; in this projection B and P are clearly associated with crossing the  $V$ -nullcline depicted as a dashed black line. . . . . 86
- 5.2 Continuation of system (4.5)–(4.8) with (5.1) in  $h_{\text{SI}_{\text{OFF}}}(1)$ ; panel (a) shows an enlargement of the projection onto the  $(dV/dt, V)$ -plane to illustrate that the end points lie on the  $V$ -nullcline (vertical dashed black line); panel (b) shows the solutions along the bifurcation curve, shown in panel (c), as  $h_{\text{SI}_{\text{OFF}}}(1)$  increases; panel (c) shows bifurcations diagram in the  $(g_{\text{SI}}, h_{\text{SI}_{\text{OFF}}}(1))$ -plane, with the solutions marked with blue dots; the onset of ADP, which is a fold of the bifurcation curve, is the blue star. . . . . 88
- 5.3 Continuation for increasing  $g_{\text{SI}}$  of solutions to system (4.5)–(4.8) with  $T_{\text{OFF}} = 297\text{ ms}$  fixed; panel (a) shows the AUTO (Doedel, 1981; Doedel and Olde-man, 2009)  $L^2$ -norm of the solution branch versus  $g_{\text{SI}}$  and illustrates that the spike-adding mechanism happens suddenly via a pronounced drop in norm; panels (b)–(f) show representative solutions along the branch, indicated by the correspondingly labelled dots in panel (a), and illustrate that solutions during a spike generation exhibit a long plateau before relaxing back to the resting potential; the time trace below  $V$  is the corresponding trace of  $h_{\text{SI}}$ , which has a minimal value that corresponds with the peak of ADP. . . . . 91
- 5.4 Continuation to find extrema of  $h_{\text{SI}_{\text{OFF}}}(1)$ ; panel (a) shows the time series of the solutions; thick lines curves correspond to the extrema of  $h_{\text{SI}_{\text{OFF}}}(1)$ ; panel (b) and (c) show  $h_{\text{SI}_{\text{OFF}}}(1)$  versus  $g_{\text{SI}}$  and  $h_{\text{SI}_{\text{OFF}}}(1)$  versus  $V_{\text{OFF}}(1)$ , respectively; consequent solutions of the continuation are marked with dots (regular solutions) and stars (extrema of  $h_{\text{SI}_{\text{OFF}}}(1)$ ). . . . . 93





# Outline

This thesis consists of 5 chapters:

**Chapter 1** gives a general introduction to excitability of neural cells. Here we explain the use of mathematical models in Hodgkin-Huxley formalism to characterise spiking and bursting. Furthermore, this chapter gives a general introduction to slow-fast systems and the application of bifurcation analysis.

**Chapter 2** presents a study of after-depolarisation using a single-compartment pyramidal-cell model based on recent voltage- and current-clamp experimental data. We use model analysis to define after-depolarisation and bursting threshold. We also explain the influence of particular ionic currents on this phenomenon. This study has been published in (Nowacki et al., 2011a).

**Chapter 3** explains how the slow-fast analysis can be applied to a pituitary cell model. We show that slow-fast analysis of a dynamical system with a single slow variable can successfully explain changes in the duration of a pseudo-plateau burst. This study has been published in (Nowacki et al., 2010).

**Chapter 4** contains a dynamical systems analysis of spike adding in transient bursts on top of the after-depolarisation. We consider a simplified five-dimensional model with two slow variables and study the critical manifold of the fast subsystem. We show that the spikes are added in a canard-like phenomenon. The results from this chapter have been submitted for publication (Nowacki et al., 2011b)

**Chapter 5** presents a continuation-based numerical analysis of the onset of ADP and a spike. We use our results for the spike-adding process presented in Chapter 4 and formulate the onsets as extrema of a slow variable. This idea allows us to detect them as folds in a one-parameter continuation. Moreover, the fold points can be continued in two-parameters to establish regions of different model behaviours. The work is being prepared for publication.



# Chapter 1

## Introduction

### 1.1 Excitability in neural cells

*Excitability* is the ability of a system to produce large responses as a result of small perturbation (Ermentrout and Terman, 2010; Izhikevich, 2006; Keener and Sneyd, 2009). Such behaviour has been reported to occur in many physical systems, such as lasers (Krauskopf et al., 2003; Wieczorek et al., 1999, 2002), electronic circuits (Douglas et al., 1995; Guckenheimer et al., 2003; Indiveri et al., 2011; Nagumo and Arimoto, 1962), chemical reactions (Brøns and Bar-Eli, 1991; Keener and Sneyd, 2009) and many types of cells (Ermentrout and Terman, 2010; Fitzhugh, 1961; Hodgkin and Huxley, 1952; Izhikevich, 2006; Keener and Sneyd, 2009). In this thesis we focus on the excitability of neural cells, that is pivotal for brain function.

Intrinsic excitability of a neural cell together with synaptic transmission and network behaviours comprise the fundamental building blocks of neurophysiology (Andersen et al., 2007; Izhikevich, 2006). In neural cells the excitability manifests itself through so-called *action potentials* or *spikes*. A spike is a large excursion of the membrane potential after a sufficiently strong stimulus, before it returns to an equilibrium, which corresponds to the resting potential of the cell. This behaviour is caused by a perturbation in the ionic balance between the inside and the outside of the cell membrane and is regulated by ion channels (Keener and Sneyd, 2009). *Ion channels* are large transmittance proteins through which ions can flow down their electrochemical gradient (Izhikevich, 2006).

The firing patterns of the neural cells are believed to be essential for information exchange in the brain. Namely, the changes of firing patterns in neural cells are a common and important feature associated with a variety of brain functions (Llinás, 1988). Many neurons under various conditions tend to fire *bursts*, i.e., clusters of high-frequency spikes (Krahe and Gabbiani, 2004). In particular, the bursting activity is characterised by slow alterations between nearly steady-state behaviour, the so-called silent phase, and the active phase when clusters of spikes are generated (Rinzel, 1987). A burst is fired in response to a stimulus, which

can be electrical (Brown and Randall, 2009; Yue and Yaari, 2004) or chemical (Rinzel, 1985; Tsaneva-Atanasova et al., 2007) and occurs periodically or as a single event. Bursts play an important role in many phenomena, namely, synaptic plasticity (Thomas et al., 1998), transmission of stimulus-related information (Krahe and Gabbiani, 2004) or sensory system function (Martinez-Conde et al., 2002). The bursting behaviour is not only limited to controlled in-vitro experiments, it has been also reported to occur in-vivo. For instance, spiking and bursting behaviour has been documented in in-vivo recordings from a single place cell (Epsztein et al., 2011; Harvey et al., 2009; Lee et al., 2006). In addition, changes in excitability are reported to take place in pathological conditions such as epilepsy (McCormick and Contreras, 2001) and Alzheimer's disease (Brown et al., 2011).

Even relatively small changes in biophysical properties of neurons (Brown and Randall, 2009; Brown et al., 2011) or their morphology (van Elburg and van Ooyen, 2010) can have a large impact on the neuron's excitability. Therefore, understanding the question how spikes, single or organised in burst, are fired is among the most fundamental question in neuroscience (Izhikevich, 2006). Many current studies, including the aforementioned, embrace the importance of the spike firing patterns, and thus, intrinsic excitability of the brain function in physiological as well as pathological conditions. In this thesis we study intrinsic excitability of neural cells using tools provided by dynamical systems theory. We show that mathematical and numerical analysis of the models not only aid understanding of the physical properties of neural cells, but can also provide useful predictions that can be tested in experimental studies. From the mathematical point of view, neural cell models exhibit a variety of different nonlinear behaviours. Therefore, they form an interesting object for studying novel excitable behaviours and their mathematical basis.

### 1.1.1 Spiking and bursting

We begin by explaining spiking and bursting in more detail. Figure 1.1 shows an example of spiking behaviour of a hippocampal pyramidal neuron in response to a 500 ms current injection of 200 pA (the data were obtained from Prof Randall's group University of Bristol). As illustrated in Figure 1.1, a current injection perturbs the neuron from its stable equilibrium, called *resting potential*, and causes a series of spikes. Typically for hippocampal pyramidal neurons, the initial spikes are clustered together, which is an example of *a burst* (sometimes referred to as *an initial burst*). Later spikes are fired relatively regularly; this behaviour is called *periodic* or *tonic spiking*. In some cases, bursts of spikes can also be fired periodically. The spiking behaviour ends with the end of the current injection and the neuron's membrane potential returns to its resting state.

As shown in Figure 1.1, when the perturbation is sufficiently strong, a spike or burst is fired. The minimal value of displacement of the membrane potential from the resting potential

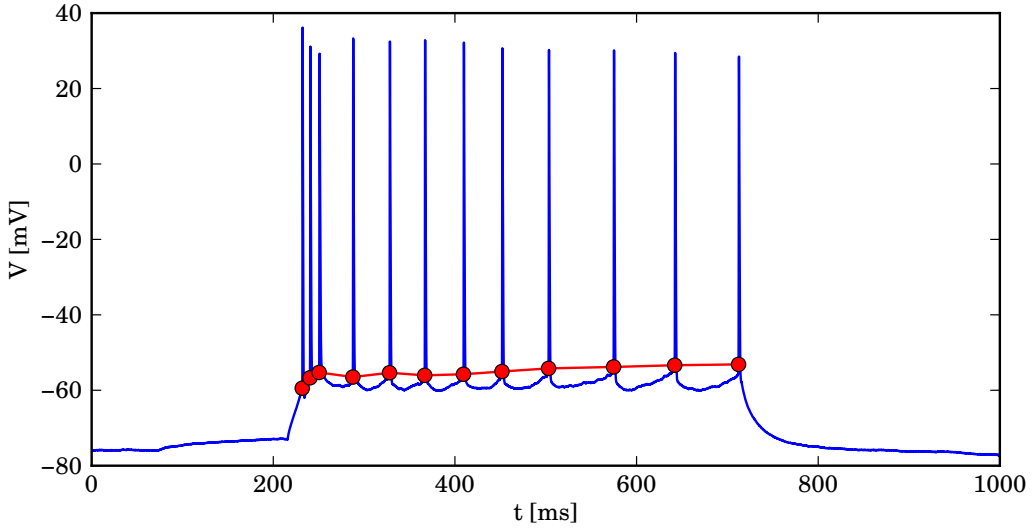


**Figure 1.1.** Example of spiking and bursting behaviour of a hippocampal pyramidal neuron; the time series of the membrane potential is shown in blue; the spike threshold of 20 V/s is shown in red and is different for every spike.

at which a spike is fired is called *a firing threshold* (Ermentrout and Terman, 2010; Hodgkin and Huxley, 1952; Izhikevich, 2006; Keener and Sneyd, 2009). The concept of a threshold is pivotal for neural excitability and much effort has been devoted to understanding this phenomenon. Despite these efforts, defining the excitability threshold is still an open problem (Izhikevich, 2006). Classically, the firing threshold is associated with a certain level of membrane potential. As illustrated in Figure 1.1, the spiking threshold is indicated by the abrupt change of the steepness of the membrane potential; it seems to differ slightly between spikes, especially for the initial burst. One could assume that, for instance,  $-60\text{ mV}$  is a firing threshold, but the threshold for initial spikes seems to be slightly lower and for the latter spikes clearly higher than  $-60\text{ mV}$ . In general, there is a considerable difficulty to define a single level because the threshold depends on the dynamical properties of the excitable cell (Ermentrout and Terman, 2010; Izhikevich, 2006; Keener and Sneyd, 2009). A different approach has been presented in (Naundorf et al., 2006), namely, firing threshold is defined as a function of the derivative of membrane potential, in this case a value of  $20\text{ V/s}$ . This approach allows to mark the estimated threshold in red, as shown in Figure 1.1. While this approach again indicates that the steepness of the membrane potential changes dramatically before the occurrence of a spike in a spike-train, it does not reveal a biophysical or a dynamical mechanism behind the process.

In this thesis we address the question of defining the excitability threshold in a number of ways. In Chapter 2 we study the influence of different types of ionic currents on excitability. The spike-adding mechanism is addressed in Chapter 4 and, using this result, the onset of a spike that is given by the firing threshold is defined in Chapter 5.

### 1.1.2 Hodgkin-Huxley formalism

In this section we present the Hodgkin-Huxley formalism, which is a mathematical description of the biophysical properties underlying excitability of neural cells. In their pioneering work on squid giant axon Hodgkin and Huxley (1952) showed that the membrane potential can be modelled as a capacitor in parallel with a nonlinear resistor representing the conductances of ionic currents, which yields their original system of nonlinear ordinary differential equations

$$C_m \frac{dV}{dt} = -I_{\text{ion}}(V, t) + I_{\text{app}} = -I_K(V, t) - I_{\text{Na}}(V, t) - I_L(V, t) + I_{\text{app}}, \quad (1.1)$$

$$\frac{dn}{dt} = \alpha_n(V)(1 - n) - \beta_n(V)n, \quad (1.2)$$

$$\frac{dm}{dt} = \alpha_m(V)(1 - m) - \beta_m(V)m, \quad (1.3)$$

$$\frac{dh}{dt} = \alpha_h(V)(1 - h) - \beta_h(V)h. \quad (1.4)$$

Here, Equation (1.1) expresses a potential difference  $V$  and  $I_{\text{ion}}(V, t)$  is the sum of all ionic currents in the cell. The potential difference is caused by different ion concentrations inside and outside the membrane. Through a rigorous data fitting, they further showed that two major ionic currents control this difference, namely,  $\text{Na}^+$ -current  $I_{\text{Na}}$  and  $\text{K}^+$ -current  $I_K$ . The last voltage-dependent current  $I_L$  represents a linear Ohmic leak, which is carried mostly by  $\text{Cl}^-$  ions. Applied current that perturbs the system is defined as  $I_{\text{app}}$ . The currents are controlled by the dynamics of gating variables  $n$ ,  $m$  and  $h$  described by Equations (1.2)–(1.4). The functions  $\alpha(V)$  and  $\beta(V)$  describe transition rates between open and closed states, respectively of a particular channel type.

The original Hodgkin-Huxley Equations (1.1)–(1.4) enabled more general description of the biophysical properties of neural cells. In fact, the two major currents  $I_{\text{Na}}$  and  $I_K$  represent a larger class of ionic currents, namely, *inward currents* that depolarise the membrane potential, i.e. initiate the spike, and *outward currents* that repolarise the membrane potential. In general, the equation for voltage-dependent ionic currents can be written as

$$I_x(V) = g_x m_x^\gamma h_x^\delta (V - E_S), \quad (1.5)$$

where  $g_x$  is a maximal conductance of a current,  $m$  and  $h$  are gating variables of a current and  $E_S$  is a reverse potential.

*The reverse potential* is associated with the potential difference caused by concentration differences of the ion distributions inside and outside the cell, and is specific for a particular ion type. Usually the reverse potential is derived from the *Nernst equilibrium* and called *Nernst potential*. Given the concentrations of the ions inside and outside the cell membrane, the Nernst

potential can be calculated as follows (Keener and Sneyd, 2009)

$$E_S = \frac{kT}{zq} \ln \left( \frac{[S]_o}{[S]_i} \right), \quad (1.6)$$

where  $k$  is the Boltzmann constant  $k = R/N_A$  defined by the universal gas constant  $R$  and the Avogadro number  $N_A$ ;  $q$  and  $z$  are the charges of a proton and the ion  $S$ , respectively. The  $S$  in square brackets,  $[S]_o$  and  $[S]_i$ , denote the outside and inside concentrations of the ion  $S$ , respectively. The value of the membrane resting potential shown in Figure 1.1 is associated with the reverse potential for  $K^+$ -current, because in equilibrium the concentration of  $K^+$ -ions is higher inside the cell for most animal cells (Keener and Sneyd, 2009). There are other equations for the reverse potential of an ionic current, e.g., the Gibbs-Donnan equation or the Goldman-Hodgkin-Katz equation (Keener and Sneyd, 2009), which are not used in the models presented in this thesis.

To understand the other terms of Equation (1.5) we need to describe how ion channels operate. As mentioned before, ion channels are large transmembrane pores that transport ions through the membrane. An ion channel can be in one of three generalised states: activated (opened), inactivated (blocked) or deactivated (closed) (Keener and Sneyd, 2009). Not all ion channels have all the states, e.g., some channels do not inactivate, in which case they are called *non-inactivating or persistent channels*. Channels that can activate and deactivate are called *transient channels*. Moreover, there can be many states of the same type. There are a number of ways to model ion channels but we use the one directly related to the original Hodgkin-Huxley formalism (Hodgkin and Huxley, 1952). Namely, we use gating variables that represent the fractions of channels in a given gating state. In particular,  $m_x$  describes a fraction of channels being activated and  $h_x$  describes the fraction of channels being deinactivated; when  $h_x = 0$  the ionic current is completely inactivated. The powers  $\gamma$  and  $\delta$  express the number of subunits of a given channel, each of which could be in any given state. Since a channel must be activated and deinactivated in order to be open, the fraction of channels being opened is  $m_x^\gamma h_x^\delta$ . Consequently, the fraction of closed channels is  $1 - m_x^\gamma h_x^\delta$ . Under these assumptions, the dynamics of a gating variable can be described by the first-order differential equation

$$\frac{dy_x}{dt} = \frac{y_{x\infty}(V) - y_x}{\tau_x(V)}, \quad (1.7)$$

where  $y_{x\infty}(V)$  is a steady-state activation function and  $\tau_x(V)$  is a time constant.

The steady-state (in)activation function and time constant of a particular current are determined experimentally via a technique called voltage clamp. *Voltage clamp* is an electrophysiological experiment to measure ionic current across the membrane of an excitable cell. Typically, the membrane potential is held at a certain holding level  $V_h$  and then stepped to a new value  $V_s$ . The difference of the potentials ( $V_s - V_h$ ) triggers a current flow, which is recorded

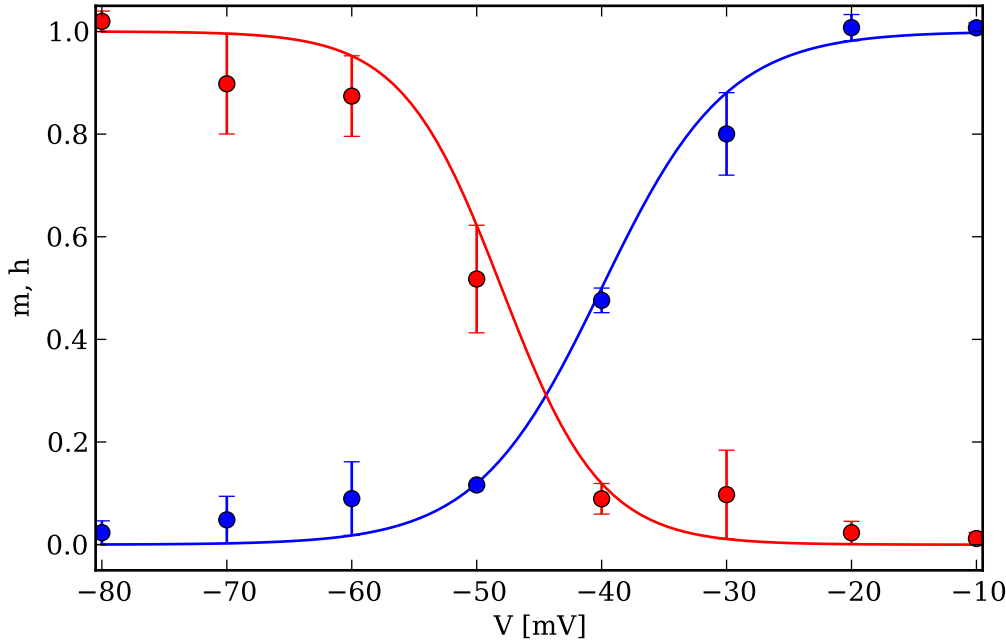


**Figure 1.2.** Example of steady-state (in)activation functions of a T-type  $\text{Ca}^{2+}$ -current; the points are obtained from the voltage-clamp experiments and labelled with dots of the respective colours; the error bars indicate the standard deviation of the measurements; the activation and inactivation curves in the form of Boltzmann function fitted to the voltage clamp measurements are depicted in blue and red, respectively.

(Hodgkin and Huxley, 1952; Hodgkin et al., 1952; Izhikevich, 2006). Analysing a steady-state current at a given voltage level gives a current-voltage relation. Since the gating variables are dimensionless, their measurements are obtained by normalising the current-voltage curves to the maximal value. After obtaining the gating data points the (in)activation function is fitted, usually by using a Boltzmann function

$$y_{x\infty}(V) = \frac{1}{1 + \exp\left(-\frac{V - V_{yx}}{k_{yx}}\right)}, \quad (1.8)$$

where  $V_{yx}$  is the half-maximum value and  $k_{yx}$  is the slope of the function, which determines the rate at which the fraction of channels in a given state is changing as a function of voltage. The relation between the state-transition rates in Equations (1.2)-(1.4) is

$$y_{x\infty}(V) = \frac{\alpha_x}{\alpha_x + \beta_x} \quad \text{and} \quad \tau_x(V) = \frac{1}{\alpha_x + \beta_x}.$$

In this thesis we use Equation (1.8) in the Boltzmann form for the dynamics of the gating variable.

Figure 1.2 shows examples of steady-state activation and inactivation functions of a T-type (transient)  $\text{Ca}^{2+}$ -current. The points are obtained from voltage-clamp experiments and labelled with dots of the respective colours; the error bars indicate the standard deviation of the measurements. The activation and inactivation have been fitted to experimental data using Boltzmann functions and are coloured blue and red, respectively. The time constant of the currents is also measured in a voltage-clamp experiment and is often voltage dependent. Nonetheless, for simplicity, it is usually approximated by a constant value. In many cases the time constants change very little with voltage, therefore, they are approximated by an average value for the voltage interval of interest. The constant-value assumption simplifies the model and enables better estimates of the time scale on which a variable evolves.

The maximal conductance of the current can, partially, be assessed from the current-voltage relation. The voltage-clamp experiment is measuring current in a patch of the cell membrane that is placed inside a glass pipette. Hence, the types and number of ion channels in this patch determine the level of the ionic current that flows when the voltage is stepped. Note that the channels in many neurons are not necessarily uniformly distributed across the cell membrane. On the other hand, Hodgkin-Huxley Equation (1.1) models the membrane potential of the whole cell. Namely, it models so-called *current clamp* in which the change in the membrane potential of the whole cell is measured in response to a current injection; Figure 1.1 is an example of such a current clamp recording. Since the magnitude of a current measured in the voltage-clamp experiment reflects just a fraction of the ionic channels in the whole cell, the maximal conductance is likely to differ between cells and, hence, between models.

The different ionic currents are characterised by different values of the steady-state activation and inactivation functions, and time constants. Those values, along with maximal conductances, determine the excitability of a cell. Often, small changes in these parameters can produce a vastly different response. We discuss the contribution of particular ionic currents on the excitability of our pyramidal neuron model in Chapter 2.

Above we explained how voltage-gated currents are modelled using the Hodgkin-Huxley formalism. There exist many channels that are controlled by intracellular messengers, such as  $\text{Ca}^{2+}$ , which require inclusion of the dynamics of such messengers and, thus, extension of the Hodgkin-Huxley formalism. The pioneering work of Chay and Keizer (1983) proposes a model that incorporates  $\text{Ca}^{2+}$  dynamics and  $\text{Ca}^{2+}$ -gated currents and combines them with classical voltage-gated currents. Another example of a more recent model containing  $\text{Ca}^{2+}$  dynamics along with  $\text{Ca}^{2+}$ -activated channels is given in appendix A (Tsaneva-Atanasova et al., 2007). This model has been analysed in Chapter 3.

Next, we focus on the original Hodgkin-Huxley model described by Equations (1.1)-(1.4) and explain the basis of excitability in this model. The values of the parameters correspond to the original model (Hodgkin and Huxley, 1952) but with reversed polarity and real Nerst

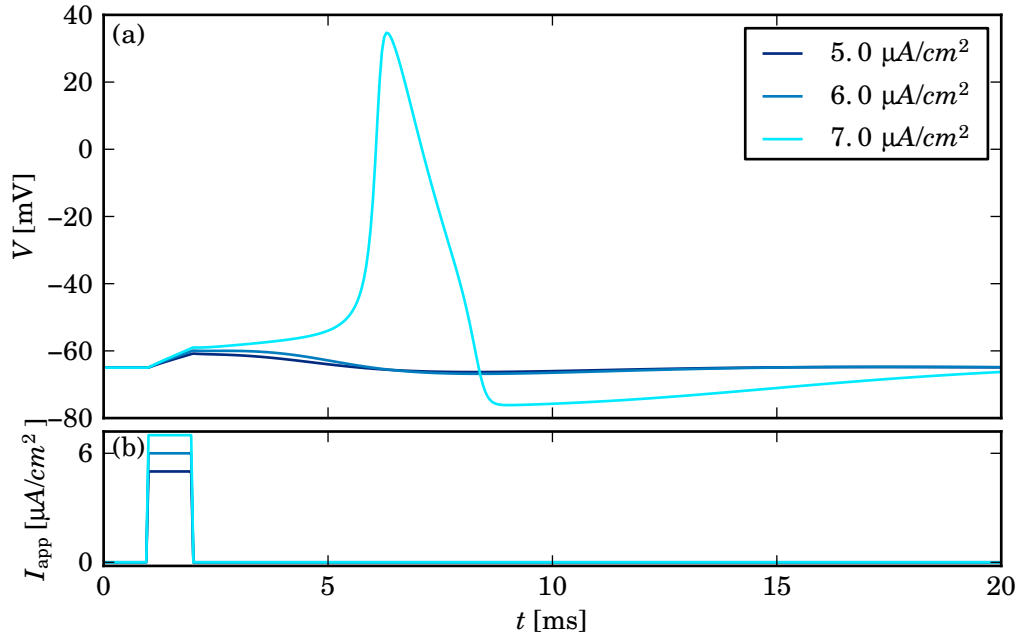


**Figure 1.3.** Example of spike in the Hodgkin-Huxley model (1.1)-(1.4); panel (a) shows the time trace of the responses of the membrane potential of the model to a brief current injection of 5, 6 and 7  $\mu\text{A}/\text{cm}^2$  depicted with the respective blue-gradient curves; panel (b) shows the time trace of the injected current.

reverse potentials as described in (Hansel et al., 1993). Figure 1.3 shows typical responses of the Hodgkin-Huxley model (1.1)-(1.4) to a brief current injection. The time traces of the membrane potential  $V$  for different magnitudes of the current injection  $I_{app}$  are shown in Figure 1.3(a) as blue-gradient curves. The corresponding trace of  $I_{app}$  is shown in Figure 1.3(b). The responses illustrated in Figure 1.3 are, in fact, a classical example of transient excitability. Namely, the current injections of 5 and 6  $\mu\text{A}/\text{cm}^2$  perturbed the model only slightly and result in a small deflection in  $V$  after which the membrane potential returns back to the stable equilibrium, i.e., the resting potential. In contrast, the current increase to 7  $\mu\text{A}/\text{cm}^2$  gives a markedly different response. In this case, shown as the top curve in Figure 1.3(a),  $V$  makes a large excursion in the form of a spike before it relaxes back to the stable equilibrium. Note that the current injection shown in Figure 1.3(b) ends clearly before the actual spike is generated. Therefore, the spike is generated due to the underlying dynamics of the system and the current plays the role of a perturbation. This excitable behaviour is transient because it takes place when the trajectory returns to the only stable attractor that exists in the system, where it will remain until the system is perturbed again.

The base of the excitable spiking behaviour of the Hodgkin-Huxley model (1.1)-(1.4) lies in the time-scale separation of its variables. The fastest variable in this model is the membrane potential  $V$ . The other fast variable, which is slightly slower than  $V$  but works on a similar

time scale, is  $m$ . This variable characterises the activation of the  $\text{Na}^+$ -channels that initiate the spike. The system (1.1)-(1.4) has two slow variables  $h$  and  $n$ , which are more than one order of magnitude slower than the fast variables. Those two variables are responsible for repolarising  $V$  back to the resting state. Namely,  $h$  inhibits, i.e., decreases the  $\text{Na}^+$ -current and  $n$  activates the  $\text{K}^+$ -current, which has an opposite sign to the  $\text{Na}^+$ -current. Since  $h$  and  $n$  are slower than  $m$  they start affecting the system later, which allows the spike to grow rapidly. When  $h$  and  $n$  finally reach an sufficient value, they counteract the effect of  $m$  and  $V$  returns to the resting potential. If there was no time-scale separation between the variables in the Hodgkin-Huxley model (1.1)-(1.4), the increase of  $V$  and, thus,  $m$  would be immediately compensated by  $n$  and  $h$  and the spike would not occur.

The major advantage of Hodgkin-Huxley formalism (Hodgkin and Huxley, 1952) is the fact that it is based on experimental data. This allows the modelling predictions to be related back directly to the real system. All models presented in this thesis are written in Hodgkin-Huxley formalism (Hodgkin and Huxley, 1952). As the models using Hodgkin-Huxley formalism are systems of ordinary differential equations, we can use many advanced tools from dynamical systems theory in order to address fundamental questions about how the real system operates. We also explore the natural time-scale separation present in the model to analyse them.

## 1.2 Bifurcation analysis of slow-fast systems

As mention in the previous section, a typical feature of the Hodgkin-Huxley models is the separation of time scales between the variables that governs the excitable behaviour of neural cells. For example, FitzHugh utilised the time-scale separation simplifying the Hodgkin-Huxley model and explaining the essence of the excitability in this model (Fitzhugh, 1960). The ideas behind such analysis come from *geometrical singular perturbation theory* (GSPT) (Dumortier, 1993; Fenichel, 1979; Jones, 1995; Szmolyan and Wechselberger, 2001; Wechselberger, 2005). In general, *singularly perturbed systems* or *slow-fast systems* are vector fields of the form

$$\begin{aligned}\varepsilon \dot{x} &= f(x, y), \quad x \in \mathbb{R}^n \quad (\text{fast}), \\ \dot{y} &= g(x, y), \quad y \in \mathbb{R}^m \quad (\text{slow}).\end{aligned}\tag{1.9}$$

Here  $\varepsilon > 0$  is a small parameter that governs the time-scale separation. Hence, system (1.9) has  $n$  fast variables  $x$  and  $m$  slow variables  $y$ . In Hodgkin-Huxley models the time-scale separation between slow and fast variables is usually not well defined. In this thesis we assume that the separation of time scales is well defined if time constants of variables of a model are different by at least one order of magnitude. Note that all variables within one class (slow or fast) do not have to evolve on identical time scales, but they are of a similar order of magnitude. Using the

time  $t = \tau/\varepsilon$ , system (1.9) can be rescaled to

$$\begin{aligned} x' &= f(x, y), \\ y' &= \varepsilon g(x, y), \end{aligned} \tag{1.10}$$

where  $\tau$  is *the slow time scale* and  $t$  is *the fast time scale* (Desroches et al., 2012; Fenichel, 1979; Hek, 2010).

The GSPT takes advantage of this time-scale separation of a slow-fast system in the singular limit  $\varepsilon \rightarrow 0$ . Namely, in this limit the solution of system (1.10) becomes *the fast subsystem*

$$\begin{aligned} x' &= f(x, y), \\ y' &= 0. \end{aligned} \tag{1.11}$$

The above Equation (1.11) implies that the fast variables are much faster than slow variables, hence, only the fast ones evolve and slow ones are constant. This decomposition allows us to analyse the dynamics of only the fast system for some chosen values of slow variables, that can be treated as constant parameters in this case.

Similarly, the system (1.9) in the limit  $\varepsilon \rightarrow 0$  becomes *the slow subsystem*

$$\begin{aligned} 0 &= f(x, y), \\ \dot{y} &= g(x, y). \end{aligned} \tag{1.12}$$

Equation (1.12) also uses the assumption that fast variables are much faster than the slow variables, but in this singular limit only the slow variables evolve. Namely, in the case of the slow subsystem the transients of fast variables are disregarded and they assume to be in their equilibria; it allow the study to focus on slow dynamics only. The differential-algebraic equation (DAE) (1.12) defines the so-called *slow flow*. The algebraic equation in (1.12) defines *the critical manifold*

$$S := \{(x, y) \in \mathbb{R}^m \times \mathbb{R}^n | f(x, y) = 0\}.$$

Note that points on  $S$  are equilibria of the fast subsystem. Hence, the evolution of the slow variables is restricted to  $S$ . In the case of Hodgkin-Huxley models the critical manifold is often divided into series of attracting ( $S^a$ ) and repelling ( $S^r$ ) sheets separated by folds ( $F$ ). The type of sheet is defined by the stability of the equilibria that span the sheet.

To solve DAE (1.12) to obtain the slow flow we often need to desingularise it, because it is singular at the fold  $F$ . We do that by scaling the time with  $-\det Df_x$ , where  $Df_x$  is a Jacobian with respect to the fast variables  $x$ ; details of this process are described in Chapter 4, where we analyse the slow flow of our model. In some cases equilibria of the desingularised slow flow are placed on the fold  $F$ . These points are called *folded singularities*, which may gives rise to complicated dynamics, such as mixed-mode oscillations (Desroches et al., 2008a, 2012).

Typically for slow-fast systems, trajectories of the full system follow approximately the attracting sheets of  $S$ . However, there exist a special type of solutions that can follow the repelling sheets of  $S$ . These orbits are called *canards* and were first reported in (Benoît et al., 1981) and later extensively studied (Brøns and Bar-Eli, 1991, 1994; Desroches et al., 2008a, 2012; Dumortier, 1993; Szmolyan and Wechselberger, 2001; Wechselberger, 2005). In the classical planar case, canards are formed during a sudden increase in the model response called *canard explosion*, which was first described in (Brøns and Bar-Eli, 1991).

GTSP allows to understand the dynamics of the full system (1.9) or (1.10) by studying the slow and fast subsystems (1.12) and (1.11) in the singular limit (Desroches et al., 2012). This slow-fast decomposition is especially useful for studying high-dimensional systems, because it reduces the dimensionality of the problem. Our analysis in both Chapters 3 and 4 takes advantage of the time-scale separation and employs GSPT.

The critical manifold  $S$  of the slow-fast system contains all equilibria and periodic attractors of the fast subsystem. Therefore, to establish  $S$  we evaluate and analyse the stability of fixed points and periodic orbits of the fast subsystem. *Bifurcation theory* provides a strategy to investigate changes of stability of equilibria and periodic orbits as a function of the system's parameters and enables us to study  $S$  in more depth and, thus, gain more insight into the behaviour of the full system. In general, a *bifurcation* takes place when a qualitative change of the dynamics, or topological inequivalence, occurs as parameters of the system are varied. The point in parameter space at which such a change takes place is called *bifurcation point*. Hence, bifurcation theory allows us to produce *bifurcation diagrams* that divide the parameter space into regions of topological equivalence (Arnol'd et al., 1994; Guckenheimer and Holmes, 2002; Kuznetsov, 1998).

Bifurcation theory investigates the behaviour of the system in the context of parameter variation. GSPT allows us to separate the system according to time scales and investigate its behaviour using bifurcation theory. Namely, Equation (1.11) implies that, since the dynamics of the fast subsystems are much faster than the dynamics of the slow subsystem, we can assume that the slow variables remain constant. Therefore, we can investigate the changes in the stability of the fixed points of the fast subsystem by performing bifurcation analysis of the fast subsystem treating the slow variables as parameters. The resulting bifurcation diagram of the fast subsystem is, in fact, a piece of the critical manifold. Furthermore, the fixed points of the full system can undergo bifurcations as well. Therefore, bifurcation analysis is also often applied to the full system. These techniques have been used extensively to analyse the behaviour of excitable dynamical systems as we briefly summarise in the next section.

### 1.3 Transient bursting mechanisms

The majority of neural cell models are high dimensional and are characterised by rich dynamics, which manifest themselves by a variety of different behaviours. The change of the model behaviour can occur within a small range of parameters and, thus, characterising it can be a challenging task. Such properties have provoked a large number of studies based on dynamical systems theory. Moreover, the theory of slow-fast systems along with bifurcation analysis allow for a new, more general understanding of excitable systems, and also lead to many types of burster's classifications.

In his pioneering work (Rinzel, 1985, 1987), Rinzel incorporated the decomposition of a system into slow and fast subsystems following the ideas of GSPT (Fenichel, 1979). Rinzel utilised the bifurcation analysis of the fast subsystem and showed that the burst can be divided into active (spiking) and silent phases, which follow different types of attractors of the fast subsystem. Rinzel also classified the bursting oscillators based on the structure of the bifurcation diagram of the fast subsystem (Rinzel, 1987).

We illustrate the idea behind Rinzel's approach in an example using the unified pyramidal neuron model presented in Chapter 2. In order to get periodic bursting, we reduce the maximal conductance of the delayed rectifier  $K^+$ -current compared to the value that will be used in Chapter 2. Figure 1.4 shows an illustrative example of periodic and transient bursting along with the critical manifold obtained from the bifurcation analysis of the fast subsystem. The branches of stable and unstable equilibria are depicted with black and red lines, respectively. Similarly, the maximal and minimal values of stable and unstable families of periodic orbits are depicted with blue and magenta lines, respectively. The fold and Hopf bifurcations are marked with labelled dots. Figure 1.4(a) shows an example trajectory of a periodic burst (grey) overlaid on the bifurcation diagram. Figure 1.4(b) shows a similar situation but involving an example of a transient trajectory with (light-grey) and without current injection (grey). The time series of the respective periodic and transient bursts are shown in Figures 1.4(c) and (d). Identifiably, the periodic burst continues, whereas, the transient burst occurs only once after the current injection, which is indicated by the light-grey segment, and then the system eventually returns to the stable equilibrium  $V^*$ .

The time-scale separation in the model allows us to decompose it into fast and slow subsystems as described in Section 1.2. The bifurcation diagrams of the fast subsystem has been parametrised by the slow variable  $h_{Ca_T}$ , with the other slow variable treated as parameter and fixed to a constant value. In fact, the bifurcation diagram is only a part (a slice) of the critical manifold because the system has four slow variables. The presented diagrams appear to be very similar but note that they were calculated for slightly different parameter values. Namely, the periodic bursting in the system only occurs when a constant holding current of  $2 \mu A/cm^2$

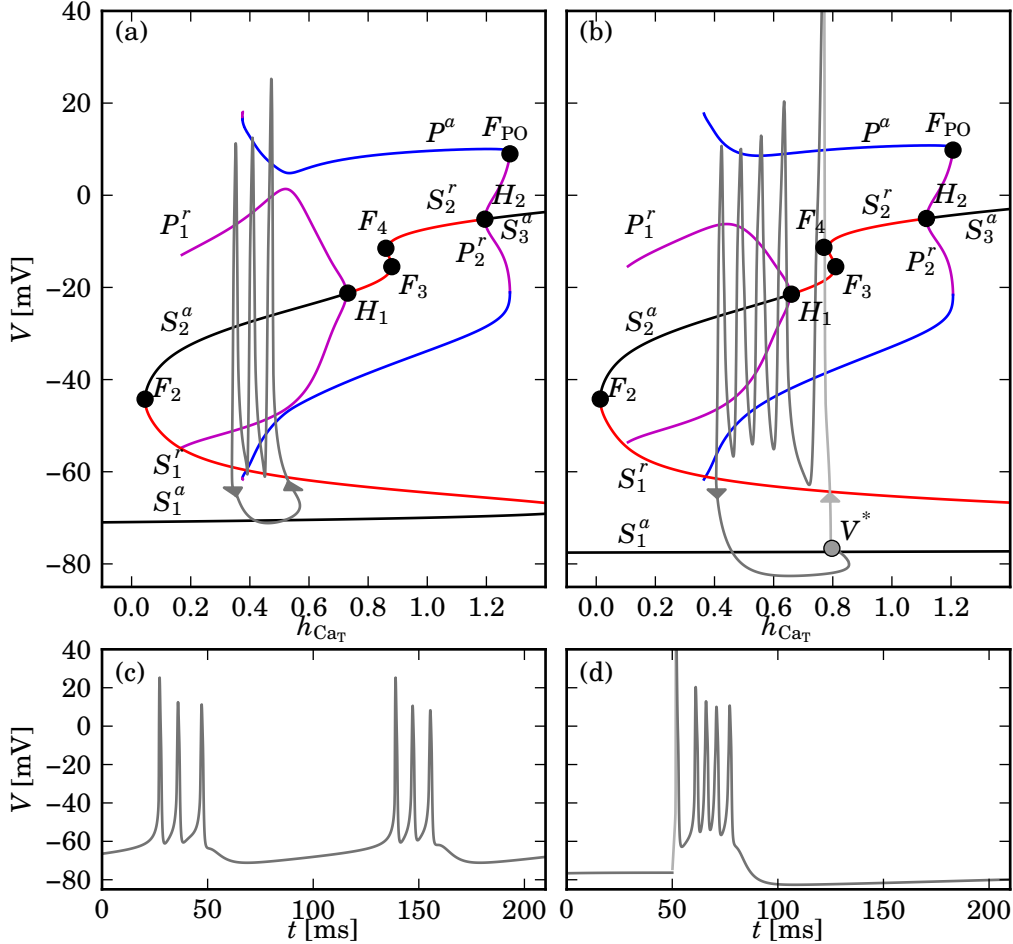


**Figure 1.4.** Examples of periodic and transient bursting with the underlying critical manifold obtained from the bifurcation analysis of the fast subsystem, where the slow variable is a parameter; the branches of stable and unstable equilibria are coloured with black and red, respectively; the maximal and minimal values of stable and unstable families of periodic orbits are coloured with blue and magenta, respectively; fold and Hopf bifurcations are marked with labelled dots; panel (a) shows a trajectory of a periodic burst (grey) overlaid on the bifurcation diagram; panel (b) shows a trajectory of a transient burst overlaid on the bifurcation diagram with (light-grey) and without current injection (grey); panels (c) and (d) show time series of the trajectories of periodic and transient bursts, respectively.

is applied. Thus, the bifurcation diagram in Figure 1.4(a) has been calculated with this holding current injection, which also causes the bottom stable branch to be slightly higher. Since the transient burst occurs when the trajectory returns to the stable equilibrium  $V^*$ , the bifurcation diagram shown in Figure 1.4(b) has been calculated for the fast subsystem without current injection.

Let us now describe the bifurcation diagrams shown in Figure 1.4 in more detail. Since the bifurcation diagrams are qualitatively the same, we use the same explanation and notation for

both of them. The bottom branch  $S_1^a$  of stable equilibria loses stability at the fold point  $F_1$  (not shown) and becomes branch  $S_1^r$  of saddle points. The branch  $S_1^r$  regains stability at another fold  $F_2$  and becomes  $S_2^a$ . The branch  $S_2^a$  loses stability again in a subcritical Hopf bifurcation  $H_1$ , from which the family  $P_1^r$  of unstable periodic orbits originates; the subsequent branch becomes  $S_2^r$  and consists of equilibria with two unstable eigenvalues. The branch  $S_2^r$  has two consecutive folds  $F_3$  and  $F_4$  and regains stability in another subcritical Hopf bifurcation  $H_2$ , after which it becomes the stable branch  $S_3^a$ . The Hopf bifurcation  $H_2$  gives birth to an unstable family  $P_2^r$  of periodic orbits that undergoes a fold of periodic orbits  $F_{\text{PO}}$  with the stable family  $P^a$ . Both families of periodic orbits  $P_1^r$  and  $P^a$  terminate in homoclinic bifurcations.

Rinzel's classical idea relates to periodic bursters. Hence, we first focus on Figure 1.4(a). The trajectory of the burst is clearly divided into silent and active phases, as shown in Figure 1.4(a). In the silent phase, the trajectory approximately follows the stable branch  $S_1^a$  of the bifurcation diagram of the fast subsystem. At the end of the silent phase the trajectory becomes attracted to the family of stable periodic orbits  $P^a$ . Moreover, as soon as it crosses the nullcline of the slow variable  $h_{\text{CaT}}$ , i.e., the curve for which  $h_{\text{CaT}}/dt = 0$ , the trajectory changes direction and follows  $P^a$ . The active phase ends when the trajectory reaches the end of the periodic orbit family  $P^a$ , that is, at a homoclinic bifurcation. Then it drops back to the branch  $S_1^a$  of stable equilibria, marking the beginning of the next silent phase, and the cycle repeats. Based on this bifurcation analysis we could explain *the bursting mechanism*, i.e., the way in which the fast subsystem dynamics control the bursting phenomenon. We remark that this is just one example of a bursting mechanism, which occurs in our unified model of pyramidal neurons presented in Chapter 2, and many other bursting mechanisms have been reported; see (Ermentrout and Terman, 2010; Izhikevich, 2000, 2006; Rinzel, 1987) for further references.

Actually, most of the spiking and bursting in the brain is not a periodic phenomenon. It only occurs after a perturbation, such as synaptic transmission, that drives the membrane potential away from the resting potential. Hence, neural responses typically take place as the cell returns to its equilibrium. Therefore, spiking and bursting, which are important elements of brain function, are most often transient phenomena (Andersen et al., 2007; Brown and Randall, 2009). Despite a large number of studies and classifications of spiking and bursting mechanisms, most of them consider these behaviours as periodic and, in particular, transient bursting is still largely mathematically unexplored. In this thesis, we present a different approach that utilises the ideas of GSPT and applies them to transient bursting phenomena.

We illustrate our approach to analysing transient bursts with the example in Figure 1.4(b). It shows a bifurcation diagram of the fast subsystem with the slow variable  $h_{\text{CaT}}$  as a parameter calculated without a current injection. As mentioned before, the transient burst trajectory is overlaid on the bifurcation diagram. Namely, we distinguish two phases of the trajectory, with and without current injection. The first phase coloured with light-grey, is a phase in which the system is perturbed by a current injection and evolves away from the stable equilibrium  $V^*$ ,

which is the resting potential of the model cell as shown in Figure 1.4(b). After the brief current injection the grey trajectory is attracted to the stable periodic orbits family  $P^a$ , which causes a burst of four additional spikes to be fired. As the family of periodic attractors  $P^a$  terminates in a homoclinic bifurcation, the trajectory is attracted to the branch of stable equilibria  $S_1^a$  and follows  $S_1^a$  until it reaches the stable equilibrium  $V^*$  of the full system, where it remains. Note that, bursting takes places during the return to this equilibrium state. Moreover, for another burst to occur the system has to be perturbed again.

The bifurcation diagrams shown in Figure 1.4 give some insight into the bursting behaviour of the system. Nonetheless, some of the features are not very well captured. For example, the termination of the silent phase of the periodic burst in Figure 1.4(a) is not explained well. Also, the spikes in a burst do not follow  $P^a$  closely. It is because the system has a multiple slow variables that change during the burst, but, in this analysis, they all have been fixed to constant values (corresponding to the active phase). This example points out the importance of taking into account the other slow variables, especially, since many physiologically accurate models are high-dimensional and often have many slow variables. In this thesis we analyse this system considering multiple slow variables. In particular, in Chapter 4 we analyse a reduced version of the model presented in Chapter 2, which has been shown in Figure 1.4. Our analysis considers two slow variables that parametrise a two-dimensional critical manifold, which is sufficient to explain the bursting in the case of this model. Nonetheless, there are many examples of simpler models that have only one slow variable, which can be analysed in more classical way. An example of such a simpler system is pituitary cell model, which we analyse in Chapter 3 with respect to only one slow variable.

Transient bursting behaviour has been associated with so-called *after-depolarisation* (ADP), which is a positive deflection of a membrane potential after a spike. Hence, it occurs as the trajectory returns to the equilibrium in the transient burst. Moreover, ADP is a hallmark of excitability and a precursor of bursting in hippocampal pyramidal neurons (Andersen et al., 2007; Brown and Randall, 2009). In Chapter 2 we use nullcline analysis of our model and show how the ADP is created. Moreover, we use the same analysis to mathematically define the ADP and characterise the time-scale separation between gating variables necessary for the ADP to occur.

Another important question is the duration of the active phase of a burst and, consequently, the number of spikes. Previous studies analysed this problem for bursting oscillators. Terman (Terman, 1992) studied transitions between bursting and tonic (continuous) spiking. He recognised the importance of connecting classical slow-fast analysis with full-system bifurcation analysis, which is necessary for detecting chaos in the system. The study in (Terman, 1992) focusses on chaotic dynamics; see (Govaerts and Dhooge, 2002; Guckenheimer and Kuehn, 2009; Tsaneva-Atanasova et al., 2010) for studies that focus on the spike-adding mechanism

directly. This analysis shows that the spike-adding mechanism is organised by a pair of saddle-node bifurcations of periodic orbits of the full system; bursts with different numbers of spikes are, in fact, different periodic attractors of the full system that may coexist only if the number of spikes differs by one (Terman, 1992; Tsaneva-Atanasova et al., 2010). In an other recent study Ghigliazza and Holmes (2004) present a generalised Hodgkin-Huxley model and explain the contribution of transient and persistent ionic currents to the bursting behaviour. They use bifurcation analysis of the fast subsystem of their three-dimensional model to show different behaviours ranging from resting, through tonic spiking, to bursting oscillations. Moreover, they explain which features of the ionic currents influence the number of spikes in a burst.

We study a different mechanism of bursting oscillations in Chapter 3. In this model the spikes in the active phase of a burst are not caused by a stable periodic orbit family but they are created via a weakly attracting branch of foci equilibria. This bursting mechanism is called *pseudo-plateau bursting*. Here, we study a system with a single slow variable, which is sufficient to explain the pseudo-plateau bursting. Nonetheless, Vo et al. (2010) successfully analyse a very similar model of pseudo-plateau bursting using two slow variables to explain this behaviour. We explain the fact that the termination of the burst happens before the orbit reaches the end of the branch of foci equilibria. To explain this behaviour, we compute a family of one-dimensional stable manifolds of the fast subsystem that arises from the branch of saddle equilibria. This manifold plays the role of *separatrix* in the system, i.e., it separates the basin of attraction of the two stable branches. We show that the orbit crosses the stable manifold before it reaches the end of the stable branch, which causes the seemingly premature termination of the active phase.

In our case of a transient burst, the spikes are created as the trajectory returns to the equilibrium. Therefore, we cannot expect the spike adding to occur via bifurcations in the full system. Moreover, the majority of the aforementioned studies show solutions with different numbers of spikes, but they do not focus on what is happening during the spike-adding transition. In Chapter 4 we use the ideas of GSPT and analyse spike adding in a transient burst. We show that the spike-adding is a canard-like phenomenon and happens on a very small parameter range. Namely, as the parameter is increased the trajectory traces an unstable sheet of the critical manifold, constructed of two-dimensional surfaces of saddle equilibria of a fast subsystem parametrised by two slow variables. As the trajectory is pushed on the other side of the critical manifold, via a jump point, which is a fold of the critical manifold, and is attracted to a family of periodic orbits, a new spike is created. We also show another spike-adding mechanism, in which a saddle equilibrium of the full system is present on the unstable sheet of critical manifold and it is attracting in respect to the slow flow.

In Chapter 5 we use the knowledge of ADP and spike-adding mechanism and formulate our model in terms of two-point boundary value problem, that directly corresponds to the experimental protocol. We show that the onset of ADP and a spike correspond to extrema of a

slow variable of the system and can be detected as folds using our boundary value problem formulation. This result offers a different view on the spiking threshold and spike generation itself, namely, as a deformation of the trajectory and, not as an abrupt process. Furthermore, Chapter 5 shows an application of continuation-based numerical methods to study the transient dynamics of the model under parameter variation. It allows to establish the boundaries of model behaviour in two parameters, which reveals the model’s sensitivity to changes in these parameters. The problem formulation and analysis is relatively general and can be applied to other models.

## 1.4 Numerical methods and tools

To perform the analysis presented in this thesis a number of numerical tools have been used. For numerical simulation we used XPP (Ermentrout, 2002) and integration methods from Python package SciPy (Jones et al., 2001; Oliphant, 2007). Moreover, we used the package XPPy (Nowacki, 2011) to perform the XPP simulations in Python.

The majority of figures has been done in Python using Matplotlib (Hunter, 2007). For more demanding visualisation tasks, Mayavi (Varoquaux and Ramachandran, 2008) has been used. In Chapter 3, Matlab has been used for visualisation.

An important element of our study is *numerical continuation*, that is, a method of following solutions of systems of equations that depend on parameters (Doedel, 2007). Most of the continuation of equilibria and periodic orbits was done using AUTO (Doedel, 1981; Doedel and Oldeman, 2009). This allowed us to calculate the critical manifold and perform the analyses presented in Chapters 4 and 3.

Furthermore, AUTO (Doedel, 1981; Doedel and Oldeman, 2009) has been used for the continuation of orbit segments as solutions to a two-point boundary value problem. In particular, the numerical methods that we use to analyse the spike-adding mechanism in a transient burst are based on such a two-point boundary value problem; this approach has already been applied to the bifurcation analysis of periodic orbits, including homoclinic or heteroclinic bifurcations (Champneys et al., 1995), and more recently for the computation of invariant manifolds (Krauskopf and Osinga, 2007) and so-called slow manifolds in systems with multiple time scales (Desroches et al., 2008a,b). Finally, in Chapter 3 we calculate the stable manifold using orbit segment continuation.



# Chapter 2

## A unified model of CA1/3 pyramidal cells: An investigation into excitability

After-depolarisation is a hallmark of excitability in hippocampal pyramidal cells of the CA1 and CA3 regions, because it constitutes the subthreshold relation between inward and outward ionic currents. This relationship determines the nominal response to stimuli and provides the necessary conditions for firing a spike or a burst of action potentials. Nevertheless, after-depolarisation is an inherently transient phenomenon that is not very well understood. In this chapter we study after-depolarisation using a single-compartment pyramidal-cell model based on recent voltage- and current-clamp experimental data. We systematically investigate CA1 and CA3 behaviour and show that changes to maximal conductances of certain ionic currents, namely, T-type  $\text{Ca}^{2+}$ -current and muscarinic-sensitive and delayed rectifier  $\text{K}^+$ -currents, are sufficient to switch the behaviour of the model from a CA3 to a CA1 neuron. We also explain with sensitivity analysis the influence of particular ionic currents on the excitability. The study ends with a model analysis that allows us to define after-depolarisation and the bursting threshold.

### 2.1 Background

We study the mechanisms underlying excitability of the hippocampal pyramidal neurons that are the principal excitatory neurons of the hippocampus. The hippocampus is critical for the formation of new memories and is one of the first brain areas to show damage in Alzheimer's disease. It is also a common focus site in epilepsy that can be damaged through chronic seizures (Andersen et al., 2007). Hence, changes in excitability of neurons in this brain region may have a profound impact on the overall performance of the brain (Brown and Randall, 2009; Harvey et al., 2009; Kile et al., 2008; Misra et al., 2008).

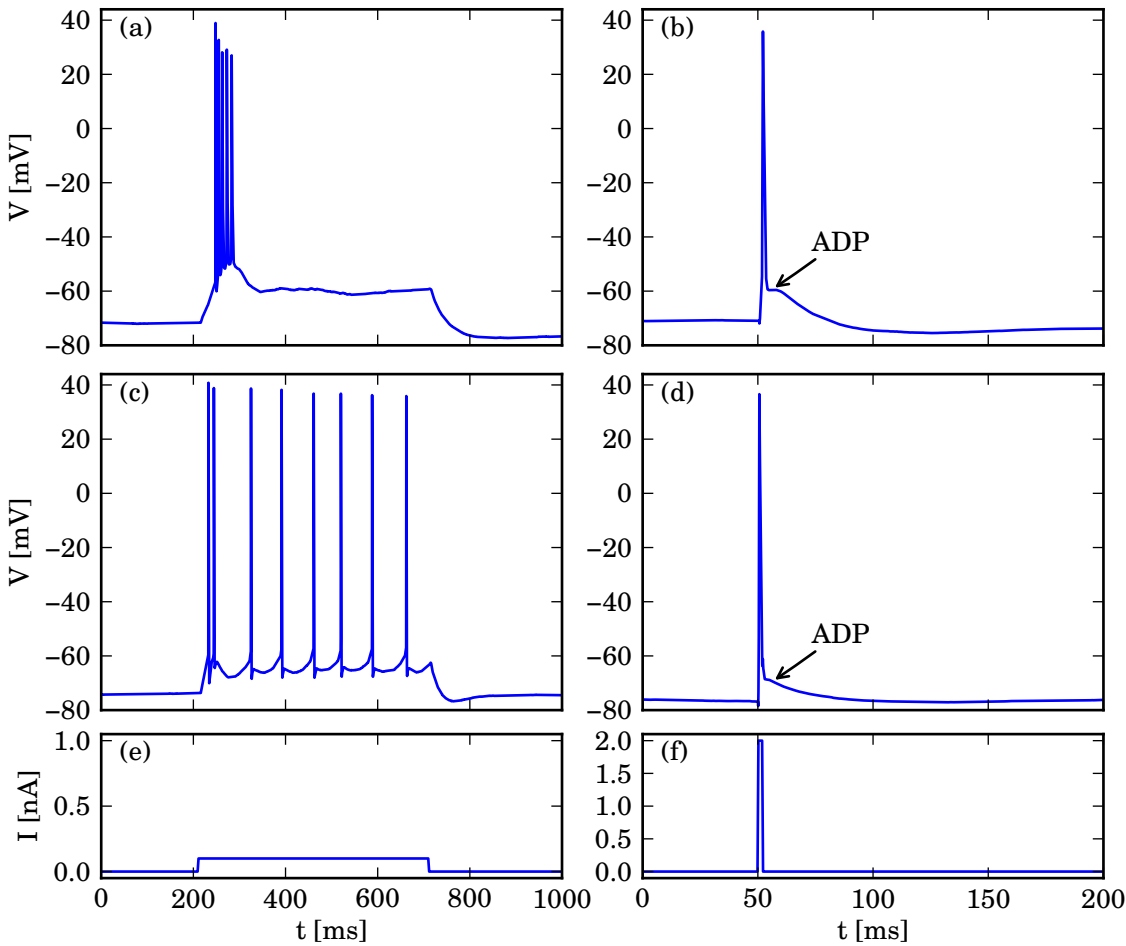


**Figure 2.1.** Electrophysiological differences between CA1- and CA3-area neurons; in a long-stimulus experiment 100 pA current is injected into a cell for 500 ms; in a short-stimulus experiment 2 nA current is injected into a cell for 2 ms; panels (a) and (b) show the typical responses of a CA3-area neuron to long and short stimuli, respectively; similarly, panels (c) and (d) show the typical responses of a CA1-area neuron to these two stimuli, respectively; panels (e) and (f) show the time traces of the injected current for the long- and a short-stimulus experiments, respectively. All experiments were performed in a submerged recording chamber maintained at  $32 \pm 1^\circ\text{C}$ , perfused with an artificial cerebrospinal fluid. The synaptic transmission was blocked pharmacologically without the truncation of the dendrites; see (Brown and Randall, 2009) for details on these methods.

From an electrophysiological point of view, pyramidal neurons in CA1 and CA3 exhibit noticeably different behaviours; Figure 2.1 illustrates examples of the responses for two *in-vitro* current-clamp experiments. The left column of Figure 2.1 presents a long-current injection experiment, where current of magnitude 100 pA (e) is injected into a CA3 (a) and CA1 (c) neuron for 500 ms. The right column of Figure 2.1 presents a short-current injection experiment, where 2 nA current (f) is injected into a CA3 (b) and CA1 (d) neuron for 2 ms. In contrast to CA1 pyramidal neurons, the responses of the pyramidal neurons from the CA3 region to a

long positive-current injection are characterised by an initial high-frequency burst of two to five spikes, followed by a depolarised plateau with or without several low-frequency spikes. Moreover, the responses of CA3 pyramidal neurons are characterised by large cell-to-cell variability with varying degrees of spike frequency accommodation, while those of CA1 neurons are rather regular. (Andersen et al., 2007; Brown and Randall, 2009; Migliore et al., 1995; Safiulina et al., 2008; Scharfman, 1993; Traub et al., 1991; Wong and Prince, 1981). As shown in Figure 2.1(c), the response of CA1 neurons to a long positive-current injection exhibits rather regular spiking patterns with a slightly higher frequency of the spikes at the beginning of the stimulus (Andersen et al., 2007; Golomb et al., 2006; Yaari et al., 2007; Yue and Yaari, 2004, 2006; Yue et al., 2005).

A characteristic feature of the CA1 and CA3 neurons that becomes evident during experiments is the so-called after-depolarisation (ADP), also known as depolarising afterpotential (DAP) (Brown and Randall, 2009; Izhikevich, 2006; Wong and Prince, 1981). It is a positive deflection of the membrane potential, which creates the characteristic 'hump' shown in Figures 2.1 (b) and (d). The amplitude of the ADP is usually larger for the CA3 neurons (Andersen et al., 2007; Wong and Prince, 1981). Furthermore, ADP with sufficiently high amplitude produces a burst of several spikes in both CA1 and CA3 neurons (Brown and Randall, 2009; Wong and Prince, 1981; Yaari et al., 2007; Yue and Yaari, 2004; Yue et al., 2005). Due to its importance for neural excitability ADP has been the focus of many recent experimental studies (Brown and Randall, 2009; Chen and Yaari, 2008; Golomb et al., 2006; Safiulina et al., 2008; Yaari et al., 2007; Yue and Yaari, 2004, 2006; Yue et al., 2005). It has been shown that this phenomenon is regulated by muscarinic-sensitive (M-type)  $K^+$ -channels (Yue and Yaari, 2004, 2006). More recent results also indicate that persistent  $Na^+$ -channels (Golomb et al., 2006; Yue et al., 2005) and transient  $Ca^{2+}$ -channels (Chen and Yaari, 2008) play an important role for ADP regulation. Furthermore, these studies suggest that ADP is a feature regulated by the intrinsic properties of the pyramidal cell-body membrane (Brown and Randall, 2009; Chen and Yaari, 2008; Golomb et al., 2006; Safiulina et al., 2008; Yaari et al., 2007; Yue et al., 2005). In this chapter we present a modelling study of CA1/3 pyramidal cells focussing on how the intrinsic properties of the cell body (soma) shape the ADP. Accordingly, we use Hodgkin-Huxley formalism (Hodgkin and Huxley, 1952) and consider only a somatic compartment in our model.

The model is parametrised according to the recently published (Brown and Randall, 2009) and unpublished experimental data; a few values are also based on other published experimental measurements (Blackmer et al., 2009; Destexhe and Bal, 2009; Golomb et al., 2006; Liu et al., 2003; Yaari et al., 2007; Yue and Yaari, 2004, 2006; Yue et al., 2005). Although in this study we focus mainly on the transient behaviour of a pyramidal neuron, the responses of CA1 and CA3 pyramidal cells to both long and short stimuli are also reproduced well by the model. To demonstrate this, we validate our model against such experimental data. Moreover, we show

that the transition between the two types of pyramidal cells in the model can be obtained by changing only three maximal conductances.

In order to dissect the excitability of the pyramidal cell model we perform a sensitivity analysis based on our excitability measure. We investigate the effect of changing the maximal values of current conductances, because they are most likely to vary among cells. This analysis allows us to make predictions about the role of isolated currents for the behaviour of the model. We show that a decrease of high-voltage-activated inward currents can increase excitability and that low-voltage-activated currents have a profound influence on ADP.

Although ADP has been studied quite extensively in experiments, the mechanisms underlying this phenomenon have received little theoretical attention. In particular, to date, there have been no attempts to formalise ADP mathematically. Having constructed a model validated by recent experimental data, we use it to dissect the ADP. We analyse ADP from a mathematical point of view and investigate what the underlying mechanisms are. In addition, we investigate the bursting-threshold for a burst of action potentials riding on top of the ADP, which is fundamentally different from the spiking-threshold of a single action potential. This transient bursting behaviour is not only important during physiological responses of a pyramidal cell, but is also related to pathological conditions characterised by hyperexcitability in the hippocampus, such as epilepsy. Furthermore, recent in-vivo experiments indicate that bursting takes place in hippocampal place cells during spatial navigation (Harvey et al., 2009) and, thus, could be important for memory and learning.

## 2.2 General single-compartment model for CA pyramidal neuron cells

In our model we only take into account fast-activating ionic currents that are known to contribute to ADP and affect the model behaviour over relatively short periods of time (up to 500 ms). The model considers the following ionic currents: two  $\text{Na}^+$ -currents, one transient ( $I_{\text{Na}_T}$ ) and one persistent ( $I_{\text{Na}_P}$ ); two  $\text{Ca}^{2+}$ -currents, one T type ( $I_{\text{Ca}_T}$ ) and one high-voltage activated ( $I_{\text{Ca}_H}$ ); and three  $\text{K}^+$ -currents, delayed rectifier ( $I_{\text{K}_{\text{DR}}}$ ), M type ( $I_{\text{K}_M}$ ), and leak ( $I_L$ ). We use Hodgkin-Huxley formalism (Hodgkin and Huxley, 1952) to represent the rate of change of the membrane potential:

$$C_m \frac{dV}{dt} = -I_{\text{Na}_T} - I_{\text{Na}_P} - I_{\text{Ca}_T} - I_{\text{Ca}_H} - I_{\text{K}_{\text{DR}}} - I_{\text{K}_M} - I_L + I_{\text{app}}, \quad (2.1)$$

where  $C_m$  is the membrane capacitance. The ionic currents are modelled as:

$$\begin{aligned} I_{Na_T} &= g_{Na_T} m_{Na_T}^3 h_{Na_T} (V - E_{Na}), \\ I_{Na_P} &= g_{Na_P} m_{Na_P} (V - E_{Na}), \\ I_{Ca_T} &= g_{Ca_T} m_{Ca_T}^2 h_{Ca_T} (V - E_{Ca}), \\ I_{Ca_H} &= g_{Ca_H} m_{Ca_H}^2 h_{Ca_H} (V - E_{Ca}), \\ I_{K_{DR}} &= g_{K_{DR}} m_{K_{DR}} h_{K_{DR}} (V - E_K), \\ I_{K_M} &= g_{K_M} m_{K_M} (V - E_K), \\ I_L &= g_L (V - E_L). \end{aligned}$$

and the gating variables are of the form

$$\frac{dx}{dt} = \frac{x_\infty - x}{\tau_x}, \quad (2.2)$$

with  $x \in \{m_{Na_T}, h_{Na_T}, m_{Na_P}, m_{Ca_T}, h_{Ca_T}, m_{Ca_H}, h_{Ca_H}, m_{K_{DR}}, h_{K_{DR}}, m_{K_M}\}$ . The activation and inactivation steady-state functions  $x_\infty$  of the respective currents are given in Boltzmann form:

$$x_\infty = \frac{1}{1 + \exp(-(V - V_x)/k_x)},$$

and the time scales  $\tau_x$  are all constant, except for the transient  $Na^+$ -channel, namely,

$$\tau_{h_{Na_T}}(V) = 0.2 + 0.007 \exp(\exp(-(V - 40.6)/51.4)), \quad (2.3)$$

is modeled as voltage dependent in order to obtain a better fit for our data.

The parameters of the pyramidal neuron model are given in Table 2.1. In the following section we validate our model against CA1 and CA3 current-clamp experiments by varying the maximal conductances ( $g_x$ ). Therefore, these values are not included in Table 2.1, but given in Section 2.3; see Table 2.2. Most of the model parameters in Table 2.1 are determined by voltage-clamp experimental measurements (Blackmer et al., 2009; Destexhe and Bal, 2009; Golomb et al., 2006; Liu et al., 2003; Yaari et al., 2007; Yue and Yaari, 2004, 2006; Yue et al., 2005); an example is shown in Figure 2.2(a) for the  $Na^+$ -current. Figures 2.2(a), (b) and (c) show the steady-state activation and inactivation functions  $m_{Na_{T\infty}}$ ,  $h_{Na_{T\infty}}$  and  $m_{Na_{P\infty}}$  of the  $Na^+$ -channel currents,  $m_{Ca_{T\infty}}$ ,  $h_{Ca_{T\infty}}$ ,  $m_{Ca_{H\infty}}$  and  $h_{Ca_{H\infty}}$  of the  $Ca^{2+}$ -channel currents, and  $m_{K_{DR\infty}}$ ,  $h_{K_{DR\infty}}$  and  $m_{K_{M\infty}}$  of the  $K^+$ -channel currents, respectively. The curve in Figures 2.2(d) illustrates the behaviour of the time constant  $\tau_{h_{Na_T}}$  of the transient  $Na^+$ -channel.

**Table 2.1.** Parameter values of the pyramidal neuron model.

Parameter	Value	Unit	Parameter	Value	Unit
$C_m$	1.0	$\mu\text{F}/\text{cm}^2$	$\tau_{h_{\text{CaT}}}$	32.0	ms
$E_{\text{Na}}$	60.0	mV	$V_{m_{\text{CaH}}}$	-15.0	mV
$E_K$	-85.0	mV	$k_{m_{\text{CaH}}}$	5.0	mV
$E_{\text{Ca}}$	90.0	mV	$\tau_{m_{\text{CaH}}}$	0.08	ms
$E_L$	-65.0	mV	$V_{h_{\text{CaH}}}$	-60.0	mV
$V_{m_{\text{NaT}}}$	-37.0	mV	$k_{h_{\text{CaH}}}$	-7.0	mV
$k_{m_{\text{NaT}}}$	5.0	mV	$\tau_{h_{\text{CaH}}}$	300.0	ms
$V_{h_{\text{NaT}}}$	-75.0	mV	$V_{m_{\text{KDR}}}$	-5.8	mV
$k_{h_{\text{NaT}}}$	-7.0	mV	$k_{m_{\text{KDR}}}$	11.4	mV
$V_{m_{\text{NaP}}}$	-47.0	mV	$\tau_{m_{\text{KDR}}}$	1.0	ms
$k_{m_{\text{NaP}}}$	3.0	mV	$V_{h_{\text{KDR}}}$	-68.0	mV
$V_{m_{\text{CaT}}}$	-54.0	mV	$k_{h_{\text{KDR}}}$	-9.7	mV
$k_{m_{\text{CaT}}}$	5.0	mV	$\tau_{h_{\text{KDR}}}$	1400.0	ms
$\tau_{m_{\text{CaT}}}$	2.0	ms	$V_{m_{\text{K_M}}}$	-30.0	mV
$V_{h_{\text{CaT}}}$	-65.0	mV	$k_{m_{\text{K_M}}}$	10.0	mV
$k_{h_{\text{CaT}}}$	-8.5	mV	$\tau_{m_{\text{K_M}}}$	75.0	ms

## 2.3 Model validation

We validate the pyramidal neuron model by simulating experimental responses of a typical neuron cell from the CA1 and CA3 areas (see Figure 2.1). The goal is to identify a set of maximal conductances that reproduce an example of ‘avarage’ CA1 and CA3 pyramidal neurons. We compare model simulations to two major types of current-clamp experiments: short- and long-current stimuli. The long-stimulus experiment is the application of a current injection with a prespecified amplitude that lasts 500 ms. The amplitude is typically 100, 200 or 300 pA. The injection amplitudes in the model are then 1, 2, 3  $\mu\text{A}/\text{cm}^2$ , respectively, because the model takes into account current densities and we simulate a whole-cell current-clamp experiment of a pyramidal neuron with a typical somatic capacitance between 90–120 pF. In the short-stimulus experiment the current injection is applied for 2 ms and the amplitude is much larger, namely, 2 nA. In the model we set the amplitude of the applied current accordingly to 20  $\mu\text{A}/\text{cm}^2$ . In some experiments the cell is made genotype independent by fixing its resting potential to a specific value that is slightly different from the physiological value (Brown and Randall, 2009). To achieve this, the cells are pre-stimulated with a steady-state current injection of an appropriate amplitude. In the model we set the resting potential to the required level by using a nonzero base value of the injected current.

In order to validate the model against the experimental results, we also compare a number of model-derived quantities that correspond to measured electrophysiological properties (Brown and Randall, 2009). These are the action-potential threshold, the membrane resting potential

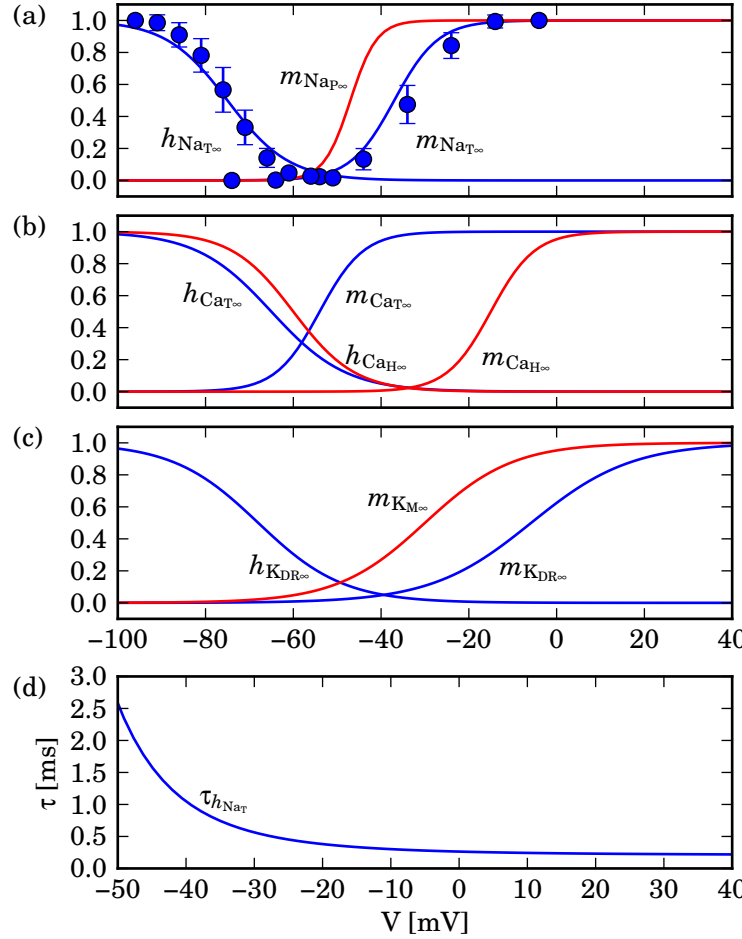


**Figure 2.2.** Channel kinetics used in the pyramidal neuron model; panels (a), (b) and (c) show (in)activation functions of  $\text{Na}^+$ -,  $\text{Ca}^{2+}$ - and  $\text{K}^+$ -channel currents, respectively; experimental measurements used to determine  $\text{Na}^+$ -current (in)activation parameters are depicted as blue dots in panel (a) with standard deviations marked by the error bars; panel (d) shows the time rate of the transient  $\text{Na}^+$ -channel.

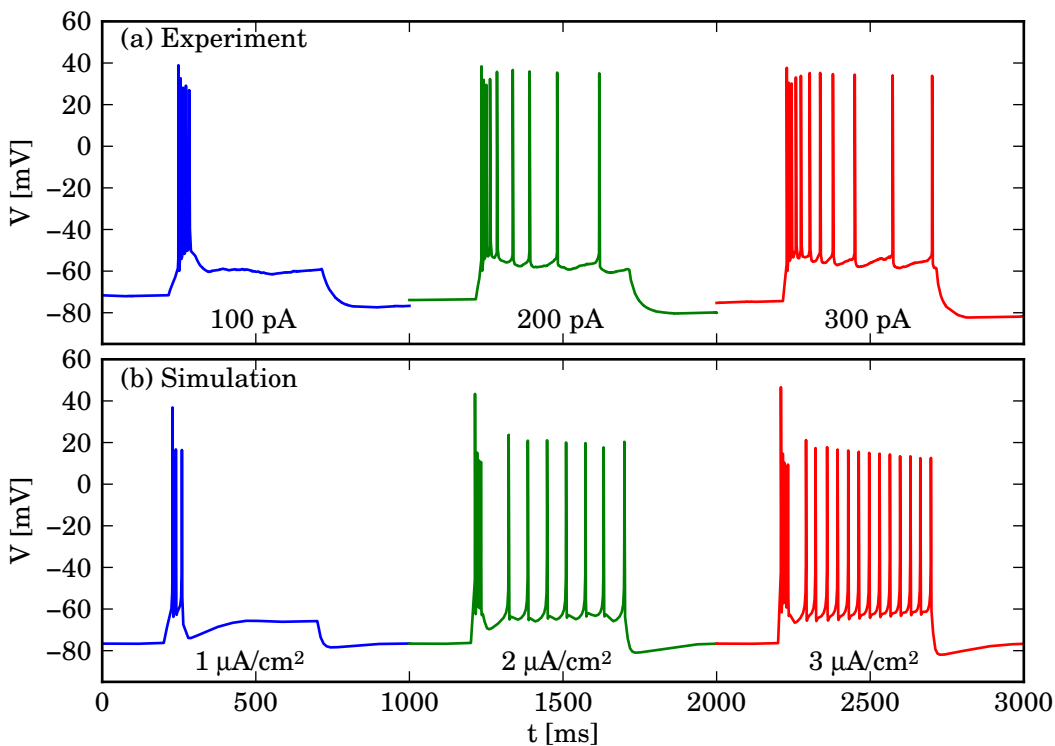
and the action-potential peak. As in (Brown and Randall, 2009), the evaluation of these quantities is done for a current injection of 300 pA, i.e.,  $3 \mu\text{A}/\text{cm}^2$  in our model. For both CA1 and CA3 neurons the membrane resistance is the same and given by  $R_m = 50,000 \Omega/\text{cm}^2$ . Therefore, with a membrane capacitance of  $1 \mu\text{F}/\text{cm}^2$ , the membrane time constant is  $\tau_m = 50 \text{ ms}$ .

### 2.3.1 Long-stimulus experiment

The time traces of the experimental membrane potential of a CA3 pyramidal neuron to 500 ms injections of 100, 200 and 300 pA depolarising currents is shown in Figure 2.3(a); we used the values of the ionic-current kinetics from Table 2.1 and the maximal conductances for a CA3

**Table 2.2.** Maximal conductances (in  $\text{mS/cm}^2$ ) used when modelling a CA1 or a CA3 neuron.

Both CA1 and CA3 neurons		CA3 neuron only		CA1 neuron only	
Parameter	Value	Parameter	Value	Parameter	Value
$g_{\text{NaT}}$	65.0	$g_{\text{K}_{\text{DR}}}$	10.0	$g_{\text{K}_{\text{DR}}}$	9.5
$g_{\text{NaP}}$	0.1	$g_{\text{K}_M}$	1.65	$g_{\text{K}_M}$	0.8
$g_{\text{CaH}}$	0.74	$g_{\text{CaT}}$	0.74	$g_{\text{CaT}}$	0.6
$g_L$	0.02				

**Figure 2.3.** Responses of a CA3 pyramidal neuron and our model to a 500 ms current injection; panel (a) shows experimental responses of a pyramidal cell, where the injected current has amplitudes 100, 200 and 300 pA; panel (b) shows the corresponding responses of the model to 1, 2 and 3  $\mu\text{A}/\text{cm}^2$  of injected current.

neuron given in Table 2.2. The corresponding responses of the model to current injections of magnitudes 1, 2 and 3  $\mu\text{A}/\text{cm}^2$  are shown in Figure 2.3(b). The resting potential for the model with the CA3 parameter set is  $-76.6$  mV for all of the traces in Figure 2.3(b). The action-potential peak for 3  $\mu\text{A}/\text{cm}^2$  current injection is 46.6 mV. The spike-threshold for the experimental and model responses due to highest current injection is approximately  $-58$  mV as shown in Figures 2.3(a) and (b).

As depicted in Figure 2.3 the overall responses of the model to the injected currents agrees with the experimental measurements, and is also in accordance with previously published re-

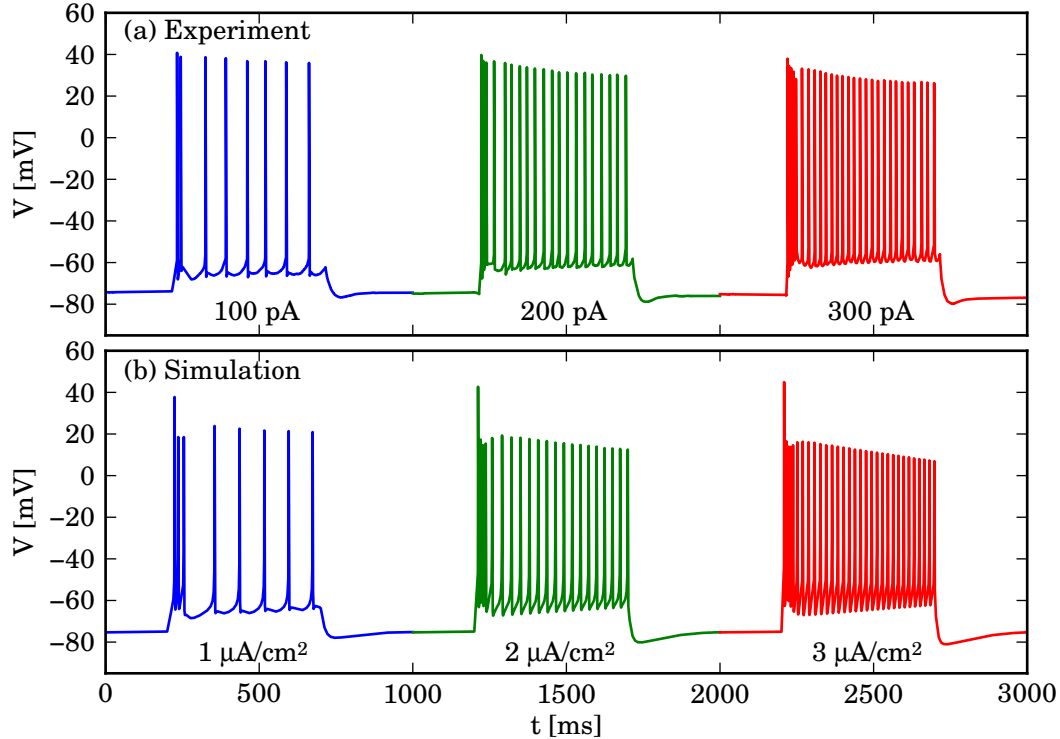


**Figure 2.4.** Responses of a CA1 pyramidal neuron and our model to a 500 ms current injection; panel (a) shows experimental responses of a pyramidal cell, where the injected current has amplitudes 100, 200 and 300 pA; panel (b) shows the corresponding responses of the model to 1, 2 and 3  $\mu\text{A}/\text{cm}^2$  of injected current.

sults in (Andersen et al., 2007; Brown and Randall, 2009). For the lowest current injection of 1  $\mu\text{A}/\text{cm}^2$  only the initial high-frequency burst is produced, which is not followed by other additional spikes, as in Figure 2.1(a). Higher-current injections produce a series of low-frequency action potentials. Also, the frequency and number of spikes increase with the amplitude of the injected current. Since our modelling study is mainly focussed on the fast transient behaviour of the pyramidal cell we neglected more detailed descriptions of the slow  $\text{K}^+$ -currents, like  $\text{Ca}^{2+}$ -dependent currents, which are, nevertheless, present in the pyramidal neurons (Gu et al., 2005). As a result our model does not capture the spike-frequency adaptation, which is evident in the experimental recordings; see Figure 2.3(a).

Our model is also capable of simulating CA1-area neural responses by changing only three maximal conductance values, as indicated in Table 2.2. Such changes may reflect a difference in the number of ion channels among CA1 and CA3 neurons. The time trace of the experimental membrane-potential response of a pyramidal neuron to the injection of 100, 200 and 300 pA depolarising current is shown in Figure 2.4(a). The corresponding responses of the model to the injection of 1, 2 and 3  $\mu\text{A}/\text{cm}^2$  depolarising current is shown in Figure 2.4(b).

The membrane resting potential for the model with the CA1 parameter set is  $-75.5$  mV for all of the traces in Figure 2.4(a). Hence, the value is within the physiological range for this class of neurons (Andersen et al., 2007; Golomb et al., 2006; Yaari et al., 2007). The action-potential peak and threshold for  $3 \mu\text{A}/\text{cm}^2$  current injection are approximately  $44.9$  mV and  $-60$  mV, respectively.

As illustrated in Figure 2.4, the overall response of the model to injected current agrees very well with the experimental data (Figure 2.4(a)), and is also in accordance with previously published results (Andersen et al., 2007; Golomb et al., 2006; Yaari et al., 2007). The response is characterised by relatively regular long-term spike frequencies, with a slight increase just after the start of the current injection. Also, the frequency and number of spikes increase with the amplitude of the injected current. Note that, compared to the CA3 neural response (Figure 2.3(a)), both the number and mean frequency of the action potentials is higher. Moreover, due to inactivation of  $I_{\text{Ca}_H}$  the characteristic modulation of the peaks of the action potential is captured in the response of the model. The gradual increase of the baseline is also reproduced well by the model; this phenomenon is caused by the inactivation of  $I_{\text{K}_{\text{DR}}}$ .

Thus, our results suggest that the CA1 neuron may have slightly fewer transient  $\text{Ca}^{2+}$ -channels and delayed rectifier  $\text{K}^+$ -channels, and far fewer M-type  $\text{K}^+$ -channels. This also emphasises the importance of M-type  $\text{K}^+$ -current for the long-term spiking behaviour and overall excitability as has been demonstrated experimentally in (Yaari et al., 2007; Yue and Yaari, 2004, 2006). Interestingly, model simulations (not shown) indicate that only decreasing the value of  $g_{\text{K}_M}$  for the CA3 neuron parameter set already rapidly increases the number and frequency of action potentials, which is a key feature of CA1-like behaviour.

### 2.3.2 Short-stimulus experiment

We now focus on the model responses to a short current injection. In Figure 2.5 we illustrate model simulations of 2 ms current injections of  $20 \mu\text{A}/\text{cm}^2$  with different (pre-stimulus) base currents that impose a pre-defined resting potential of the cell. The time traces of the membrane potential of the model with the CA3 parameter set and an injected current with base current values of  $0$ ,  $0.4$  and  $0.8 \mu\text{A}/\text{cm}^2$  are shown in Figure 2.5(a). Similarly, the time traces of the membrane potential of the model with the CA1 parameter set and an injected current with base current values of  $0$ ,  $0.2$  and  $0.4 \mu\text{A}/\text{cm}^2$  are shown in Figure 2.5(b). The simulated traces are overlaid to show how the after-depolarisation grows with the changes in the membrane resting potential.

Figure 2.5 illustrates that the model is capable of simulating the experimental results shown in Figure 2.1(b) and (d) and in (Andersen et al., 2007; Brown and Randall, 2009; Golomb et al., 2006; Yaari et al., 2007), including the characteristic shape of the after-depolarisation

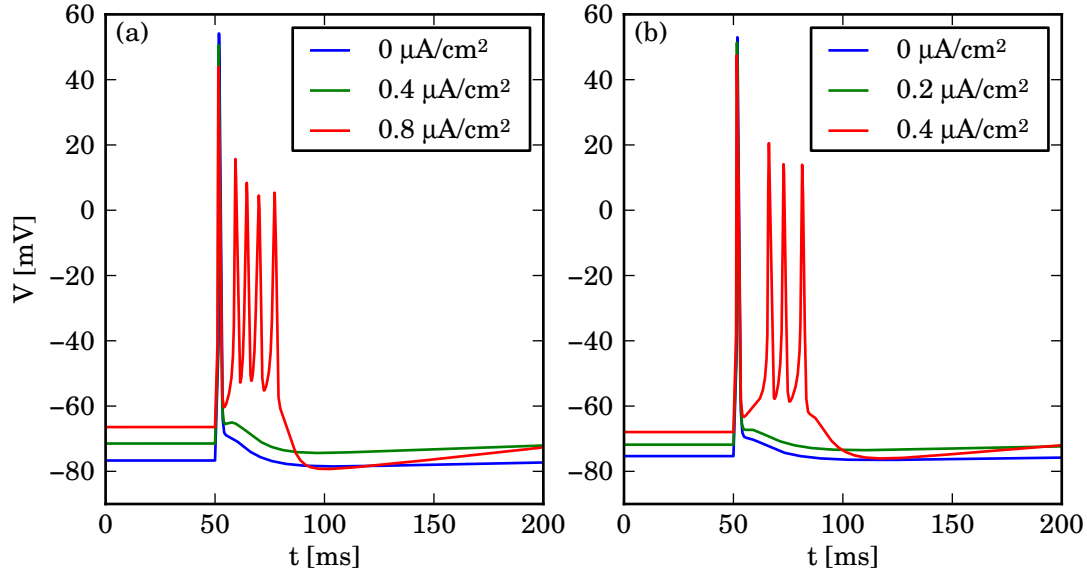


**Figure 2.5.** Responses of the pyramidal neuron model to a 2 ms current injection of  $20 \mu\text{A}/\text{cm}^2$ ; panel (a) shows overlaid responses of the model with the CA3 parameter set to a stimulus with different (pre-stimulating) base currents, namely,  $0 \mu\text{A}/\text{cm}^2$  (blue),  $0.4 \mu\text{A}/\text{cm}^2$  (green) and  $0.8 \mu\text{A}/\text{cm}^2$  (red); similarly, panel (b) shows overlaid responses of the model with the CA1 parameter set to those same stimuli.

‘hump’. Moreover, as reported in (Brown and Randall, 2009; Golomb et al., 2006), as soon as the membrane resting potential exceeds approximately  $-70 \text{ mV}$ , a burst of action potentials is produced, which is clearly illustrated by the highest (red) trace in Figures 2.5(a) and (b). Although the shape of the after-depolarisation is reproduced quite well, the duration of the simulated after-depolarisation is slightly shorter than for the experimental measurements. Our simulations (not shown) suggest that the main reason for this difference is the fact that we use constant values for the time constants of most of the currents; in real cells these are most likely voltage dependent. Note that the duration of the ADP is mainly influenced by the rate of the inactivation of the participating currents, thus, more detailed description of the time constants of these currents may indeed influence the duration of the ADP. Compared to the simulations of the model with the CA3 parameter set in Figure 2.5(a), the amplitude of ADP for the CA1 model is noticeably smaller, which agrees well with experimental observations (Andersen et al., 2007; Golomb et al., 2006; Yaari et al., 2007). The CA1 model response expresses a less prominent ADP and transient burst mainly due to reduction of  $g_{\text{Ca}_T}$  for the CA1 parameter set, which also supports the importance of  $I_{\text{Ca}_T}$  in ADP modulation; this reduction of  $g_{\text{Ca}_T}$  causes less inward current in the low-voltage region, which shapes the amplitude of the ADP. The CA1 parameter set also uses a smaller value for  $g_{\text{K}_M}$ , which significantly reduces the long-term inhibition of the outward current; therefore, the CA1 model response to a long stimulus has more action potentials than the CA3 response.

## 2.4 Excitability sensitivity analysis of the pyramidal neuron model

A necessary step towards a better understanding of the model is to investigate the influence that particular parameter variations have on the behaviour of the system. Such a sensitivity analysis also provides predictions that can be tested in further experimental studies of pyramidal neurons. In Section 2.3 we validated the model against typical responses of CA1 and CA3 neurons, but experiments show that the responses of the pyramidal neurons express much more variable behaviour. We present a sensitivity analysis of our pyramidal neuron based on what we define as the excitability measure. In the subsequent sections we investigate the influence of all maximal conductances for the  $\text{Na}^+$ -,  $\text{Ca}^{2+}$ - and  $\text{K}^+$ -currents on the excitability behaviour of the model.

### 2.4.1 Methods

One of the most widely used measures for neural excitability is the so-called mean instantaneous frequency for the number of first spike pairs. A characteristic feature of the pyramidal neuron response to long-current injection is a higher frequency of the first spike pairs. In order to capture this feature we define the excitability measure:

$$M_e = \sum_{i=1}^n \frac{1}{i^2 ISI_i},$$

as a form of mean instantaneous frequency where the frequency of the initial spike pairs have larger weight. Here,  $n$  is the total number of spike pairs in an  $(n+1)$ -spike response and  $(ISI)_i$  is the inter-spike interval of the pair  $i$ . The pair number is squared to increase the importance of the initial spike-pairs, because the frequency equilibrates rather fast. Note that the total number of spikes changes the (minimal) excitability measure. Hence, for a better comparison, we calculate this value for a constant number of spikes in a spike-train.

It is important to note that the parameters of the gating variables in our model are based on voltage-clamp experimental data and are measured with a high level of confidence. On the other hand voltage clamp allows to measure conductances that are present only on a patch of the neuron's membrane. Since we simulate whole-cell current-clamp recordings, the values of maximal conductances for such simulations are not very well defined. Therefore, we perform an excitability sensitivity analysis with respect to the maximal conductances. These are also most likely to vary between the cells. In our analysis we vary only one conductance and keep all other parameters at their reference values given in Tables 2.1 and 2.2. We use a  $1 \mu\text{A}/\text{cm}^2$  current injection of duration 500 ms, which corresponds to the 100 pA injection

in the experiment. This value was chosen because the pyramidal cells are reported to express more variability in behaviour under low-current injection (unpublished observations of prof. Randall's group). We found that the outcome of the analysis is similar for both types of model CA1 and CA3 neurons, and chose to present the results for CA1 neurons only. We remark here that the excitability measure is not continuous across parameter values where the number of spikes in the response changes. In Figures 2.6, 2.8 and 2.9 we only show the excitability measure over the parameter range for which the response consists of eight spikes (left columns), while the changes in spike number are visualised over a larger range (right columns).

## 2.4.2 The $\text{Na}^+$ -channel currents

Firstly, we investigate the influence of  $\text{Na}^+$ -currents on the excitability of our pyramidal neuron model. Transient  $\text{Na}^+$ -current is known to be responsible for the generation of action potentials (Hodgkin and Huxley, 1952). We chose the parameters for this current based on experimental studies performed at close-to-physiological temperatures of  $33^\circ\text{C}$  (Brown and Randall, 2009), with  $m_{\text{Na}_{T\infty}}$  and  $h_{\text{Na}_{T\infty}}$  as shown in Figure 2.2(a). The activation of this channel is known to be sufficiently fast, so that we neglect its dynamics and assume that it is instantaneous, i.e.,  $m_{\text{Na}_T} = m_{\text{Na}_{T\infty}}$ . Hence,  $I_{\text{Na}_T}$  only contributes to the response during the rising phase of the action potential.

The persistent  $\text{Na}^+$ -current also plays an important role in the generation of action potentials (Golomb et al., 2006; Yue et al., 2005). The kinetics of this channel have been adopted from earlier modelling studies (Golomb et al., 2006). We note that they are also in accordance with recent dynamic-clamp experiments (Destexhe and Bal, 2009). Similar to the transient  $\text{Na}^+$ -channel, persistent  $\text{Na}^+$ -channel activation is known to be very fast (Golomb et al., 2006); hence, we again neglect its dynamics, i.e.,  $m_{\text{Na}_P} = m_{\text{Na}_{P\infty}}$ . The combination of low-voltage activation (see Figure 2.2(a)) and persistence allows this current to contribute actively to the generation of action potentials for the duration of a simulation.

Figure 2.6 shows the sensitivity of excitability to the maximal conductances  $g_{\text{Na}_T}$  and  $g_{\text{Na}_P}$  of the transient and persistent  $\text{Na}^+$ -currents, respectively. Panels (a) and (c) plot the excitability measure versus  $g_{\text{Na}_T}$  and  $g_{\text{Na}_P}$ , respectively, over the range where the model produces an eight-spike response; the changes in the number of spikes are shown in panels 2.6(b) and (d), respectively. Counter-intuitively, the increase of  $g_{\text{Na}_T}$  results in a decrease of both the excitability measure and the number of spikes (Figures 2.6(a) and (b)). This could be explained by the fact that  $I_{\text{Na}_T}$  mainly influences the amplitude of the action potentials and, hence, an increase in  $I_{\text{Na}_T}$  would activate more outward current. Therefore, in contrast to what one would expect, excitability is indirectly inhibited by an increase of  $g_{\text{Na}_T}$ . On the other hand, a decrease of  $g_{\text{Na}_T}$  causes an increase in the excitability, as a result of the lower inhibition of outward

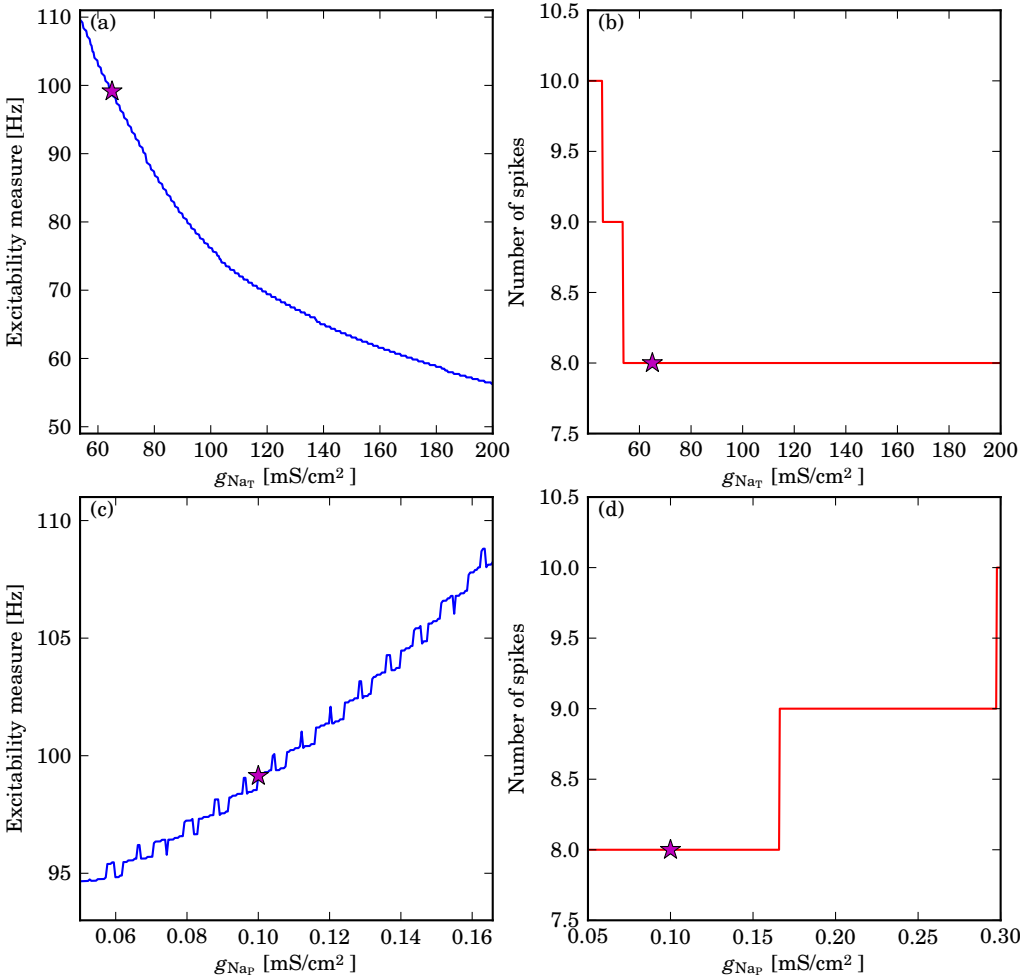


**Figure 2.6.** Sensitivity analysis of the maximal conductances of the  $\text{Na}^+$ -currents; panels (a) and (c) show the excitability measure for the ranges of  $g_{\text{Na}_T}$  and  $g_{\text{Na}_P}$  where the model produces an eight-spike response; panels (b) and (d) show the numbers of spikes in a spike train for  $g_{\text{Na}_T}$  and  $g_{\text{Na}_P}$ , respectively; the original values of the maximal conductances are marked by a (magenta) star.

currents. Since  $g_{\text{Na}_T}$  is the same for CA1 and CA3 neurons in our model, the changes in this parameter have the same effect for both types of cells.

The influence of  $g_{\text{Na}_P}$  on the excitability of the model is more in line with intuition. As shown in Figure 2.6(c) the increase in  $I_{\text{Na}_P}$  produces higher-frequency action potentials. Note that the value of the frequency measure is much larger than for  $g_{\text{Na}_T}$ . On the other hand,  $g_{\text{Na}_P}$  has little influence on the number of spikes, as illustrated in Figure 2.6(d), which reflects the low-voltage activation of this current. Note also that very small changes of  $g_{\text{Na}_P}$ , compared to  $g_{\text{Na}_T}$ , increase the value of the excitability measure quite dramatically. Despite the fact that the value of  $g_{\text{Na}_P}$  in our model is the same for both the CA1 and CA3 parameter sets, the high

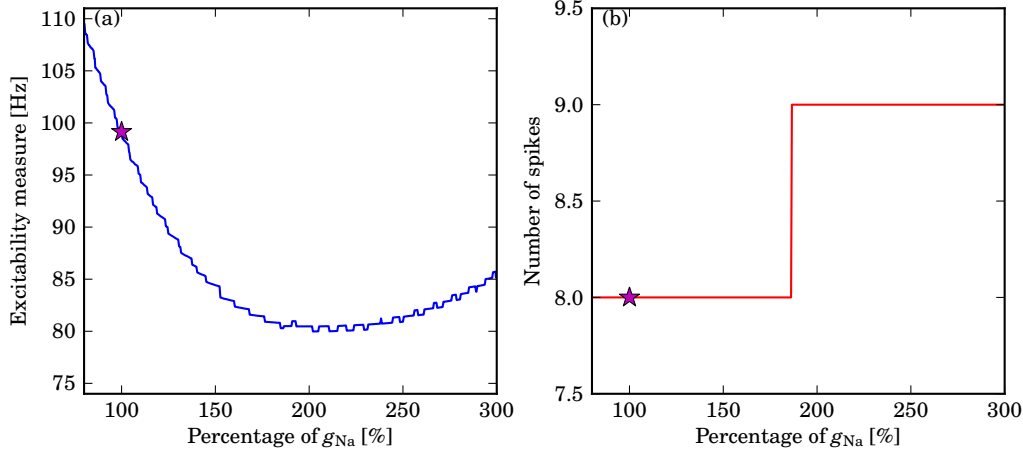


**Figure 2.7.** Sensitivity analysis of the maximal conductance of the combined  $\text{Na}^+$ -currents; panel (a) shows the excitability measure ranging over the given percentages of  $g_{\text{Na}}$ ; the original value of the maximal conductance is marked by a (magenta) star.

sensitivity to changes in this parameter can induce the variability of the neurons' responses reported in the experimental studies of mainly CA3 pyramidal cells (Brown and Randall, 2009; Migliore et al., 1995; Safiulina et al., 2008; Scharfman, 1993; Traub et al., 1991; Wong and Prince, 1981).

Due to a lack of pharmacological tools to influence  $I_{\text{NaP}}$  selectively, it is very hard to separate this current experimentally from the total  $\text{Na}^+$ -current (Destexhe and Bal, 2009). Therefore, in order to compare with experimental data, we investigate the influence of both currents on the excitability. For this purpose we use a common parameter that modifies the percentages of  $g_{\text{NaT}}$  and  $g_{\text{NaP}}$  that are active in a given simulation run by the same factor. Here, the values from the CA1 set are used as the reference values. As before, the excitability measure and the number of spikes are plotted versus the percentage of total  $I_{\text{Na}}$  in Figures 2.7(a) and (b), respectively. The effect of simulated change in both  $\text{Na}^+$ -currents produces a parabola-like characteristic curve, as shown in Figure 2.7(a). Figure 2.7 clearly illustrates that either an increase or decrease of  $I_{\text{Na}}$  can result in an increase of our neural excitability measure. In the studied interval, the increase of  $I_{\text{Na}}$  changes the number of spikes from eight to nine, as shown in Figure 2.7(b). Thus, our result suggests that there exists a minimum  $I_{\text{Na}}$  for which any perturbation of the  $\text{Na}^+$ -current could cause an increase in excitability. The analysis also shows how two different parameters that produce opposite excitability effects can cross-influence the response of a neuron. Moreover, it demonstrates how the total ionic current of a particular type can alter a pyramidal cell behaviour.

We observe this effect for the CA3 parameter set as well (not shown). The minimum of excitability is reached, however, for a greater percentage value of the total  $g_{\text{Na}}$ . This may be caused by the fact that the CA3 neuron model has a larger value of  $g_{\text{K}_M}$ , which, in general,

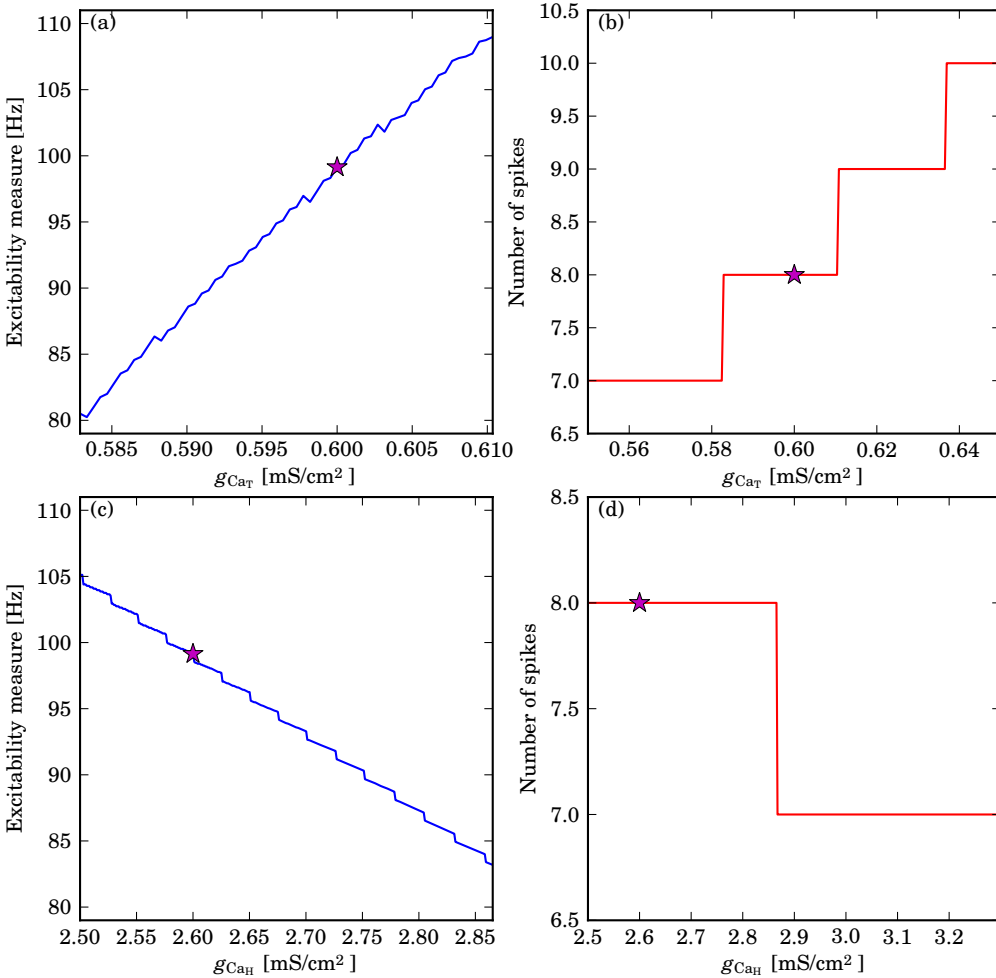


**Figure 2.8.** Sensitivity analysis of the maximal conductances of the  $\text{Ca}^{2+}$ -currents; panels (a) and (c) show the excitability measure for the ranges of  $g_{\text{Ca}_T}$  and  $g_{\text{Ca}_H}$  where the model produces an eight-spike response, respectively; panels (b) and (d) show the numbers of spikes in a spike train for  $g_{\text{Ca}_T}$  and  $g_{\text{Ca}_H}$ , respectively; the original values of the maximal conductances are marked by a (magenta) star.

would cause more inhibition. Hence, more  $I_{\text{NaP}}$  would be needed to compensate the increase in inhibition.

### 2.4.3 The $\text{Ca}^{2+}$ -channel currents

In addition to  $\text{Na}^+$ -channels, recent research shows that  $\text{Ca}^{2+}$ -channels are also actively involved in neural responses to stimuli (Yaari et al., 2007). Moreover,  $\text{Ca}^{2+}$ -channels are found to be present in both CA1 and CA3 pyramidal cells (Jaffe et al., 1994; Yaari et al., 2007). In our model we use two classes of  $\text{Ca}^{2+}$ -channels, low-voltage-activated T-type  $\text{Ca}^{2+}$ -channels and a general class of high-voltage-activated  $\text{Ca}^{2+}$ -channels. The influence of the maximal

conductances of these currents on the neural excitability in the model is shown in Figure 2.8. The excitability measures for the eight-spike responses as functions of  $g_{\text{Ca}_T}$  and of  $g_{\text{Ca}_H}$  are shown in Figures 2.8(a) and (c), respectively. Figures 2.8(b) and (d) illustrate the changes in the numbers of spikes as the maximal conductances vary.

The kinetic parameters of a T-type  $\text{Ca}^{2+}$ -channel in our model are based on (Blackmer et al., 2009) and our data. To model this current, we use similar values to those published in (Jaffe et al., 1994; Lazarewicz et al., 2002; Migliore et al., 1995; Xu and Clancy, 2008). As shown in Figure 2.2(b), the T-type  $\text{Ca}^{2+}$ -channel operates in the low-voltage interval and hence is an important building block of the neuron’s ADP (Yaari et al., 2007). The inactivation of  $I_{\text{Ca}_T}$  is a relatively slow process (see  $\tau_{h_{\text{Ca}_T}}$  in Table 2.1) that contributes to the transient excitability in the beginning of the current-injection stimulus. The main role of  $I_{\text{Ca}_T}$  in the model is to bring the membrane potential up, near the action-potential threshold, so that the other currents produce a spike.

Because of the low-voltage activation, similar to  $I_{\text{NaP}}$ , a change of  $g_{\text{Ca}_T}$  also has a large effect on the excitability properties of the model. The excitability measure has a steep slope and reaches quite high values within a small interval of  $g_{\text{Ca}_T}$  (Figure 2.8(a)). Moreover, Figure 2.8(b) illustrates that even small changes of  $g_{\text{Ca}_T}$  in the given interval profoundly influence the number of spikes. Note that we were able to perform the analysis only for a relatively small interval of  $g_{\text{Ca}_T}$ ; this is due to the fact that for values below  $0.4 \text{ mS/cm}^2$  the inhibition of the outward currents is too large and no action potentials are generated. On the other hand for  $g_{\text{Ca}_T} > 0.65 \text{ mS/cm}^2$  the model exhibits bursting behaviour. The CA3 neuron model has  $g_{\text{Ca}_T} = 0.74 \text{ mS/cm}^2$ , which is above the bursting boundary for the CA1 parameter set. The reason why CA3 neurons may tolerate more  $I_{\text{Ca}_T}$  is due to the higher inhibition from the outward currents, i.e., larger values of  $g_{\text{K}_M}$  and  $g_{\text{K}_{DR}}$ . These results establish the relatively high sensitivity of the model to changes in  $I_{\text{Ca}_T}$ . Moreover, it suggests that the concentration of  $\text{Ca}^{2+}$  can indirectly affect the pyramidal-cell behaviour, because it can change the amount of active  $I_{\text{Ca}_T}$  through the Nerst potential of  $\text{Ca}^{2+}$ . In addition, analysis of both  $I_{\text{NaP}}$  and  $I_{\text{Ca}_T}$  shows that low-voltage activated currents, which are important elements of neural excitability, can also cause bursting of the pyramidal neuron.

The high-voltage-activated  $\text{Ca}^{2+}$ -channel current plays a role in shaping the action potentials in our model. In particular, it determines their amplitudes. The gating parameters for this channel are based on values from (Blackmer et al., 2009; Liu et al., 2003) and our data; their values are similar to those used in (Jaffe et al., 1994; Lazarewicz et al., 2002; Migliore et al., 1995; Xu and Clancy, 2008). To capture the effect of amplitude modulation observed in pyramidal cells, we allow  $I_{\text{Ca}_H}$  to inactivate. Note that this inactivation is a slow process (see  $\tau_{h_{\text{Ca}_H}}$  in Table 2.1), so that the inactivation of  $I_{\text{Ca}_H}$  is only significant for long spike-trains with a higher mean frequency.

The sensitivity analysis of  $g_{\text{Ca}_H}$  produces counterintuitive results similar to those for  $g_{\text{Na}_T}$ . Since it affects mostly the amplitudes of the action potentials, the increase of  $g_{\text{Ca}_H}$  results in a decrease of the excitability measure, as shown in Figure 2.8(c). Note that the values of the excitability measure are not as high as for  $g_{\text{Ca}_T}$ , which means that the frequency is less affected. Figure 2.8(d) shows that, in the given interval,  $g_{\text{Ca}_H}$  has only little influence on the number of spikes. Further increases of  $g_{\text{Ca}_H}$  above  $3.3 \text{ mS/cm}^2$  eventually cause a depolarised state instead of action potentials. For both CA1 and CA3 parameter sets we find equivalent effects on excitability due to changes in  $g_{\text{Ca}_H}$ . Importantly these effects are also similar to the influence of changes in total  $\text{Na}^+$ -current in the model. Therefore, a decrease in  $g_{\text{Ca}_H}$  may be a cause for hyper-excitability as well.

#### 2.4.4 The $\text{K}^+$ -channel currents

The main outward current in our model is the  $\text{K}^+$  delayed rectifier, representing a number of fast  $\text{K}^+$ -currents. In the model the  $\text{K}^+$  delayed rectifier is a transient current, with a very slow inactivation. This slow inactivation is often neglected in models, because it hardly affects spiking. However, it plays an important role in setting the resting potential of the cell that corresponds to the initial conditions in the model.

It has been shown experimentally that the muscarinic-sensitive  $\text{K}^+$ -channel is important for the ADP of pyramidal cells (Yaari et al., 2007; Yue and Yaari, 2004, 2006). The parameters we used are based on (Oldfield et al., 2009). The muscarinic-sensitive  $\text{K}^+$ -current  $I_{\text{K}_M}$  does not inactivate (Yue and Yaari, 2004, 2006). Hence, it is active for a wide range of values of the membrane potential. Because  $I_{\text{K}_M}$  activates slowly, its contribution to the spike inhibition is lower at the beginning of the current injection.

Figure 2.9 shows the influence of these maximal conductances on the behaviour of our model. Figure 2.9(a) and (c) depict the excitability measures for the eight-spike responses as functions of  $g_{\text{K}_{\text{DR}}}$  and  $g_{\text{K}_M}$ , respectively. The changes in the number of spikes are show in Figure 2.9(b) and (d). Both outward currents have a significant inhibitory influence on the model excitability, as is reflected by the negative slopes of the excitability measures shown in Figures 2.9(a) and (c). Note that  $g_{\text{K}_M}$  varies on a much smaller scale than  $g_{\text{K}_{\text{DR}}}$  (Figure 2.9(c)). The excitability measure in Figures 2.9(a) and (c) appear to have similar slopes, but small changes of  $g_{\text{K}_M}$  have a greater influence on the overall excitability. Evidently, small changes of  $g_{\text{K}_M}$  cause profound changes of both frequency and number of spikes. Moreover, the maximal values of the excitability measure are quite large compared to the previous cases, which indicates that changes of this current have a substantial effect on the spike frequency.

Small changes in  $g_{\text{K}_{\text{DR}}}$  and  $g_{\text{K}_M}$  also have a significant effect on the number of spikes. Figure 2.9(d) illustrates the influence of  $g_{\text{K}_M}$  on the number of spikes; this is in line with

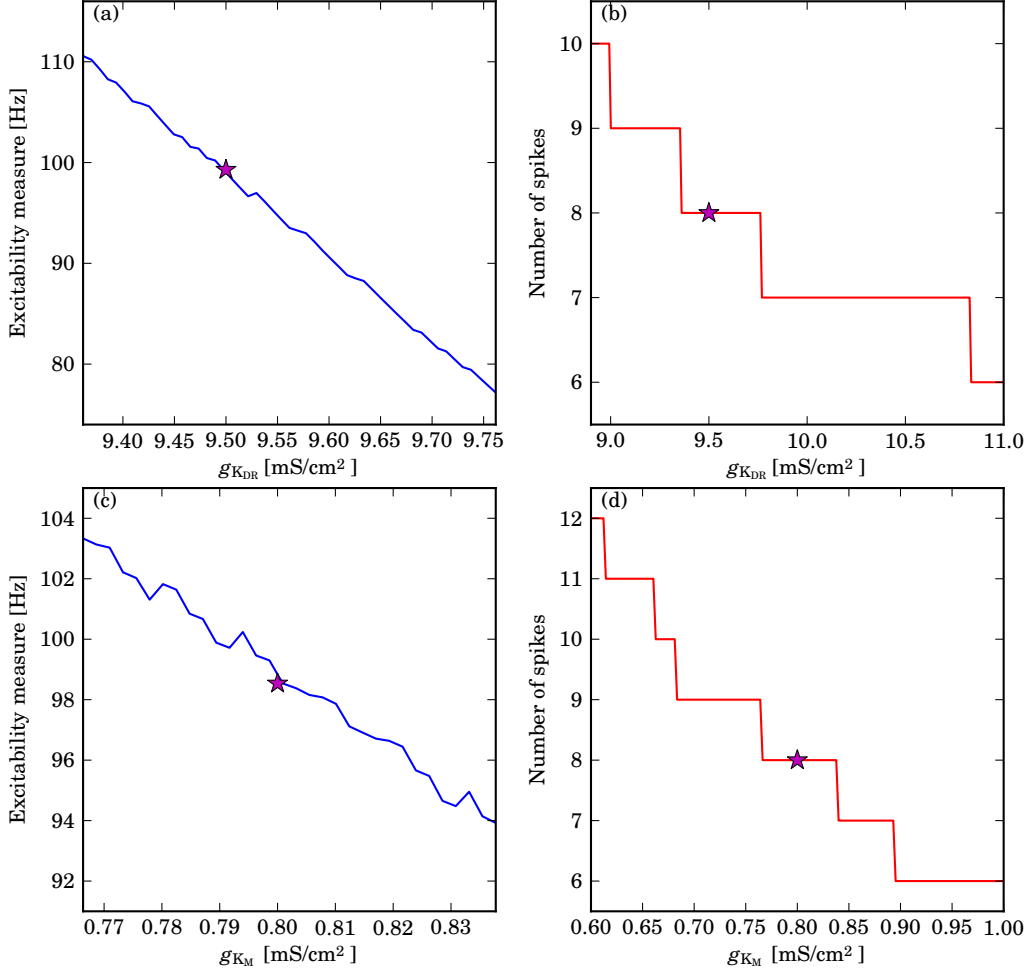


**Figure 2.9.** Sensitivity analysis of the maximal conductances of the  $K^+$ -currents; panels (a) and (c) show the excitability measure for the ranges of  $g_{K_{DR}}$  and  $g_{K_M}$  where the model produces an eight-spike response, respectively; panels (b) and (d) show the number of spikes in a spike train for  $g_{K_{DR}}$  and  $g_{K_M}$ , respectively; the original values of the maximal conductances are marked by a (magenta) star.

our previous finding for the CA3 neuron model, where a reduction of  $g_{K_M}$  also led to regular spiking behaviour with an increased number of spikes. Since the value of  $g_{K_M}$  for the CA1 parameter set is lower than for the CA3 parameter set, the long-lasting inhibition caused by this current is smaller; see Table 2.2. Therefore, the amount of inward current in the low-voltage region is larger, which allows the membrane potential to cross the spiking-threshold much more often. Hence, more action potentials can be generated. Moreover, because  $I_{K_M}$  is a slow current, it deactivates slowly as well. Hence, lower  $g_{K_M}$  causes less active  $I_{K_M}$  in the low-voltage region, which directly influences the inward currents.

We started the excitability sensitivity analysis from  $g_{K_{DR}} = 8$  mS/cm<sup>2</sup>, because below

that value our model exhibits bursting. On the other hand, further decreases of  $g_{K_M}$  toward zero produce tonic-spiking behaviour without any bursts in the model; this could be explained by the fact that  $I_{K_M}$  is slow and has a long-lasting effect on the spiking behaviour of the model.

## 2.5 Identification of after-depolarisation and the initial burst

In this section we investigate the mechanisms that shape the ADP and the transient burst. As a starting point we formulate a mathematical definition of ADP in order to identify the roles of the ionic currents for ADP generation and modulation in the model. We then discuss the connection between the ADP and transient bursts in the long-stimulus experiment.

### 2.5.1 Mathematical formulation of after-depolarisation

Although the phenomenon of ADP has been investigated experimentally for a number of years and its significance for neural excitability has been recognised, there have not been any attempts to formalise this behaviour. Generally ADP is defined as a positive deflection of the membrane potential immediately after an action potential (Izhikevich, 2006).

The ADP is a relatively slow transient process, that takes place below the spiking threshold of the pyramidal neuron as shown in the previous sections. Hence, the absolute value of the derivative  $dV/dt$  of the membrane potential should be below threshold. According to (Naundorf et al., 2006) an action potential occurs when  $dV/dt$  exceeds 20V/s. Hence, during ADP we require:

$$\frac{dV}{dt} < 20 \text{ [V/s].} \quad (2.4)$$

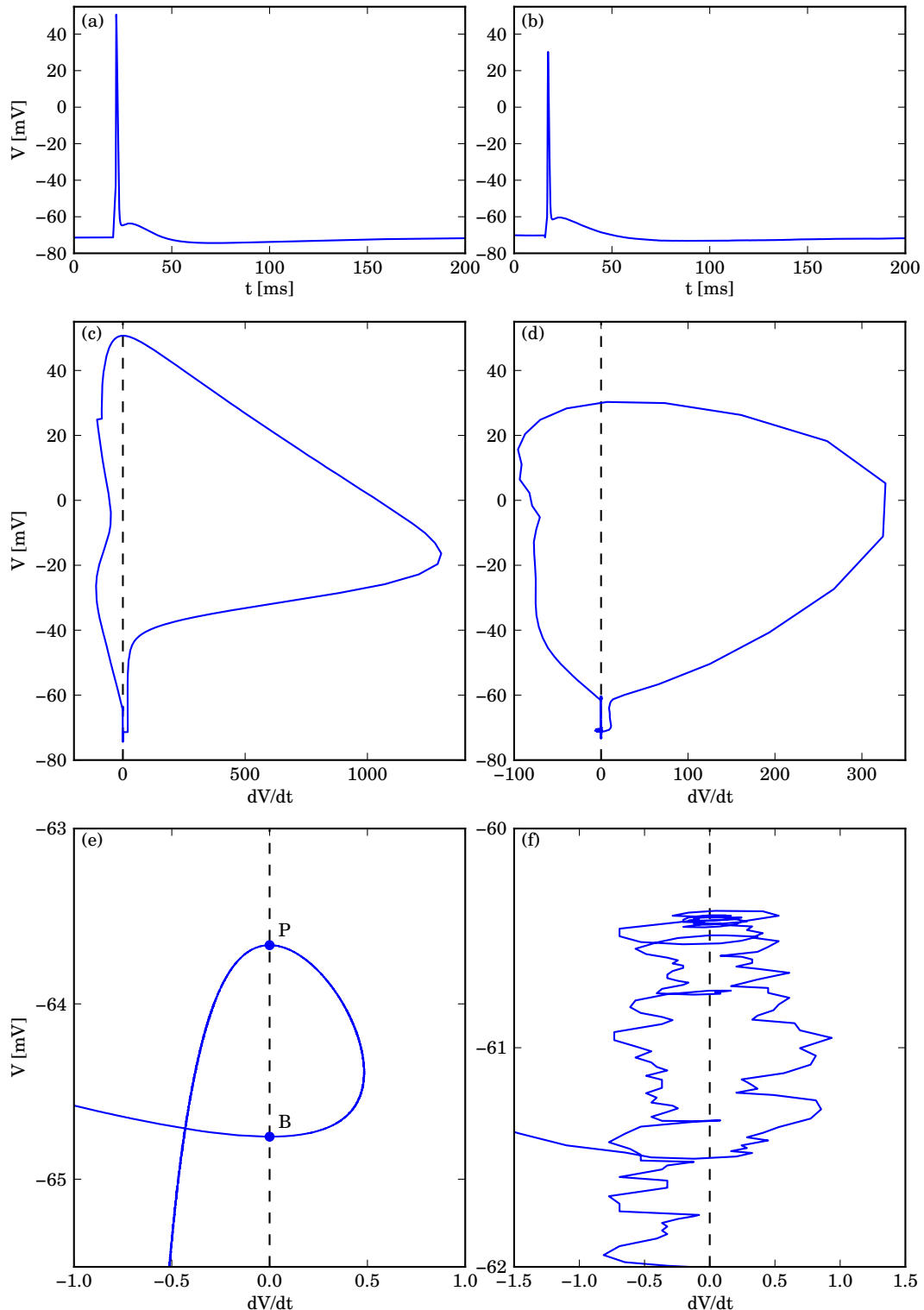
The positive deflection of the membrane potential, as observed in the time traces in Figures 2.3(a) and 2.4(a), is characterised by a local minimum  $B$  at a time  $t = t_B > 0$  and a local maximum  $P$  for some  $t = t_P > t_B$  of  $V$ , which define the beginning and the peak of the ADP, respectively. Hence,  $B$  and  $P$  satisfy:

$$\frac{dV}{dt}(t_B) = 0 \quad \text{and} \quad \frac{d^2V}{dt^2}(t_B) > 0, \quad (2.5)$$

$$\frac{dV}{dt}(t_P) = 0 \quad \text{and} \quad \frac{d^2V}{dt^2}(t_P) < 0, \quad (2.6)$$

such that  $dV/dt \geq 0$  in the time interval  $(t_B, t_P)$ . We use (2.4) to distinguish ADP from a genuine action potential by imposing the following constraint:

$$\frac{dV}{dt}(t) < 20, \text{ for all } t_B \leq t \leq t_P.$$



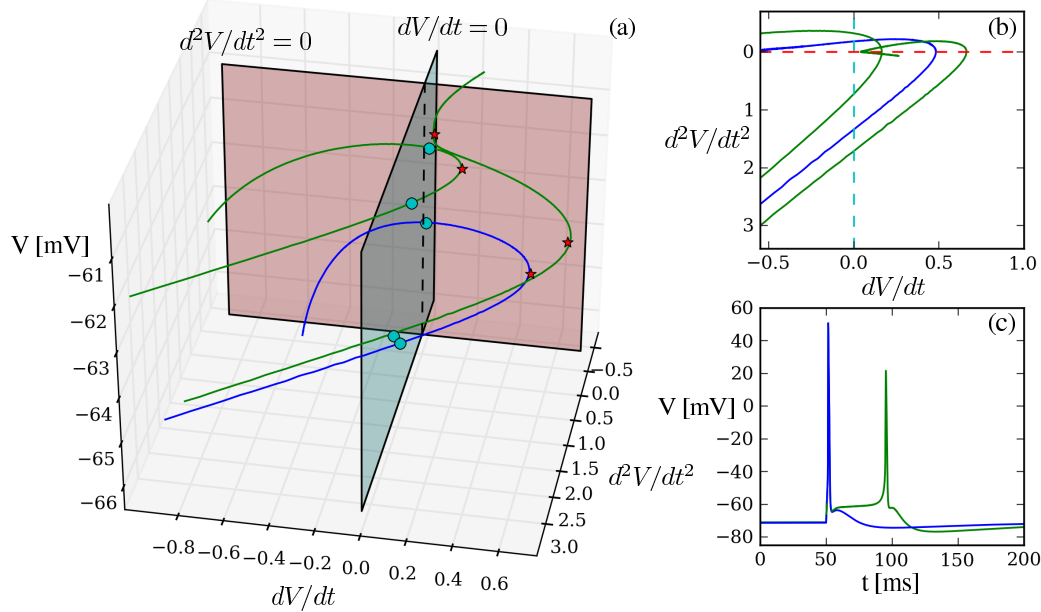
**Figure 2.10.** ADP in a CA3 pyramidal neuron for the model (first column) and the experiment (second column); panel (a) shows the time series of  $V$  for the model with a holding current of  $0.4 \mu\text{A}/\text{cm}^2$ ; panel (b) shows the time series of  $V$  for an experimental sweep; panels (c) and (d) show the membrane potential  $V$  versus  $dV/dt$ ; the dashed line marks  $dV/dt = 0$ ; panels (e) and (f) show an enlargement of the ADP region, with the beginning  $B$  and peak  $P$  of the ADP marked for the model in panel (e).

Figure 2.10 depicts ADP for a model simulation and an example of experimental measurements. In the model simulation the holding current was set to  $0.4 \mu\text{A}/\text{cm}^2$  to pre-define a resting potential of approximately  $-72 \text{ mV}$ , as was done in the experiments. The time traces shown in Figures 2.10(a) and (b) represent the model simulation and experimental data, respectively. We use finite-difference approximation to estimate  $dV/dt$  numerically. For better comparison, we used the same approximation method for both data sets, because we did not observe a significant difference when deriving the values of  $dV/dt$  directly from the model equations. We used a three-point moving average (mean) to smooth the experimental data. More sophisticated processing of experimental measurements could be beneficial when the ADP is small. Figures 2.10 (c) and (d) show  $V$  versus  $dV/dt$  for the simulation and experiment, respectively. The vertical dashed line denotes the nullcline  $dV/dt = 0$ . The large excursions in Figures 2.10(c) and (d) correspond to the action potentials generated by the current injection in the model and experiment, respectively. Although the shape of the derivative plot from our model simulation agrees with the experimental data, the maximum derivative is much higher compared to the experimental data. This is due to the assumption that the kinetics of  $\text{Na}^+$  currents are instantaneous, which imposes an almost instantaneous growth of the action potential that results in an arbitrarily large derivative. The ADP itself is a much slower process, which takes place in the enlarged region shown in Figures 2.10(e) and (f); the beginning point  $B$  and the peak value  $P$  of ADP for the model are marked on panel (e), but the ADP loop is also clearly visible in panel (f), despite the presence of noise for the experimental data. After the trajectory crosses the  $V$ -nullcline at  $B$ , which marks the beginning of ADP, the voltage  $V$  grows until the trajectory crosses the  $V$ -nullcline for a second time at  $P$ , which marks the peak of ADP. Note that  $dV/dt$  remains well below its threshold value of  $20 \text{ V/s}$ . The maximal value of  $dV/dt$  satisfies  $d^2V/dt^2 = 0$  and corresponds to the point where ADP turns back toward the  $V$ -nullcline, while  $dV/dt$  remains positive.

The ADP takes place as soon as there are two local subthreshold extrema of the membrane potential. Therefore, the onset of ADP is the degenerate case where the trajectory develops a cubic tangency. Effectively,  $B$  and  $P$  coincide so that there exist a time  $t_{BP}$  after the action potential such that

$$\frac{dV}{dt}(t_{BP}) = 0 \quad \text{and} \quad \frac{d^2V}{dt^2}(t_{BP}) = 0, \quad (2.7)$$

that is, in the projection of  $V$  versus  $dV/dt$ , the trajectory is tangent to the  $V$ -nullcline (we assume that  $d^3V/dt^3(t_{BP}) \neq 0$ ). It can be very hard to determine the onset of ADP using just time series, whereas the derivative plot does this unmistakably both for the simulations and the experimental measurements. Moreover, we can identify ADP-like behaviour, where  $dV/dt$  in the peak of the deflection is very close to the  $V$ -nullcline, but  $dV/dt$  is negative. Such ADP-like behaviour can be deceiving when observing the time-trace plot, but it is readily



**Figure 2.11.** Bursting-threshold of the pyramidal neuron model; panel (a) shows trajectory segments of ADP without (blue) and with (green) a secondary spike in  $(d^2V/dt^2, dV/dt, V)$ -space; the intersections of the trajectory segments with the planes  $dV/dt = 0$  (cyan) and  $d^2V/dt^2 = 0$  (red) are marked by dots and stars, respectively; panel (b) presents a top view, namely, the projection onto the  $(dV/dt, d^2V/dt^2)$ -plane, with the projections of  $dV/dt = 0$  (cyan) and  $d^2V/dt^2 = 0$  (red) represented by dashed lines; panel (c) shows the time traces of the two trajectories.

distinguishable from ADP when determined by the derivative analysis.

Using the above approach we can also identify the underlying causes for generation of a burst riding on top of ADP, as presented in Figure 2.5. Following condition (2.4), the action potential is generated when  $dV/dt > 20$  at a time after the trajectory crosses the  $V$ -nullcline. Hence,  $dV/dt$  has to exceed the threshold value before reaching the turning point with  $d^2V/dt^2 = 0$ . Figure 2.11 illustrates this by plotting two trajectories, one with a single (blue) and one with an additional (green) action potential. Panel (a) shows the trajectory segments in the ADP region projected in  $(d^2V/dt^2, dV/dt, V)$ -space. The points where the segments intersect the planes  $dV/dt = 0$  (cyan) and  $d^2V/dt^2 = 0$  (red), that is, the  $V$ - and  $dV/dt$ -nullclines, are marked by dots and stars, respectively. Panel (b) provides a top view of panel (a); the trajectory segments are shown in projection onto the  $(dV/dt, d^2V/dt^2)$ -plane and the dashed lines correspond to the projections of the  $V$ - and  $dV/dt$ -nullclines. Note that the  $d^2V/dt^2$ -axis in Figure 2.11(b) is inverted to match Figure 2.11(a). The time series of the trajectories for the two cases are shown in panel (c). The first (blue) trajectory in Figure 2.11(a) is the same as the one in Figure 2.10(e). After crossing the  $dV/dt$ -nullcline (red plane), the trajectory turns back to the  $V$ -nullcline (cyan plane), which marks the peak of ADP and results in a decrease of  $V$ . The burst trajectory (green) consists of two segments in Fig-

ure 2.11(a); the S-shaped segment corresponds to the action-potential generation on top of the ADP, and the additional loop is the small ‘hump’ after the second spike (see Figure 2.11(c)). The S-shaped trajectory also crosses the  $dV/dt$ -nullcline, i.e.,  $d^2V/dt^2 = 0$ , and turns back toward the  $V$ -nullcline. However, before reaching the  $V$ -nullcline, it crosses the  $dV/dt$ -nullcline again. Thus, after the second crossing,  $dV/dt$  remains positive and an action potential is generated. Hence, the  $dV/dt$ -nullcline plays the role of a bursting-threshold in our model. There also exists a degenerate case where the trajectory produces an inflection point at the intersection of the  $V$ - and  $dV/dt$ -nullclines, at which condition (2.7) is satisfied. Hence, condition (2.7) can also be used to mark the transition to bursting. Therefore, the above definition of the ADP is not only a mathematical formulation of the phenomenon, but as such, allows for more rigorous analysis of the transitions between possible dynamic behaviours of the model.

## 2.5.2 The role of different ionic currents in shaping the after-depolarisation

In the previous section we defined the ADP phenomenon using the first and second derivatives of the membrane potential. We can use this information to determine the contribution of particular currents to the ADP. Both T-type  $\text{Ca}^{2+}$ -channel currents and persistent  $\text{Na}^+$ -channel currents are known to facilitate ADP (Chen and Yaari, 2008; Golomb et al., 2006; Yue et al., 2005). The M-type  $\text{K}^+$ -channel current also mediates this phenomenon and is known to work for low values of the membrane potential (Yue and Yaari, 2004, 2006). Since the ADP is a low-voltage phenomenon, the main currents that play a role in its generation are low-voltage activated. Moreover, the ADP process is relatively slow in comparison to the spike-generation process; see Figure 2.10 and also the time traces in Figure 2.5. Hence, the currents that mediate ADP should be slower than the currents taking part in the process of spike generation.

In our model there are only four currents satisfying this condition, namely,  $I_{\text{NaP}}$ ,  $I_{\text{CaT}}$ ,  $I_{\text{K}_{\text{DR}}}$  and  $I_{\text{K}_M}$ . Note that only these four currents are active in the low-voltage region; the remaining currents are deactivated and effectively equal to zero. In addition, in our model  $I_{\text{NaP}}$  is small in this region compared to the other participating currents. As illustrated in Figure 2.10,  $dV/dt < 0$  for most of the time after the action potential, because the membrane potential tries to return to its equilibrium (i.e. the resting potential). In order to create a time interval  $(t_B, t_P)$  during which  $dV/dt > 0$ , the total inward current must be larger than the total outward current. For low voltages in our model the total inward current is given by the sum of  $I_{\text{NaP}}$  and  $I_{\text{CaT}}$ , and the total outward current is the sum of  $I_{\text{K}_{\text{DR}}}$  and  $I_{\text{K}_M}$ . Therefore, ADP is possible only if an interval  $(t_B, t_P)$  exists such that

$$|I_{\text{NaP}}(t) + I_{\text{CaT}}(t)| > |I_{\text{K}_{\text{DR}}}(t) + I_{\text{K}_M}(t)|, \quad t_B \leq t \leq t_P. \quad (2.8)$$

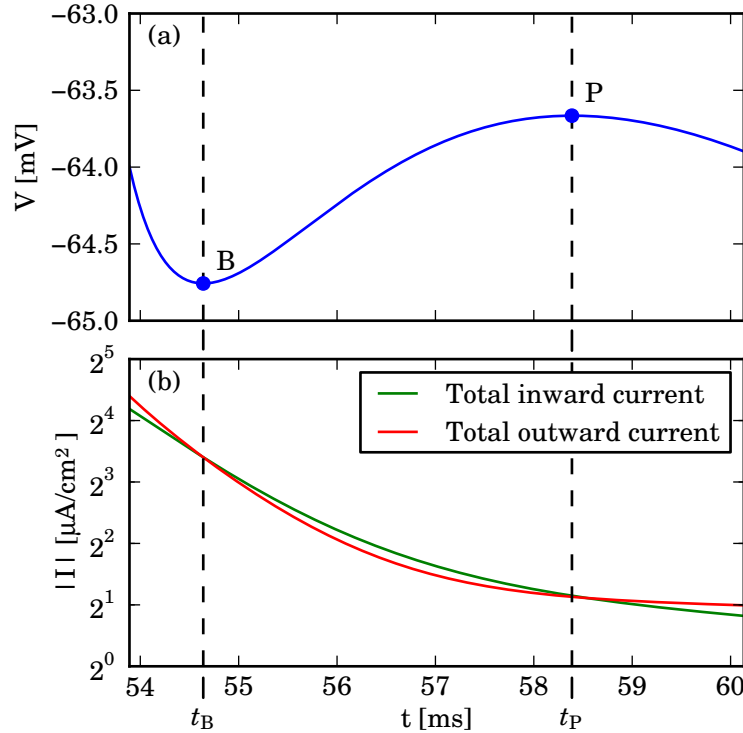


**Figure 2.12.** The relation between inward and outward currents in the model during the ADP. Panel (a) shows a detailed view of the ADP from the time trace shown in Figure 2.10(a), with the beginning and the peak of ADP labelled as B and P, respectively. Panel (b) shows the time traces of the absolute values of the total inward (green) and outward (red) current presented on a  $\log_2$ -scale. Vertical dashed (black) lines in panels (a) and (b) indicate the times  $t_B$  and  $t_P$ , respectively.

In Figure 2.12 we illustrate this condition. Panel (a) shows a detailed view of the time trace of the ADP from Figure 2.10(a), with beginning and peak of the ADP marked by B and P, respectively. Figure 2.12(b) shows the time traces of the absolute values of the total inward and outward currents. The times  $t_B$  and  $t_P$  are indicated in Figure 2.12 by a vertical dashed (black) lines and they almost coincide with the times at which the total inward and outward currents are equal; compare the intersection points of the two curves in Figure 2.12(b). Note that condition (2.8) is satisfied in the interval  $t_B \leq t \leq t_P$ .

Condition (2.8) can be satisfied when there is a difference in the time scales of the currents participating in the ADP. The gating variable  $m_{K_{DR}}$  deactivates rapidly, which causes a reduction of the total outward current just after the action potential. Since  $I_{CaT}$  is the largest inward current, it mainly regulates the amount of the total inward current in the low-voltage area. The activation variable  $m_{CaT}$  of  $I_{CaT}$  has a slightly larger time constant than  $m_{K_{DR}}$  (see Table 2.1). Thus, its deactivation evolves slower than the deactivation of  $I_{K_{DR}}$ , which allows the inward current to grow larger than the total outward current. Hence, there exists a period of time where the rate of change of the membrane potential is dominated by  $I_{CaT}$ . This results in

a positive sign of  $dV/dt$  and the membrane potential increases during this period. The slowest current involved in the ADP, namely,  $I_{K_M}$  mainly controls the duration of this phenomenon.

As shown in Figure 2.5, a sufficiently high base-current injection can result in a burst on top of ADP. In general, ADP is generated by a perturbation in the membrane potential caused by a current injection. Therefore, after the first spike, the cell gradually returns to its resting state. Moreover, all currents evolve on their characteristic time scales, which causes the change in the sign of  $dV/dt$ . Nevertheless, not all currents activate during ADP. In particular, only when the differences between the currents are sufficiently large the membrane potential could reach the threshold for  $\text{Na}^+$ -current activation. The second turn of the trajectory with two spikes in Figure 2.11 is caused by this gradual activation of  $\text{Na}^+$ -currents, which takes place around  $-60$  mV (see Figure 2.2(a)). The activation of additional inward currents cause  $dV/dt$  to increase and eventually generate an additional action potential on top of ADP, as shown in Figures 2.5 and 2.11.

### 2.5.3 After-depolarisation and CA1/3 neural excitability

Recent experimental studies (Brown and Randall, 2009; Golomb et al., 2006; Yaari et al., 2007) suggest that there is a direct relationship between ADP and excitability of pyramidal neurons. In this section we discuss this relationship based on our modelling and experimental results. Since the behaviour of  $dV/dt$ , is determined by the dynamic interactions between the ionic currents in the system, we are able to define ADP in terms of the subthreshold difference of the ionic currents in the model. Figure 2.5(a) shows that a prominent ADP for the CA3 neuron causes the firing of a high-frequency transient burst. In contrast, CA1 neural response is characterised by a lower ADP, as illustrated in Figure 2.5(b), and the corresponding transient burst has a lower frequency. The above analysis suggests that such behaviour could be explained in terms of the amount of inward current that is active in the low-voltage region. In other words, more prominent ADP increases the probability of firing an action potential.

Furthermore, it is important to distinguish between transient excitable behaviour, which is part of the initial burst, and regular excitable behaviour such as spiking. The initial response is indeed very important, because the stimuli, such as synaptic inputs, during physiological conditions are more likely to be short and transient. Based on the above analysis, we suggest that CA3 neurons are more excitable than CA1 because of the higher values of  $dV/dt$ , i.e., the total inward current in the low-voltage region, that results in more prominent ADP and transient bursting.

## 2.6 Conclusion

We presented a unified model of CA1/3 pyramidal cells that was calibrated to, and validated with, recent experimental data obtained at close-to-physiological temperatures. We used this model to unravel the mechanisms that govern ADP and transient bursting behaviour in CA1/3 pyramidal cells. Our analysis of the model suggests a possible explanation for a number of puzzling experimental observations related to hyper-excitability in pathological conditions. Moreover, we defined ADP as a local maximum of the membrane potential. We analysed this phenomenon by using the derivative  $dV/dt$ ; we performed the same analysis also for the experimental measurements. This method of analysis is particularly useful in the study of onset of ADP, which corresponds to a subthreshold cubic tangency of the membrane potential to the  $V$ -nullcline.

In Chapter 4 we use this knowledge about the ADP and the underlying burst to formulate a simplified model of this phenomenon. We use this model to analyse the spike-adding on top of ADP. Moreover, the mathematical definition of ADP allows us to analyse numerically the onset of ADP and a spike, which we investigate further in Chapter 5.

In the next chapter we perform a slow-fast analysis of pituitary cell model, which is also written in Hodgkin-Huxley formalism. This study of a relatively simple three-dimensional model with one slow variable is a clear example, which demonstrates the classical ideas of GSPT. In the latter chapters we extend the slow-fast analysis to study a high-dimensional model of transient burst, which has two slow variables.



# **Chapter 3**

## **The role of large-conductance Calcium-activated K<sup>+</sup> (BK) channels in shaping bursting oscillations of a somatotroph cell model**

In this chapter we use classical ideas of GSPT to study a recently proposed somatotroph model that exhibits plateau bursting, a form of electrical activity that is typical for this cell type. We focus on how the large conductance (BK-type)  $\text{Ca}^{2+}$ -activated  $\text{K}^+$  current influences the oscillations and duration of the active phase. This three-dimensional model involves two different time scales, namely, it has two fast and one slow variables. Despite the relative simplicity of the model, a standard bifurcation analysis of equilibria and periodic orbits of the fast-time limit does not completely explain the behaviour of the model. In particular, the nullclines and velocities of the fast variables play an important role in shaping the bursting oscillations. We determine numerically how the fraction of open BK channels controls the amplitudes of the fast oscillations during the active phase. Furthermore, we show how manifolds of the fast subsystem are involved in the termination of the active phase.

### **3.1 Background**

Plateau bursting is a common pattern of electrical activity in hormone-secreting cells. Typical examples are the endocrine cells of the anterior pituitary gland, which are responsible for the secretion of hormones that, in turn, regulate a variety of other glands in the body (Stojilkovic et al., 2005; Van Goor et al., 2001b). All of the anterior pituitary cells exhibit  $\text{Ca}^{2+}$ -dependent electrical activity that can vary significantly between cell types, ranging from spiking to bursting with distinct duration of the depolarized plateaus (Van Goor et al., 2001b). We focus on

the behaviour of a particular type of pituitary cell, namely, the somatotroph cell which releases growth hormone. Experimental data (Stojilkovic et al., 2005; Tsaneva-Atanasova et al., 2007; Van Goor et al., 2001a,b) demonstrate that these cells fire plateau bursts of action potential (AP) associated with depolarization of the membrane potential ( $V_m$ ). In turn, these plateau bursts induce  $\text{Ca}^{2+}$ -signals with an amplitude that is sufficient to trigger hormonal secretion (Stojilkovic et al., 2005; Van Goor et al., 2001b). Clearly, a deeper insight into the mechanisms that govern the generation and duration of bursts of AP and concurrent  $\text{Ca}^{2+}$  signals is an important step toward a better understanding of secretory responses.

In order to address these questions we study the somatotroph cell model introduced by Tsaneva-Atanasova et al. in (Tsaneva-Atanasova et al., 2007). This model is based on the classic Hodgkin-Huxley formalism (Hodgkin and Huxley, 1952) and, therefore, incorporates the main biophysical determinants of the behaviour of somatotrophs. Previous theoretical studies have focused on investigations of the effect of various currents on the electrical activity in pituitary somatotrophs (Tsaneva-Atanasova et al., 2007) as well as phase resetting (Stern et al., 2008). Here, we concentrate on the underlying dynamics of plateau bursting. Therefore, it suffices to study a simplified three-dimensional version of the model, which also allows for direct visualization of the bursting behaviour. According to some bursting classifications (Izhikevich, 2000), the model in (Tsaneva-Atanasova et al., 2007) is an example of fold/subHopf bursting, also termed pseudo-plateau bursting (Stern et al., 2008). Interestingly, compared with previously published models of fold/subHopf bursters (LeBeau et al., 1998; Stern et al., 2008; Tabak et al., 2007; Toporikova et al., 2008), our model is subtly different, because it features very small plateau oscillations. Moreover, its active phase ends rather abruptly in a way that appears to be unrelated to the underlying bifurcation structure of the fast subsystem.

The results in (Tsaneva-Atanasova et al., 2007) suggest that the BK channels of the somatotroph cell play a key role in the initiation and the duration of plateau bursting. Modelling studies of other pituitary cell types have also shown that the magnitude of the BK current modulates the duration of plateau bursting (Tabak et al., 2007; Toporikova et al., 2008; Van Goor et al., 2001a). Since BK channels are present in many cell types and influence a variety of cellular functions by controlling  $\text{Ca}^{2+}$ -influx (Fakler and Adelman, 2008; Stojilkovic et al., 2005; Van Goor et al., 2001b), it is essential to explore their role in shaping the bursting oscillations.

## 3.2 The model

The model that we analyse in this chapter is a reduced version of the model presented in (Tsaneva-Atanasova et al., 2007) and consists of three ordinary differential equations that describe the rates of change of the membrane potential  $V_m$ , the delayed-rectifier activation gating variable  $n_{dr}$  that governs the fraction of open  $K^+$ -channels, and the intracellular concentration

$[Ca^{2+}]_i$  denoted by  $c$ . Here, we neglect the dynamics of the  $Ca^{2+}$  concentration in the endoplasmic reticulum and assume that it is constant at  $Ca_{ER} = 167\mu M$ ; namely, during plateau bursting in the full model  $[Ca^{2+}]_{ER}$  oscillates with very small amplitude around an average value of about  $167\mu M$  (Tsaneva-Atanasova et al., 2007). Hence, this is a reasonable assumption that allows for a dimension reduction. The simplified equations are as follows:

$$\frac{dV_m}{dt} = -\frac{1}{C_m} I_{ionic}(V_m, n_{dr}, c), \quad (3.1)$$

$$\frac{dn_{dr}}{dt} = \frac{n_{dr\infty}(V_m) - n_{dr}}{\tau_{n_{dr}}}, \quad (3.2)$$

$$\begin{aligned} \frac{dc}{dt} = & f\beta(-\alpha(I_{CaL}(V_m) + I_{CaT}(V_m)) - J_{PMCA}(c)) \\ & + \frac{1}{v_{cell}}(p_{ER}(Ca_{ER}(V_m) - c) - J_{SERCA}(c)). \end{aligned} \quad (3.3)$$

Model details as well as the values of the parameters used can be found in Appendix A.

System (3.1)–(3.3) is an example of slow-fast system; the variables  $V_m$  and  $n_{dr}$  change on a considerably faster time scale than  $c$ . A standard approach to analyse such systems is to consider the singular limit where the slow variable  $c$  is assumed to be constant (Fenichel, 1971; Rinzel, 1985). In this limit, Equations (3.1) and (3.2) represent the so-called fast subsystem, which describes the dynamics of the two variables  $V_m$  and  $n_{dr}$ , and the slow variable  $c$  is treated as a parameter.

### 3.3 Analysis of the model using the fast subsystem

Both experimental and theoretical results support the claim that BK channels have a large influence on the generation and duration of the active phase of plateau bursting in pituitary cells (Tsaneva-Atanasova et al., 2007; Van Goor et al., 2001a). Blocking of the BK-channels results in reduction of the BK-type  $Ca^{2+}$ -activated  $K^+$  current; see the Appendix. In our model the fraction of blocked BK channels is expressed by the value of the parameter  $b_{BK}$ . We consider both  $b_{BK} = 0$  and  $b_{BK} = 0.15$ , that is, the model without any BK channels blocked and with 15% of the open BK channels blocked.

The bursting behaviour of the model with  $b_{BK} = 0$  is shown in Figure 3.1. Panel (a) shows a time series of both  $V_m$  (blue) and  $c$  (red) that illustrates pseudo-plateau-bursting oscillations in  $V_m$  characterized by an active (bursting) and a silent phase. During the silent phase  $V_m$  slowly rises until it reaches a threshold level, which triggers the firing of an action potential (AP). The bursting activity results in an increase of  $c$ , because during the active phase there is  $Ca^{2+}$  influx through voltage-gated calcium channels. As  $c$  reaches a certain concentration (for  $b_{BK} = 0$  it is  $c \approx 1 \mu M$ ) the active phase ends. In the model, this end is caused by

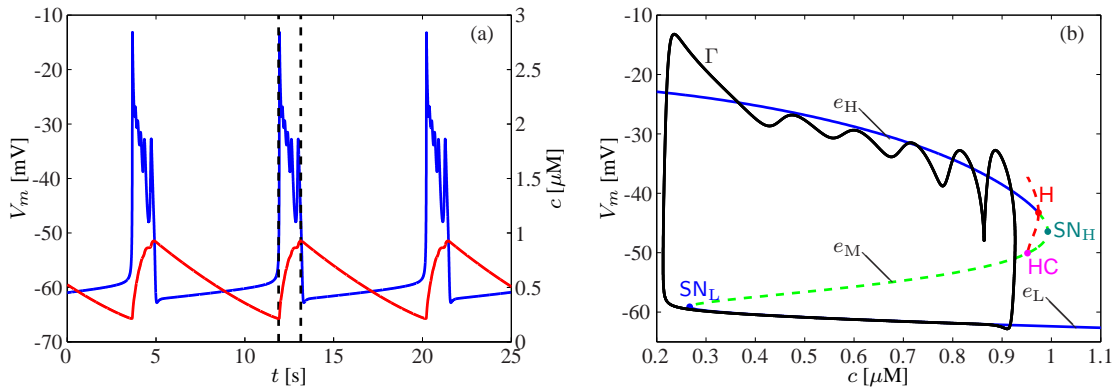


**Figure 3.1.** Bursting oscillations in system (3.1)–(3.3) with  $b_{\text{BK}} = 0$ . Panel (a) shows the periodic dynamics of  $V_m$  (blue) and  $c$  (red) versus time. One active phase is marked by black dashed lines. Panel (b) shows this same periodic orbit  $\Gamma$  (black) overlaid on the bifurcation diagram of the fast subsystem in the  $(c, V_m)$ -plane. The solid blue curves are branches of stable equilibria; the dashed green line consists of saddle equilibria; dashed red lines show the maxima and minima of the family of unstable periodic orbits that arises from the Hopf bifurcation point labeled  $H$ ; this family ends in a homoclinic bifurcation marked  $HC$ ; labels  $SN_L$  and  $SN_H$  indicate saddle-node bifurcations.

the activation of BK channels located further away from the voltage-gated calcium channels ( $\text{BK}_{\text{FAR}}$ ; see the Appendix) that repolarise the membrane potential (Tsaneva-Atanasova et al., 2007) and in this way control the level of  $[\text{Ca}^{2+}]_i$ . The maximal rise of  $\text{Ca}^{2+}$  is determined by the number of active BK channels (Fakler and Adelman, 2008; Tsaneva-Atanasova et al., 2007). Note that the duration of the active phase, which in Figure 3.1(a) is marked by black dashed lines, is significantly shorter than the duration of the silent phase. Hence, the rise in  $c$  is noticeably faster than its decay.

The pseudo-plateau-bursting oscillations in panel (a) correspond to a globally attracting periodic orbit of system (3.1)–(3.3). Figure 3.1(b) shows this periodic orbit, in projection onto the  $(c, V_m)$ -plane, as the black closed curve  $\Gamma$  superimposed on the bifurcation diagram of the fast subsystem (3.1)–(3.2). The bifurcation diagram of the fast subsystem (3.1)–(3.2) is formed by a Z-shaped branch of equilibria and a family of unstable periodic orbits. The top part of the Z-shaped branch (solid blue curve) is a family  $e_H$  of stable foci that loses stability at a subcritical Hopf bifurcation marked  $H$ ; this top part ends at a saddle-node bifurcation labelled  $SN_H$ . The bottom part of the Z-shaped branch is a family  $e_L$  of stable nodes that also ends at a saddle-node bifurcation, which is labelled  $SN_L$ ; the middle branch (dashed green line) in between the two saddle-node bifurcations is a family  $e_M$  of saddle equilibria. The family of unstable periodic orbits that emanates from the subcritical Hopf bifurcation terminates in a homoclinic bifurcation at a saddle equilibrium on  $e_M$  (labelled  $HC$ ). In relation to the full system (3.1)–(3.3), the branch  $e_H$  corresponds to the active phase and  $e_L$  to the silent phase.

The bifurcation diagram of the fast subsystem (3.1)–(3.2) is of fold/subHopf type (Izhike-

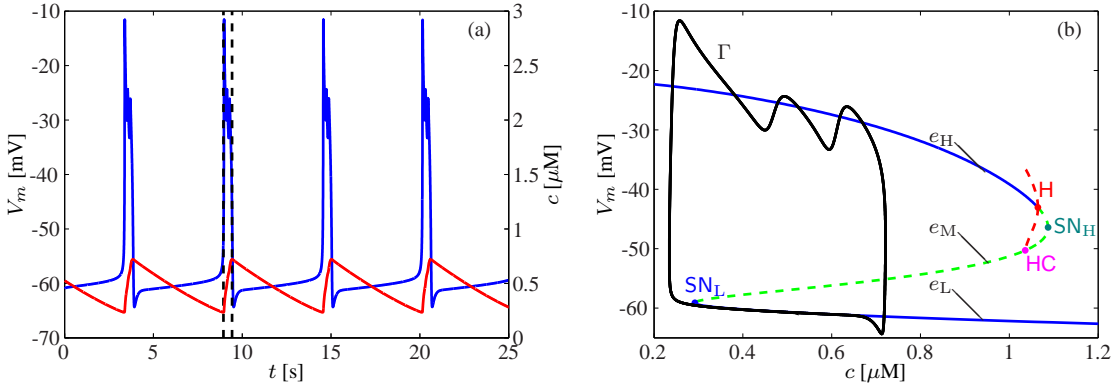


**Figure 3.2.** Bursting oscillations in system (3.1)–(3.3) with  $b_{BK} = 0.15$ . Panel (a) shows the periodic dynamics of  $V_m$  (blue) and  $c$  (red) versus time. One active phase is marked by black dashed lines. Panel (b) shows this same periodic orbit  $\Gamma$  (black) overlaid on the bifurcation diagram of the fast subsystem in the  $(c, V_m)$ -plane. The solid blue curves are branches of stable equilibria; the dashed green line consists of saddle equilibria; dashed red lines show the maxima and minima of the family of unstable periodic orbits that arises from the Hopf bifurcation point labelled  $H$ ; this family ends in a homoclinic bifurcation marked  $HC$ ; labels  $SN_L$  and  $SN_H$  indicate saddle-node bifurcations.

vich, 2000) and it is used to explain the behaviour of the full system (3.1)–(3.3) as follows (Fenichel, 1971; Rinzel, 1985). The silent phase of  $\Gamma$  occurs along the stable branch  $e_L$ . Since  $V_m$  is low, there is no influx of calcium and  $c$  decreases due to efflux. Hence, the phase point tracing  $\Gamma$  approximately follows  $e_L$  until it reaches  $SN_L$ . The decrease of calcium is accompanied by a gradual increase in the membrane potential, which leads to depolarization that is necessary for the activation of voltage-gated  $\text{Ca}^{2+}$ -channels. Indeed, the bifurcation diagram of the fast subsystem predicts the thresholds of  $V_m$  and  $c$  that mediate the transition from the silent to the active phase. As soon as  $V_m$  increases beyond the critical value at  $SN_L$ , the active phase begins, which is characterized by a rapid increase of  $V_m$  as the phase point of  $\Gamma$  moves up to the only remaining attractor on the branch  $e_H$ . The rapid change leads to an overshoot followed by several weaker oscillations along  $e_H$ . Since  $V_m$  is high along  $e_H$ , the voltage-gated  $\text{Ca}^{2+}$ -channels are open and  $[\text{Ca}^{2+}]_i$  starts to increase. Dynamically this means that  $\Gamma$  crosses the  $c$ -nullcline and, thus, changes its direction of motion.

Continuing the argument, one expects that the active phase ends at the moment when  $e_H$  loses stability, that is, at the Hopf bifurcation  $H$ , or perhaps at the homoclinic bifurcation  $HC$ . However, in contrast to classical plateau-bursting (square-wave or fold/homoclinic) oscillators (Bertram et al., 1995; Izhikevich, 2000; Keener and Sneyd, 2009; Shilnikov and Kolments, 2008) and pseudo-plateau (fold/subHopf) bursters (LeBeau et al., 1998; Stern et al., 2008; Tabak et al., 2007; Toporikova et al., 2008), the oscillations take place away from the family of periodic orbits. Hence, the Hopf and homoclinic bifurcations do not seem to play a role at all in the termination of the active phase of  $\Gamma$ . This same surprising behaviour can also be

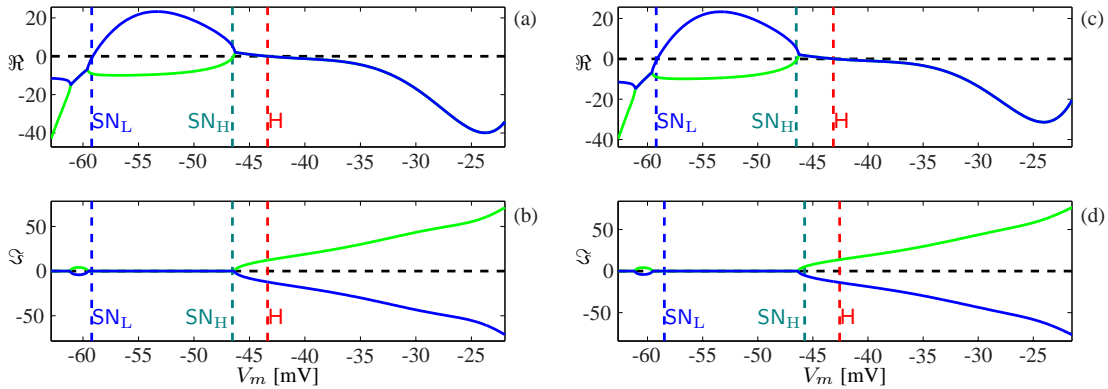


**Figure 3.3.** Eigenvalues of the fast subsystem with  $b_{BK} = 0$  (left column) and  $b_{BK} = 0.15$  (right column) as a function of  $V_m$  along the Z-shaped branch of equilibria  $e_L$ ,  $e_M$  and  $e_H$ ; panels (a) and (c) show the real parts and panels (b) and (d) the imaginary parts of the eigenvalues; the dotted vertical lines mark the bifurcation points  $SN_L$ ,  $SN_H$  and  $H$ , respectively.

observed for  $b_{BK} = 0.15$  as is shown in Figure 3.2. Here, the active phase consists of fewer oscillations, but with larger amplitude. Setting  $b_{BK} = 0.15$  reduces the magnitude of the BK current that is repolarising in our model, which results in an increase of the rate of change of  $V_m$ ; see Equation (3.1). As with  $b_{BK} = 0$ , the active phase ends long before the Hopf or homoclinic bifurcations. Note that the active phase, labelled by dashed lines in panel (a), is even shorter than for  $b_{BK} = 0$  and ends at a smaller concentration of  $\text{Ca}^{2+}$ , which only reaches the value of  $c \approx 0.7 \mu\text{M}$ . Another major difference between the two cases is the manner in which  $\Gamma$  oscillates during the active phase. For  $b_{BK} = 0$  the oscillations lie mostly below the branch  $e_H$ , while for  $b_{BK} = 0.15$  the oscillations are always around  $e_H$ .

The fact that  $\Gamma$  oscillates at all during the active phase requires that the slow variable  $c$  changes faster than the speed at which  $\Gamma$  is attracted to  $e_H$ . In order to establish the rate of convergence, we compute the eigenvalues of the fast subsystem (3.1)–(3.2) for each value of  $V_m$  along the Z-shaped branch of equilibria. Figure 3.3 shows the real (top row) and imaginary parts (bottom row) of the eigenvalues for the cases  $b_{BK} = 0$  and  $b_{BK} = 0.15$  in the left and right columns, respectively. Since the eigenvalues of  $e_L$  are mostly real with rather large negative real parts, there are no oscillations in this region and  $\Gamma$  is sliding along the branch until it reaches  $SN_L$ . Approximately at  $SN_L$  the orbit  $\Gamma$  jumps to  $e_H$  and enters the active phase. The family  $e_H$  are stable foci and the eigenvalues along this branch are complex conjugate with negative real parts. The transition of  $\Gamma$  from  $e_L$  to  $e_H$  is marked by a large overshoot at the beginning of the active phase determined by the magnitude of the eigenvalues at this  $c$  value. Figure 3.3 shows that the real parts of the eigenvalues along  $e_H$  are smaller for  $b_{BK} = 0.15$ , while the imaginary parts are the same as for  $b_{BK} = 0$ . Hence, the rate of convergence is weaker for  $b_{BK} = 0.15$ , which causes the difference in amplitudes of the oscillations during the active phase.

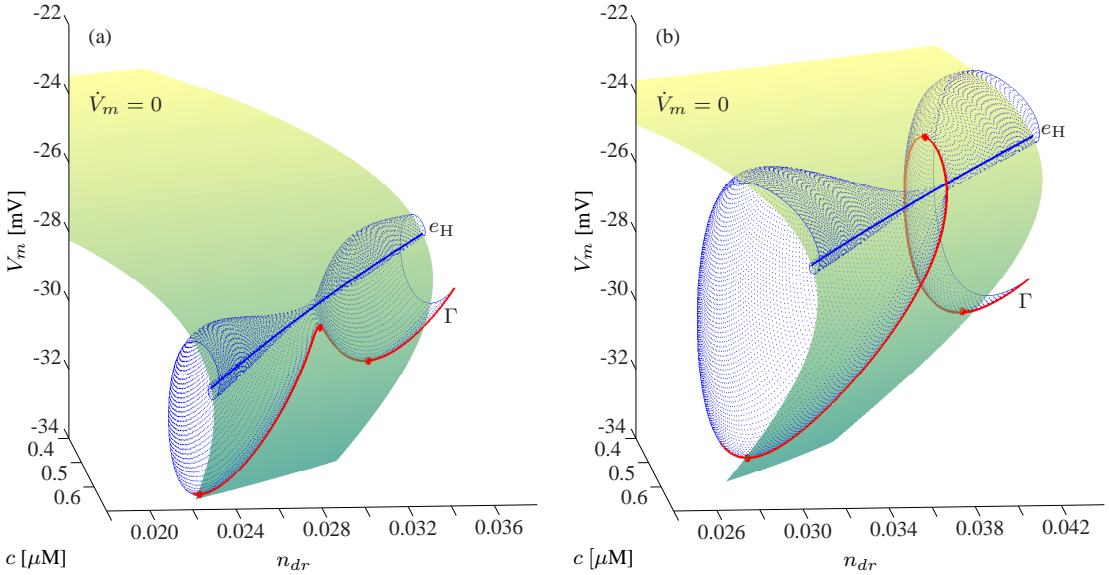


**Figure 3.4.** Three-dimensional view of one oscillation of  $\Gamma$  during the active phase for  $b_{BK} = 0$  (a) and  $b_{BK} = 0.15$  (b). The two panels show how  $\Gamma$  (red) interacts with the  $V_m$ -nullcline surface (green to yellow gradient). The blue cloud of points are trajectories of the frozen system starting on  $\Gamma$  for different values of  $c$ ; all these trajectories converge to the family  $e_H$  (blue curve) on the  $V_m$ -nullcline.

### 3.4 Oscillations during the active phase

Unfortunately, the analysis of the fast subsystem does not explain why the peaks of the plateau oscillations are below  $e_H$  for  $b_{BK} = 0$ , as illustrated in Figure 3.1(b). The oscillations for  $b_{BK} = 0.15$  are clearly around  $e_H$ , which is more in accordance with the theory (Izhikevich, 2000); see Figure 3.2(b). In fact, the theory does not make any statements about this difference in oscillations, but they seem counterintuitive nonetheless. Let us study the nature of the oscillations in more detail by considering the  $V_m$ -nullcline, which separates the regions of increasing and decreasing  $V_m$ . We focus on the part of the active phase after the first overshoot.

Figure 3.4 shows three-dimensional views of one oscillation of  $\Gamma$  (red curve) during the active phase past the overshoot. Panel (a) shows an oscillation for  $b_{BK} = 0$  in the range  $c \in [0.519, 0.679] \mu\text{M}$  and panel (b) shows an oscillation for  $b_{BK} = 0.15$  in the range  $c \in [0.465, 0.669] \mu\text{M}$ . The  $V_m$ -nullcline is a surface in  $(V_m, n_{dr}, c)$ -space, shown with a green to yellow gradient, and there are three intersection points with this part of  $\Gamma$ , indicated by red dots. Note that  $\Gamma$  has a local maximum or minim in  $V_m$  precisely at these intersection points. The (blue) point cloud is formed by trajectories of the fast subsystem (3.1)–(3.2), generated from initial conditions on  $\Gamma$ . As expected, each trajectory converges to the branch  $e_H$  of stable foci (blue curve). Figure 3.4 reveals that the oscillatory nature of  $\Gamma$  is essentially the same, except that the second crossing with the  $V_m$ -nullcline for  $b_{BK} = 0$  in panel (a) happens below  $e_H$ , while for  $b_{BK} = 0.15$  in panel (b) the second crossing takes place above

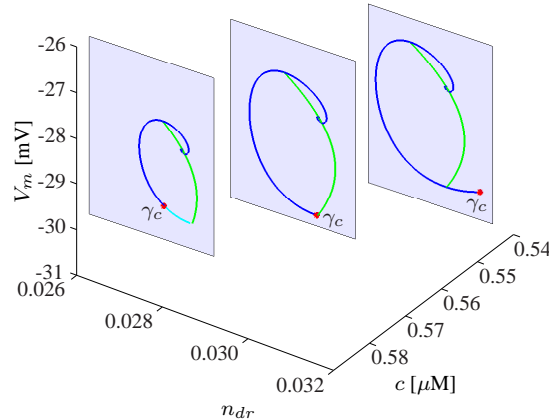


**Figure 3.5.** Behaviour of trajectories of the fast subsystem with  $b_{BK} = 0$  starting at initial values  $\gamma_c$  (red dots) along the active phase of  $\Gamma$  for  $c = 0.541 \mu\text{M}$ ,  $c = 0.559 \mu\text{M}$  and  $c = 0.578 \mu\text{M}$ , where  $\gamma_c$  lies to the right of, precisely on, and to the left of the  $V_m$ -nullcline (green), respectively.

$e_H$ . More precisely, the behaviour of  $\Gamma$  is entirely in line with the theory. Let us illustrate this further by considering three cross-sections in the  $(n_{dr}, V_m)$ -plane of the phase space shown in Figure 3.4(a) for  $b_{BK} = 0$ , namely, at  $c = 0.541 \mu\text{M}$ ,  $c = 0.559 \mu\text{M}$  and  $c = 0.578 \mu\text{M}$ ; see Figure 3.5. The trajectories of the fast subsystem generated from initial conditions  $\gamma_c$  on  $\Gamma$  (red dots) are drawn as solid (blue) curves and the cross-sections illustrate the different behaviour depending on the position of the initial condition relative to the  $V_m$ -nullcline (green). For  $c = 0.541 \mu\text{M}$ , the initial condition lies on the right-hand side of the  $V_m$ -nullcline and, at first,  $V_m$  decreases. Hence the trajectory of the fast subsystem appears to move away from the attractor. For  $c = 0.578 \mu\text{M}$  the initial condition lies on the left-hand side of the  $V_m$ -nullcline and  $V_m$  starts to rise immediately. The cross-section at  $c = 0.559 \mu\text{M}$  illustrates the transition between these two cases, where the trajectory of the fast subsystem starts exactly on the  $V_m$ -nullcline. Since  $\Gamma$  has a maximum or minimum precisely at these transition points, the change in the direction of motion satisfies the theory for the fast subsystem, as well as for  $\Gamma$ .

The fact that the oscillations of  $\Gamma$  during the active phase for  $b_{BK} = 0.15$  are able to reach the upper part of the  $V_m$ -nullcline surface in Figure 3.4(b) means that, in contrast to the case for  $b_{BK} = 0$ , the oscillations reach the  $n_{dr}$ -nullcline. We illustrate this in Figure 3.6(a) by plotting the entire active phase past the first overshoot in  $(\dot{V}_m, \dot{n}_{dr}, c)$ -space, that is, in terms of the velocities of the fast variables  $V_m$  and  $n_{dr}$ . The active phase for  $b_{BK} = 0$  (red curve) lasts five oscillations, while the active phase for  $b_{BK} = 0.15$  (cyan curve) is much shorter and lasts only two oscillations after the first overshoot. The horizontal (green) plane at  $\dot{V}_m = 0$  is the  $V_m$ -nullcline. Note that each oscillation of the active phase both for  $b_{BK} = 0$  and  $b_{BK} = 0.15$  crosses the  $V_m$ -nullcline twice. This can most easily be seen in Figure 3.6(b), where we plot the projection onto the  $(c, \dot{V}_m)$ -plane with the  $V_m$ -nullcline shown as a dashed (green) line. The vertical (blue) plane at  $\dot{n}_{dr} = 0$  is the  $n_{dr}$ -nullcline. The active phase for  $b_{BK} = 0.15$

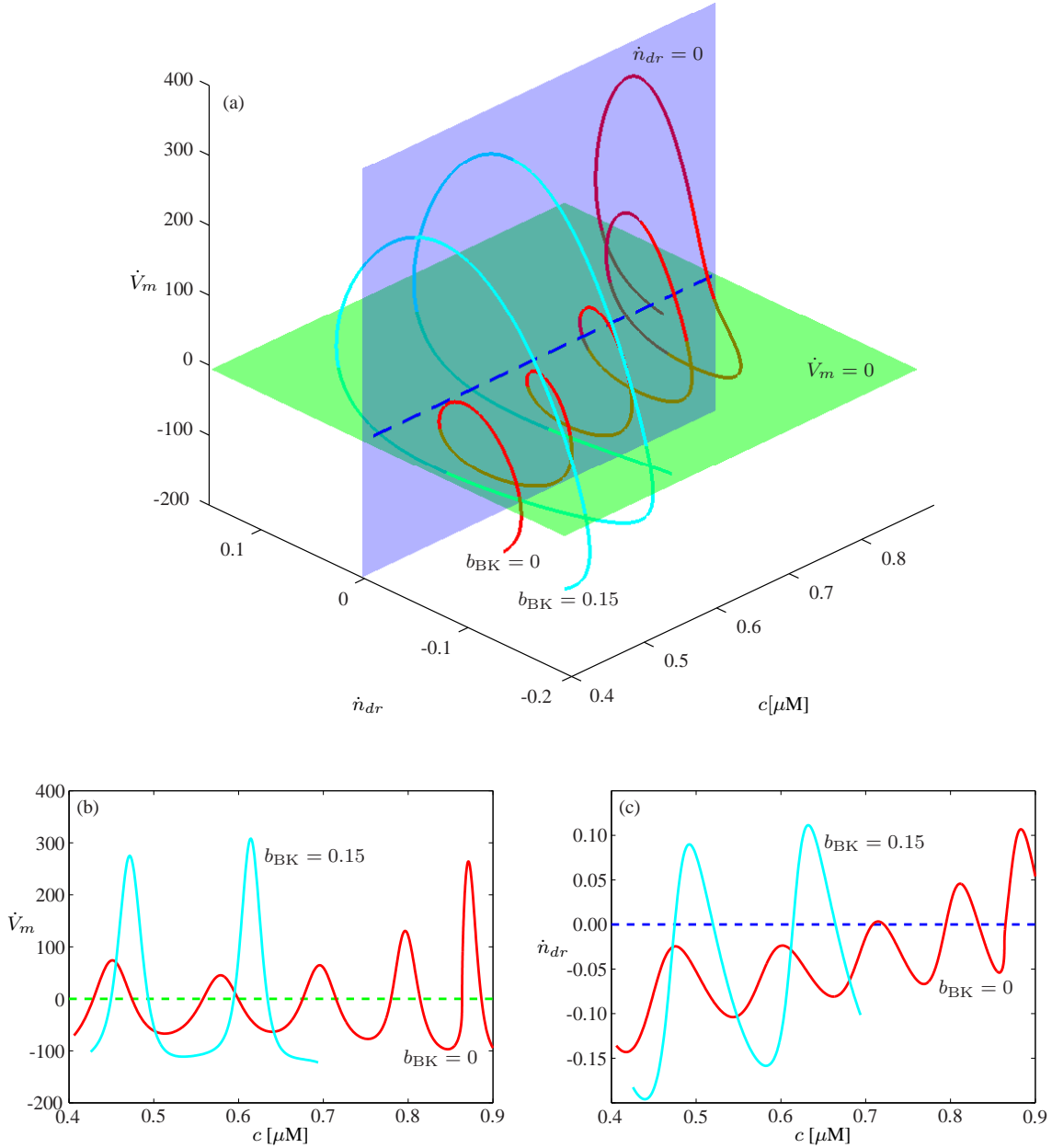
crosses the  $n_{dr}$ -nullcline also twice during each revolution. However, for  $b_{BK} = 0$  the first two oscillations do not reach the  $n_{dr}$ -nullcline, as is most clearly shown in the projection onto the  $(c, \dot{n}_{dr})$ -plane in Figure 3.6(c). In fact, the third oscillation for  $b_{BK} = 0$  only just crosses the  $n_{dr}$ -nullcline; compare also with Figure 3.1(b) where the third oscillation after the overshoot barely goes around the branch  $e_H$ .

Figure 3.6 indicates that the  $n_{dr}$ -nullcline plays an essential role in shaping the oscillations during the active phase. Surprisingly, the  $n_{dr}$ -nullcline does not depend on  $b_{BK}$  or  $c$  at all. That is, the level of  $[Ca^{2+}]_i$ , which is regulated by the value of  $b_{BK}$ , does not influence the position of the  $n_{dr}$ -nullcline. Hence, the transition happens solely through the variation of  $\Gamma$ . Since the modulation of BK channel activity significantly affects the shape and duration of the active phase it is of interest to obtain an estimate of the critical  $b_{BK}$ -value for which the active phase changes from oscillating below to oscillation around  $e_H$ . We define the moment of this transition as the  $b_{BK}$ -value for which the first oscillation of  $\Gamma$  after the initial overshoot is tangent to the  $n_{dr}$ -nullcline. This means that  $\dot{n}_{dr} = 0$  at the peak of the second oscillation, where  $\dot{V}_m = 0$  for the third time. Note that the condition  $\dot{n}_{dr} = 0$  as well as  $\dot{V}_m = 0$  means that  $\Gamma$  will be tangent to  $e_H$ . We track the points along the active phase of  $\Gamma$  where  $\dot{V}_m = 0$  numerically and continue the third such point in the parameter  $b_{BK}$  while monitoring the value of  $\dot{n}_{dr}$ ; the result is shown in Figure 3.7. If  $\dot{n}_{dr} < 0$  then the first oscillation of  $\Gamma$  after the overshoot will be below  $e_H$ . If  $\dot{n}_{dr} > 0$  then the second peak already lies above  $e_H$ , so that most likely all oscillations of the active phase are around  $e_H$ . We determined numerically that the transition happens approximately at  $b_{BK} = 0.07$ . The time series of  $\Gamma$  and the associated bifurcation diagram of the fast subsystem for this critical value  $b_{BK} = 0.07$  are shown in Figure 3.8; compare also with Figures 3.1 and 3.2.

### 3.5 The end of the active phase

Modulating the BK current not only affects the position of the oscillations in the active phase relative to the equilibrium branch  $e_H$ . Figures 3.1, 3.2, and 3.8 show that increasing  $b_{BK}$  dramatically alters the duration of the active phase. The active phase contains six oscillations for  $b_{BK} = 0$  and ends relatively close to the homoclinic bifurcation HC, but for  $b_{BK} = 0.07$  there are five oscillations, and for  $b_{BK} = 0.15$  only three oscillations remain, while the end of the active phase moves increasingly further away to the left of HC. Note that the variation of  $b_{BK}$  has almost no effect on the bifurcation diagram of the fast subsystem, so that this cannot be the mechanism behind the termination of the active phase.

Since we have coexisting attractors for the range of  $c$  that corresponds to the active phase, the end of the active phase must be explained by the fact that  $\Gamma$  leaves the basin of attraction of  $e_H$ , thereby entering the basin of attraction of  $e_L$ . The projection onto the  $(c, V_m)$ -plane of



**Figure 3.6.** The active phase of  $\Gamma$  past the first overshoot for  $b_{BK} = 0$  (red curve) and  $b_{BK} = 0.15$  (cyan curve) plotted in  $(\dot{V}_m, \dot{n}_{dr}, c)$ -space (a) along with projections onto the  $(c, \dot{V}_m)$ - and  $(c, \dot{n}_{dr})$ -planes in panels (b) and (c), respectively. The nullclines  $\dot{V}_m = 0$  (green horizontal plane) and  $\dot{n}_{dr} = 0$  (blue vertical plane) in panel (a) project to the dashed lines in panels (b) and (c), respectively.

the bifurcation diagram of the fast subsystem appears to indicate that the branch  $e_M$  of saddle equilibria separates the two basins of attraction. However, in the full  $(V_m, n_{dr}, c)$ -space the separatrix is formed by the family of one-dimensional stable manifolds of the saddle points

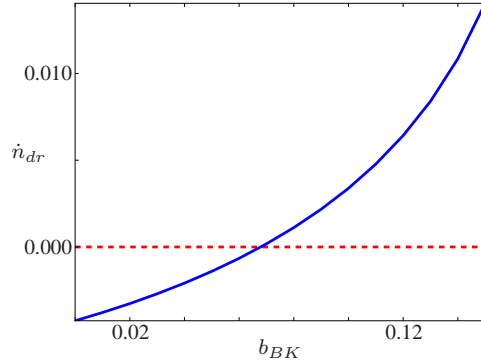


**Figure 3.7.** The value of  $\dot{n}_{dr}$  at the peak of the second oscillation in the active phase of  $\Gamma$  as a function of  $b_{BK} \in [0, 0.15]$ . The crossing at  $\dot{n}_{dr} = 0$  marks the transition from oscillations below  $e_H$  to oscillations around  $e_H$  in system (3.1)–(3.3).

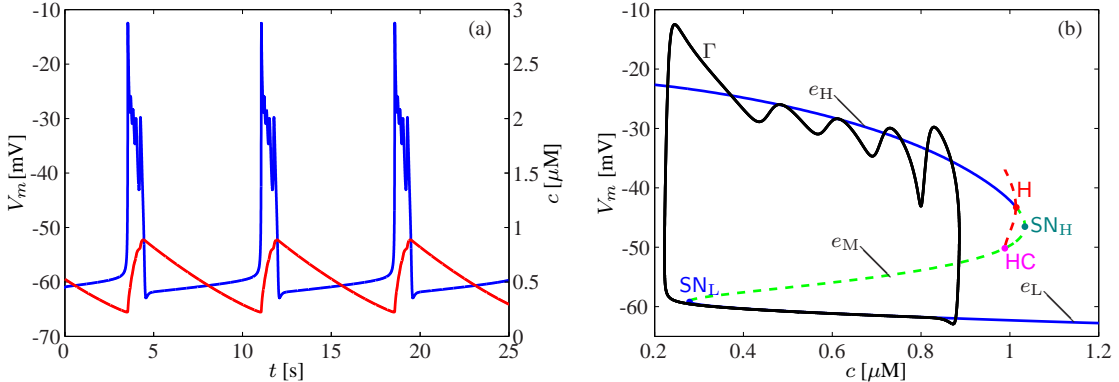


**Figure 3.8.** Bursting oscillations in system (3.1)–(3.3) with  $b_{BK} = 0.07$ . Panel (a) shows the periodic dynamics of  $V_m$  (blue) and  $c$  (red) versus time. Panel (b) shows this same periodic orbit  $\Gamma$  (black) overlaid on the bifurcation diagram of the fast subsystem in the  $(c, V_m)$ -plane. The solid blue curves are branches of stable equilibria; the dashed green line consists of saddle equilibria; dashed red lines show the maxima and minima of the family of unstable periodic orbits that arises from the Hopf bifurcation point labelled H; this family ends in a homoclinic bifurcation marked HC; labels  $SN_L$  and  $SN_H$  indicate saddle-node bifurcations.

on  $e_M$ . This family, denoted  $W^s(e_M)$ , is a well-defined manifold for saddle points on  $e_M$  in between the saddle-node bifurcation  $SN_L$  and the homoclinic bifurcation  $HC$ ; note that the family of one-dimensional stable manifolds continues to exist for points on  $e_M$  past  $HC$ , but then the manifolds are no longer separating the basins of attraction.

We compute the family  $W^s(e_M)$  via continuation of a one-parameter family of two-point boundary value problems (Krauskopf and Osinga, 2007). The manifold  $W^s(e_M)$  is parametrized by  $c$  and the computation effectively generates a family of orbit segments that start at a point on the ( $c$ -dependent) stable eigenvector sufficiently close to the ( $c$ -dependent) saddle point on  $e_M$ ; we refer to (Krauskopf and Osinga, 2007; Krauskopf and Rieß, 2008) for details on the

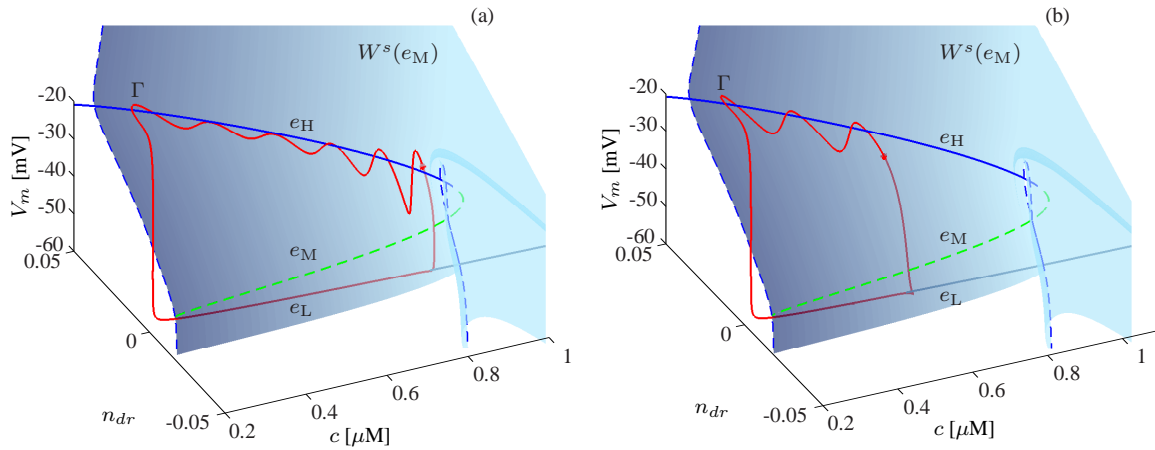


**Figure 3.9.** The  $c$ -dependent family  $W^s(e_M)$  of one-dimensional stable manifolds of the saddle points along  $e_M$  in between  $SN_L$  and  $HC$ . Panel (a) shows the manifold for  $b_{BK} = 0$  and panel (b) for  $b_{BK} = 0.15$  along with the family  $e_M$  of saddle equilibria (green dashed line). The manifold  $W^s(e_M)$  is shown as a blue gradient surface with two solid (blue) lines marking the bounding manifolds at  $SN_L$  and  $HC$ . The orbit  $\Gamma$  is depicted as a solid (red) curve.

precise boundary conditions. The branches starting along the eigendirection with positive  $V_m$  were computed up to arc length 60 and those with negative  $V_m$  up to arc length 10. Figure 3.9 shows  $W^s(e_M)$  as a blue gradient surface with the associated equilibria on  $e_M$  marked by a dashed (green) line. Panel (a) shows the manifold for  $b_{BK} = 0$  and panel (b) for  $b_{BK} = 0.15$ . In both cases the corresponding orbit  $\Gamma$  is shown as well (red curve).

The manifolds  $W^s(e_M)$  for  $b_{BK} = 0$  and  $b_{BK} = 0.15$  are quite similar. For low values of  $c$  the surface is relatively straightforward with each one-dimensional manifold having one side (the upper branch) extend toward  $-\infty$  and the other side extend toward  $+\infty$  for both  $V_m$  and  $n_{dr}$ . The first bounding manifold on this side is shown as a dashed (blue) curve and corresponds to the manifold at the moment of the saddle-node bifurcation ( $SN_L$ ). The manifolds vary smoothly with  $c$  and, in fact, they hardly change initially as  $c$  increases. The other side of  $W^s(e_M)$  is bounded by the homoclinic bifurcation, which is again shown as a dashed (blue) curve. Here, the one-dimensional stable manifold of the corresponding saddle equilibrium on  $e_M$  must have its upper branch fold over and connect back to this saddle equilibrium. Since the family of manifolds depends smoothly on  $c$ , one expects to see the folding happening slightly earlier, for slightly smaller values of  $c$ , so that the upper branch comes back below the corresponding saddle equilibrium and folds exponentially flat onto the lower branch, also extending to  $-\infty$  for both  $V_m$  and  $n_{dr}$ . The start of this process can be observed in Figure 3.9 as the darker shaded band running through the lighter side of  $W^s(e_M)$ , which is caused by the smaller steps taken in the continuation to capture the dramatic change of the one-dimensional manifolds here.

While the expected folding of the manifolds does take place before the homoclinic bifur-

cation, it happens only for a relatively small range of  $c$ -values and there is little difference between the manifolds for  $b_{BK} = 0$  and  $b_{BK} = 0.15$ . This means that  $b_{BK}$  has no noticeable influence on the shape of the basin of attraction of  $e_H$ . Hence, similarly to the case for oscillations below or around  $e_H$ , the parameter  $b_{BK}$  only influences the shape of the orbit  $\Gamma$  itself such that its position with respect to  $W^s(e_M)$  changes. Indeed,  $b_{BK}$  has the effect of increasing the amplitude of the oscillations of  $\Gamma$  during the active phase. This increase causes  $\Gamma$  to lie closer to  $W^s(e_M)$  so that it crosses  $W^s(e_M)$  for increasingly smaller values of  $c$ . As illustrated in Figure 3.9, as soon as  $\Gamma$  crosses  $W^s(e_M)$ , it drops down to  $e_L$  and the active phase ends.

Therefore, the behaviour of system (3.1)–(3.3) can be explained using the fast subsystem (3.1)–(3.2), but the bifurcation analysis must include the computation of the stable manifolds that bound the basins of attraction of  $e_H$  and  $e_L$  that represent the active and silent phases, respectively. As we already noted earlier, the fast subsystem is, however, not noticeably affected when a fraction of the BK channels is blocked. The parameter  $b_{BK}$  only influences the amplitude of  $\Gamma$ , which may be inferred from inspecting the contraction rates along the branch  $e_H$ , but is extremely subtle. An increase in amplitude causes  $\Gamma$  to oscillate closer to  $W^s(e_M)$  already for small values of  $c$ , which leads to the earlier termination of the active phase.

## 3.6 Conclusion

We performed a detailed analysis of a slow-fast single-compartment physiologically-based cell model of fold/subHopf type. We used a reduced version of a somatotroph cell model by Tsaneva-Atanasova et al. (Tsaneva-Atanasova et al., 2007) that includes modulation of the BK channels, controlled by the parameter  $b_{BK}$ . As previously reported in (Tsaneva-Atanasova et al., 2007; Van Goor et al., 2001a), blocking of the BK channels significantly influences the model behaviour. We considered the cases of no ( $b_{BK} = 0$ ) and 15% blocking ( $b_{BK} = 0.15$ ). In order to understand fully the behaviour of the bursting trajectories in our model we had to consider dynamical systems techniques other than the classical bifurcation analysis of the corresponding fast subsystem, where one considers the singular limit of stationary slow flow. Through a detailed analysis of the relative position of the nullclines, we explained the seemingly counterintuitive behaviour of the plateau bursting taking place below the branch of attracting equilibria of the fast subsystem that corresponds to the active phase. Furthermore, we used continuation to compute the basin boundary of this branch of attracting equilibria of the fast subsystem as a family of one-dimensional stable manifolds of saddle equilibria. Our computation showed that this surface marks the end of the active phase.

In the next chapter we extend the slow-fast analysis from one to two slow variables and study the transient spike-adding mechanism originating from ADP in pyramidal neurons. We compute the critical manifold parametrised by two slow variables, which consists of equilibria

of the fast subsystem, and it is embedded in a five-dimensional space of the full system. Our analysis shows that slow flow on the critical manifold plays an important role in spike adding in transient burst. Despite the fact, that stable manifold exist in this system and also shapes the behaviour of the model, it is very hard to calculate for such a high-dimensional system. Hence, we do not use the computation of the stable manifold in the analysis presented in the next chapter.

# Chapter 4

## Dynamical systems analysis of spike-adding mechanisms in transient bursts

In this chapter we analyse the spike-adding mechanism in a transient burst, where the burst takes place due to a brief perturbation and a periodic attractor of the full system does not exist. We use GSPT and numerical continuation methods to study such transient behaviour in the model of hippocampal pyramidal neurons from Chapter 2.

As for periodic bursting, a spike-adding transition occurs over a very small parameter interval (Guckenheimer and Kuehn, 2009; Lee and Terman, 1999; Terman, 1992). Within this very small parameter interval, we find an even smaller parameter interval during which the canard-like orbit segment includes a fast transition from a saddle-unstable to *another saddle-unstable* slow manifold. This phenomenon is similar to so-called fold-initiated canards that have been observed for periodic orbits (Guckenheimer and Hoffman, 2000). To understand this behaviour we study the associated slow flow on the critical manifold and identify the effect of folds and folded singularities on the behaviour of the orbit segment.

Our study concerns the analysis of a spike-adding mechanism where the full system has a unique stable equilibrium that does not undergo any bifurcations. We find that for different values of model parameters, the system can have additional unstable equilibria that alter the nature of the spike-adding mechanism. More precisely, the appearance of two saddle equilibria on the critical manifold suppresses the fold-initiated transition between unstable sheets and changes the behaviour of the orbit segment. We analyse the slow flow on the critical manifold to explain this phenomenon.

### 4.1 The model

We apply our analysis of transient bursts to pyramidal neuron cells from the CA1 and CA3 regions of the hippocampus. Here, we study a reduced version of the model of those neurons

presented in Chapter 2. The simplified model consists of four ionic currents, namely, fast and slow inward currents, denoted  $I_{FI}$  and  $I_{SI}$ , respectively, and fast and slow outward currents, denoted  $I_{FO}$  and  $I_{SO}$ , respectively. Inward currents are responsible for the depolarisation or increase of the membrane potential, whereas outward currents hyperpolarise or decrease the membrane potential and return the cell back to its resting state (a stable equilibrium) (Hodgkin and Huxley, 1952; Keener and Sneyd, 2009). The fast inward current  $I_{FI}$  represents the fastest class of spike-generating  $\text{Na}^+$ - and  $\text{Ca}^{2+}$ -currents. The rates of change of these currents are usually similar to that of the membrane potential. Therefore, we assume that the gating of  $I_{FI}$  is instantaneous (Golomb et al., 2006; Hodgkin and Huxley, 1952; Yue et al., 2005). The slow inward current  $I_{SI}$  mainly corresponds to the transient T-type  $\text{Ca}^{2+}$ -current (Blackmer et al., 2009; Jaffe et al., 1994; Yaari et al., 2007) and represents the low-voltage activated currents responsible for shaping the subthreshold behaviour of the model. The fast outward current  $I_{FO}$  represents high-voltage activated fast  $\text{K}^+$ -currents that we base on the delayed rectifier  $\text{K}^+$ -current (Golomb et al., 2006; Hodgkin and Huxley, 1952). Finally,  $I_{SO}$  represents muscarinic-sensitive  $\text{K}^+$ -current (Yaari et al., 2007; Yue and Yaari, 2004, 2006), which has an activation rate of the same order as that of  $I_{SI}$ .

We only consider the following variables as dynamic: the membrane potential  $V$ , the gating variables  $m_{SI}$ ,  $m_{FO}$  and  $m_{SO}$  that govern activation of the respective currents, and the gating variable for inactivation of  $I_{SI}$ , which we denote by  $h_{SI}$ . Hence, our reduced model is five dimensional and has the form

$$\frac{d\mathbf{u}}{dt} = \frac{d}{dt} \begin{pmatrix} V \\ m_{SI} \\ m_{FO} \\ m_{SO} \\ h_{SI} \end{pmatrix} = \mathbf{f}(\mathbf{u}, \lambda, I_{app}) := \begin{pmatrix} f_1(\mathbf{u}, \lambda, I_{app}) \\ f_2(\mathbf{u}, \lambda) \\ f_3(\mathbf{u}, \lambda) \\ f_4(\mathbf{u}, \lambda) \\ f_5(\mathbf{u}, \lambda) \end{pmatrix}. \quad (4.1)$$

Here,  $\mathbf{u} \in \mathbb{R}^5$  is the non-dimensionalised state vector and  $I_{app}$  is an applied current that stimulates (perturbs) the cell model when it is non-zero. We specifically indicate further parameter dependencies with the parameter vector  $\lambda \in \mathbb{R}^k$ , for some integer  $k > 0$ ; in this chapter we primarily focus on how the system depends on the maximal conductances of  $I_{SI}$  and  $I_{FO}$ ; these parameters are most likely to vary between neurons, due to different sizes and numbers of channels in different cells (even among the same types of neurons). The right-hand side of (4.1) has the specific form that is well known from Hodgkin-Huxley formalism: the dynamics of the

$C_m = 1.0 \mu\text{F}/\text{cm}^2$		
Inward currents:		
$g_{\text{FI}} = 2.0 \text{ mS}/\text{cm}^2$	$E_I = 80.0 \text{ mV}$	
$V_{m_{\text{FI}}} = -25.0 \text{ mV}$	$g_{\text{SI}} = 0.5 \text{ mS}/\text{cm}^2$	$V_{h_{\text{SI}}} = -56.0 \text{ mV}$
$k_{m_{\text{FI}}} = 5.0 \text{ mV}$	$V_{m_{\text{SI}}} = -54.0 \text{ mV}$	$k_{h_{\text{SI}}} = 8.5 \text{ mV}$
	$k_{m_{\text{SI}}} = 5.0 \text{ mV}$	$\tau_{h_{\text{SI}}} = 20.0 \text{ ms}$
	$\tau_{m_{\text{SI}}} = 3.0 \text{ ms}$	
Outward currents:		
$g_{\text{FO}} = 9.5 \text{ mS}/\text{cm}^2$	$E_O = -80.0 \text{ mV}$	
$V_{m_{\text{FO}}} = -6.0 \text{ mV}$	$g_{\text{SO}} = 1.2 \text{ mS}/\text{cm}^2$	$V_{m_{\text{SO}}} = -20.0 \text{ mV}$
$k_{m_{\text{FO}}} = 11.5 \text{ mV}$	$k_{m_{\text{SO}}} = 10.0 \text{ mV}$	
$\tau_{m_{\text{FO}}} = 1.0 \text{ ms}$	$\tau_{m_{\text{SO}}} = 75.0 \text{ ms}$	

**Table 4.1.** Parameter values for the simplified model (4.1) as defined in (4.2)–(4.4).

membrane potential is organised by the equations for the ionic currents, modelled as

$$\begin{aligned} C_m \frac{dV}{dt} &= -(I_{\text{FI}} + I_{\text{SI}} + I_{\text{FO}} + I_{\text{SO}}) + I_{\text{app}} \\ &= -(g_{\text{FI}} m_{\text{FI}}(V)(V - E_I) + g_{\text{SI}} m_{\text{SI}}^2 h_{\text{SI}}(V - E_I) \\ &\quad + g_{\text{FO}} m_{\text{FO}}(V - E_O) + g_{\text{SO}} m_{\text{SO}}(V - E_O)) + I_{\text{app}}, \end{aligned} \quad (4.2)$$

where  $C_m$  is the membrane capacitance. Here,  $g_x$  with  $x \in \{\text{FI}, \text{SI}, \text{FO}, \text{SO}\}$  are maximal conductances of the currents and  $E_I$  and  $E_O$  are Nerst potentials of the inward and outward currents, respectively. Note that  $I_{\text{FI}}$  only depends on  $V$ , that is,  $m_{\text{FI}} = m_{\text{FI}}(V)$  as defined in (4.4) below. The dynamics of the gating variables is modelled by

$$\frac{dx}{dt} = \frac{x_\infty(V) - x}{\tau_x}, \quad \text{where } x \in \{m_{\text{SI}}, m_{\text{FO}}, m_{\text{SO}}, h_{\text{SI}}\}; \quad (4.3)$$

the corresponding activation and inactivation steady-state functions  $x_\infty(V)$  of the respective currents, as well as  $m_{\text{FI}}(V)$ , are given in Boltzmann form as:

$$x_\infty(V) = \frac{1}{1 + \exp\left(-\frac{V - V_x}{k_x}\right)}. \quad (4.4)$$

Unless specified otherwise, the default values that we use for the parameters of this simplified model are summarised in Table 4.1.

Figure 4.1 illustrates three classes of the responses of the simplified model obtained by changing the maximal conductance  $g_{\text{SI}}$ . These correspond to cell responses, that are typically observed experimentally. During the simulations, the model is perturbed from its stable equilibrium by a short-current injection whose duration guarantees that the rapidly rising membrane

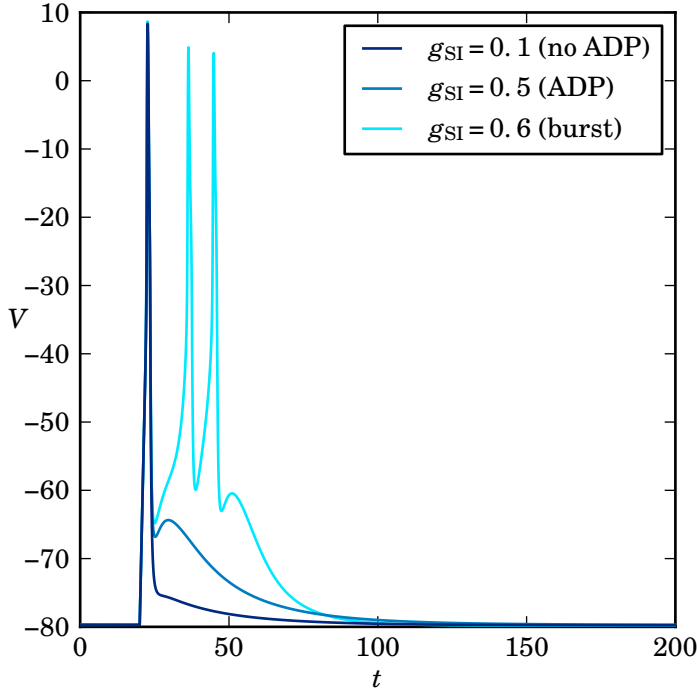


**Figure 4.1.** Responses of system (4.1) to a current injection of  $I_{\text{app}} = 20 \mu\text{A}/\text{cm}^2$  from  $t = 20$  to  $t = 23$ ; overlaid are the responses corresponding to different values of the maximal conductance  $g_{\text{SI}}$  (in  $\text{mS}/\text{cm}^2$ ) of the slow inward current, namely,  $g_{\text{SI}} = 0.1$ ,  $g_{\text{SI}} = 0.5$  and  $g_{\text{SI}} = 0.6$ , which are examples of responses with no ADP, with ADP and a (three-spike) burst with ADP, respectively.

potential will reach and cross its local maximum creating a fully developed spike; see (Brown and Randall, 2009; Golomb et al., 2006; Yue et al., 2005) for more details. Two of the three typical responses shown in Figure 4.1 exhibit a positive deflection of the membrane potential characterised by a ‘hump’ in the time trace of the membrane potential at the end of the burst; this is called after-depolarisation (ADP), which can exist, provided  $\tau_{m_{\text{FO}}} < \tau_{m_{\text{SI}}}$  as shown in Chapter 2. Only the first response (lower curve) is a spike without ADP. Note that the last trace, which corresponds to  $g_{\text{SI}} = 0.6$ , the highest value of  $g_{\text{SI}}$  in the example, has sufficiently strong  $I_{\text{SI}}$  to enable the membrane potential to cross the excitability threshold during the ADP, so that additional spikes are fired.

System (4.1) defined by equations (4.2)–(4.4) evolves on multiple time scales, because  $C_m/g_{\text{FO}}$  (as an approximation of the time scale for  $V$ ) and  $\tau_x$  with  $x \in \{m_{\text{SI}}, m_{\text{FO}}, m_{\text{SO}}, h_{\text{SI}}\}$  have different orders of magnitude. As indicated in Table 4.1,  $m_{\text{SO}}$  and  $h_{\text{SI}}$  are slow variables that vary on a time scale that is (roughly) 10 times slower than  $m_{\text{SI}}$  and  $m_{\text{FO}}$ , and 100 times slower than  $V$ . In particular, this means that our model is capable of firing an arbitrarily large number of spikes during the ADP. More precisely, an increase in  $g_{\text{SI}}$ , as in Figure 4.1 and

throughout this chapter, has the net effect that the slow variable  $h_{\text{SI}}$  becomes even slower, so that more spikes can be fired during the time it takes for  $h_{\text{SI}}$  to relax back to its equilibrium value. In this chapter we are not interested in the exact nature of this process, but we mention here that a large number of spikes will also be accompanied by a noticeable reduction in oscillation amplitudes, because the dynamics, as  $h_{\text{SI}}$  slows down, will more and more resemble the behaviour organised by slow passage through a Hopf bifurcation (Baer et al., 1989; Tsaneva-Atanasova et al., 2010). We focus on the process of spike adding and take advantage of the difference in time scales in Section 4.2, where it suffices to consider time-scale separation between the three fast variables  $V$ ,  $m_{\text{SI}}$  and  $m_{\text{FO}}$ , and two slow variables  $m_{\text{SO}}$  and  $h_{\text{SI}}$ .

The gating variables express the fractions of channels in a given state and naturally range over the interval  $[0, 1]$ . The natural range of the membrane potential  $V$  is bounded by the two Nernst potentials (Hodgkin and Huxley, 1952; Keener and Sneyd, 2009), i.e.,  $E_{\text{O}} \leq V \leq E_{\text{I}}$ , where  $E_{\text{O}} = -80.0$  mV and  $E_{\text{I}} = 80.0$  mV. It is beneficial for the numerical analysis if all variables vary over a similar range. Therefore, the computations are done using the scaled membrane potential  $V/k_v$ , where  $k_v = 100$  mV.

## 4.2 Identifying the spike-adding mechanism

Spike adding happens after a current injection, that is, in the regime where  $I_{\text{app}} = 0$ . Hence, any numerical investigation of the transient behaviour must take into account a discontinuous jump from  $I_{\text{app}} > 0$  to  $I_{\text{app}} = 0$  on the right-hand side of Equation (4.2). We view the orbit as a concatenation of two orbit segments that are the solution of a two boundary value problems and define appropriate boundary conditions to account for the discontinuity in  $I_{\text{app}}$ .

More precisely, we consider two successive orbit segments, denoted  $\mathbf{u}_{\text{ON}}$  and  $\mathbf{u}_{\text{OFF}}$ , during which current is injected ( $I_{\text{app}} > 0$ ) and during which it is not ( $I_{\text{app}} = 0$ ), respectively; the concatenation of the two orbit segments  $\mathbf{u}_{\text{ON}}$  and  $\mathbf{u}_{\text{OFF}}$  gives the orbit segment that characterises the solution of interest. An illustration of this idea is given in Figure 4.2, where  $\mathbf{u}_{\text{ON}}$  is the segment coloured red and  $\mathbf{u}_{\text{OFF}}$  the segment coloured blue. Both  $\mathbf{u}_{\text{ON}}$  and  $\mathbf{u}_{\text{OFF}}$  are solution segments of (4.1), but for different values of  $I_{\text{app}}$  and for different integration times  $T_{\text{ON}}$  and  $T_{\text{OFF}}$ , respectively. Using the set-up that is standard in AUTO (Doedel, 1981; Doedel and Oldeman, 2009), we formulate a boundary value problem using scaled equations, such that the total integration time for both segments is 1. That is,  $\mathbf{u}_{\text{ON}}$  and  $\mathbf{u}_{\text{OFF}}$  are solutions of

$$\mathbf{u}'_{\text{ON}}(t) = T_{\text{ON}} \mathbf{f}(\mathbf{u}_{\text{ON}}(t), \lambda, I_{\text{app}}), \quad (4.5)$$

$$\mathbf{u}'_{\text{OFF}}(t) = T_{\text{OFF}} \mathbf{f}(\mathbf{u}_{\text{OFF}}(t), \lambda, 0). \quad (4.6)$$

In order to obtain a unique solution pair  $\{\mathbf{u}_{\text{ON}}, \mathbf{u}_{\text{OFF}}\}$ , we must impose boundary conditions. The boundary conditions for (4.5) are determined by the fact that the current injection perturbs

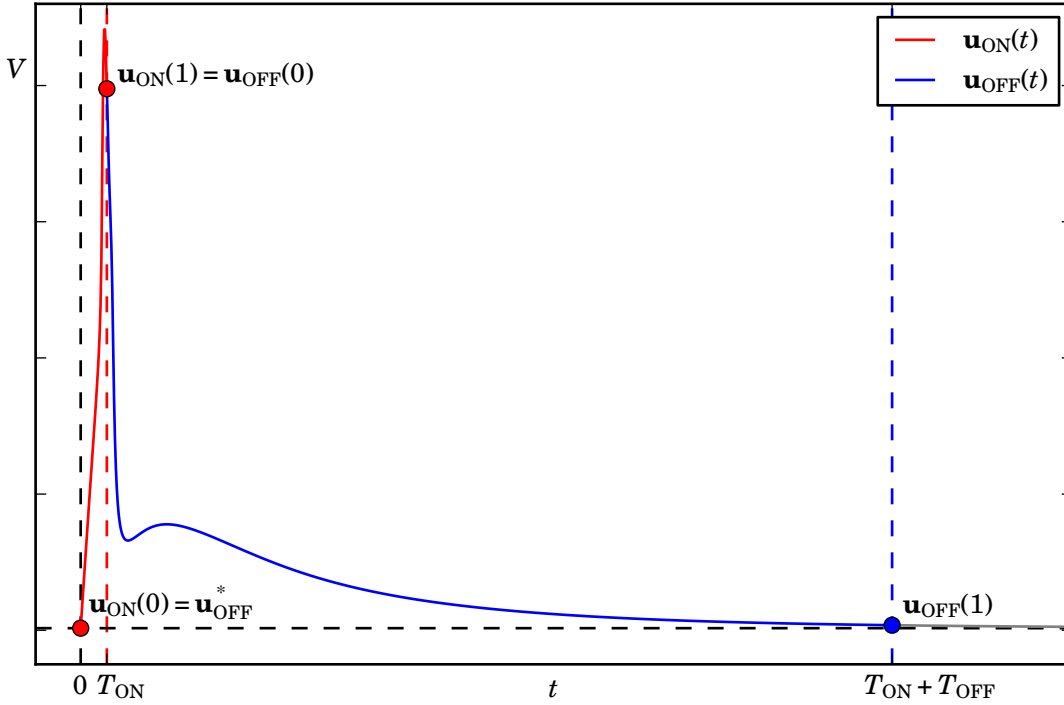


**Figure 4.2.** Formulation of system (4.1) as the boundary value problem (4.5)–(4.8). The first (red) segment is the solution  $\mathbf{u}_{\text{ON}}(t)$  of (4.1) with  $I_{\text{app}} = 20 \mu\text{A/cm}^2$  and  $\mathbf{u}_{\text{ON}}(0)$  is at the resting potential  $\mathbf{u}_{\text{OFF}}^*$ , which is an equilibrium of (4.1) with  $I_{\text{app}} = 0$  (indicated by the horizontal black dashed line); the total integration time is  $T_{\text{ON}} = 3\text{ms}$ , such that one action potential occurs. The second (blue) segment is the solution  $\mathbf{u}_{\text{OFF}}(t)$  of (4.1) with  $I_{\text{app}} = 0$  and  $\mathbf{u}_{\text{OFF}}(0) = \mathbf{u}_{\text{ON}}(1)$ ; the integration time  $T_{\text{OFF}}$  is fixed to a large enough value so that  $\mathbf{u}_{\text{OFF}}(1) \approx \mathbf{u}_{\text{OFF}}^*$ .

system (4.1) from its resting potential for a fixed duration  $T_{\text{ON}}$  as indicated by horizontal black and vertical red dashed lines. Hence, (4.5) is effectively an initial value problem with  $\mathbf{u}_{\text{ON}}(0) = \mathbf{u}_{\text{OFF}}^*$ , where  $\mathbf{u}_{\text{OFF}}^*$  is the stable equilibrium of (4.1) with  $I_{\text{app}} = 0$ ; we solve for  $\mathbf{u}_{\text{OFF}}^*$  implicitly in AUTO (Doedel, 1981; Doedel and Oldeman, 2009) and the boundary condition becomes

$$\mathbf{f}(\mathbf{u}_{\text{ON}}(0), \lambda, 0) = 0. \quad (4.7)$$

Equations (4.5) and (4.7) uniquely define the orbit segment  $\mathbf{u}_{\text{ON}}$  as a function of  $\lambda$  for fixed  $T_{\text{ON}}$ . The orbit segment  $\mathbf{u}_{\text{OFF}}$  continues on from  $\mathbf{u}_{\text{ON}}$ , but now  $I_{\text{app}} = 0$ . Hence,  $\mathbf{u}_{\text{OFF}}$  is again effectively the solution of an initial value problem with initial condition

$$\mathbf{u}_{\text{OFF}}(0) = \mathbf{u}_{\text{ON}}(1). \quad (4.8)$$

Throughout this chapter, we use  $I_{\text{app}} = 20 \mu\text{A/cm}^2$  for a total duration  $T_{\text{ON}} = 3\text{ms}$ , which

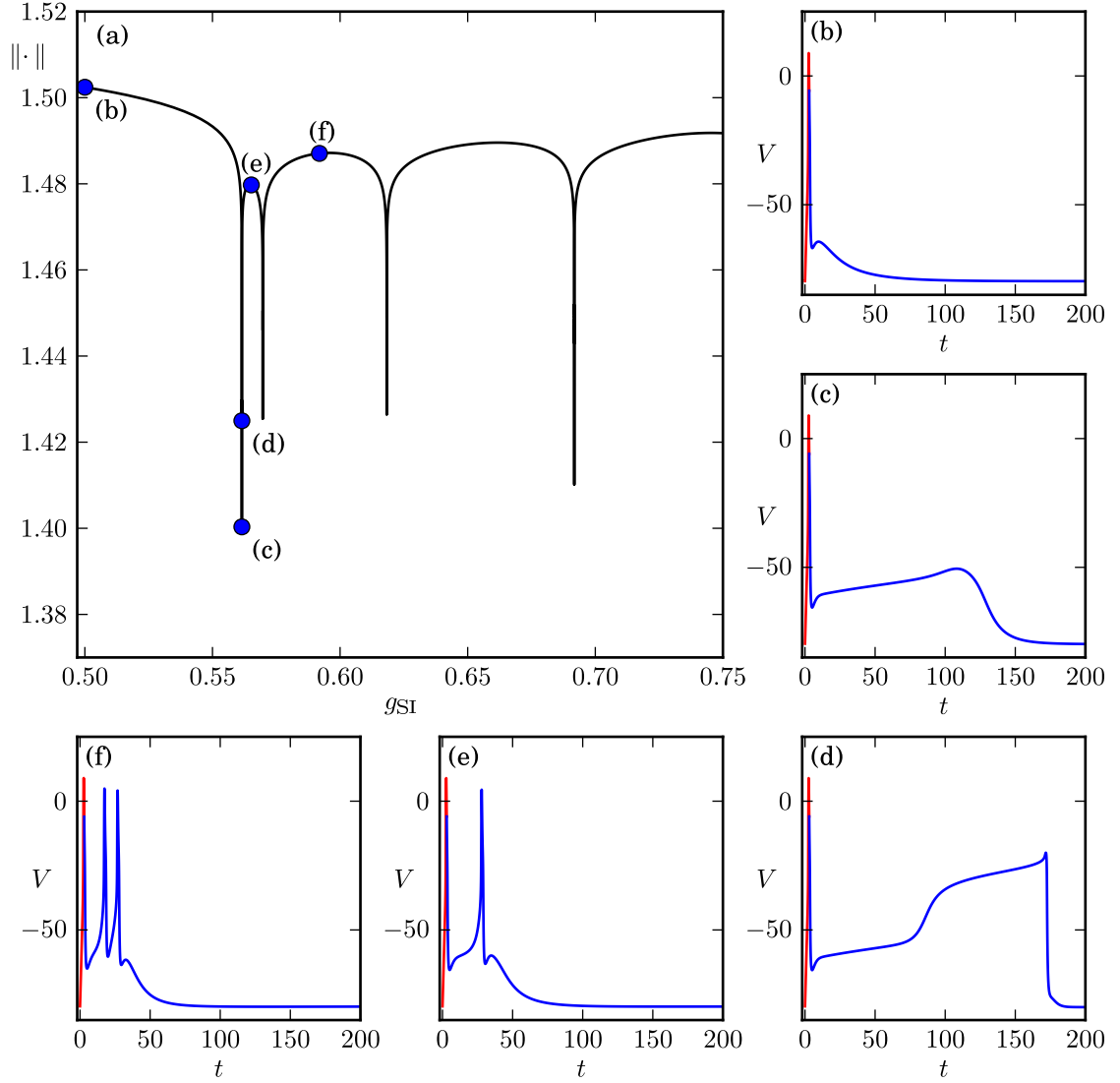


**Figure 4.3.** Continuation for increasing  $g_{\text{SI}}$  of solutions to system (4.5)–(4.8); panel (a) shows the AUTO (Doedel, 1981; Doedel and Oldeman, 2009)  $L^2$ -norm of the solution branch versus  $g_{\text{SI}}$  and illustrates that the spike-adding mechanism happens suddenly via a pronounced drop in norm; panels (b)–(f) show representative solutions along the branch, indicated by the correspondingly labelled dots in panel (a), and illustrate that solutions during a spike generation, i.e., panels (c) and (d), exhibit a stretched ADP that develops into a double step before relaxing back to the resting potential.

is long enough to drive the system past its threshold for the constants as in Table 4.1. We fix  $T_{\text{OFF}} = 297$  ms so that the total integration time of the orbit segment is  $T_{\text{ON}} + T_{\text{OFF}} = 300$  ms, which is long enough for  $\mathbf{u}_{\text{OFF}}(1)$  to be (approximately) at the resting potential. System (4.5)–(4.8) is now well posed and uniquely defines a  $\lambda$ -dependent solution family.

As illustrated by the example in Figure 4.1, we expect that increasing  $g_{\text{SI}}$  leads to a spike-

adding transition, namely, a new spike is added on top of ADP when it reaches a critical threshold of the membrane potential  $V$ . Hence, we set  $\lambda = g_{SI}$  in system (4.5)–(4.8) and solve it by continuation in AUTO (Doedel, 1981; Doedel and Oldeman, 2009), starting from  $g_{SI} = 0.5 \text{ mS/cm}^2$ . Figure 4.3(a) shows the resulting solution branch using the standard  $L^2$ -norm of AUTO (Doedel, 1981; Doedel and Oldeman, 2009) as a measure. We observe that the solution norm exhibits a series of fairly constant ‘plateaus’ that are separated by sharp downward peaks. This behaviour seems similar to that of spike-adding phenomena of periodic bursting solutions, which is organised by pairwise saddle-node bifurcations of periodics (Smolen et al., 1993; Tsaneva-Atanasova et al., 2010). However, our numerical set-up imposes a fixed initial condition, rather than a periodicity constraint. Hence, uniqueness of solutions of (4.5)–(4.8) prevents the possibility of coexisting orbit segments, that is, the branch in Figure 4.3(a) cannot have folds. The orbit segments of selected solutions along the branch are shown in Figures 4.3(b)–(f); note that we present the time series up to  $t = 200 \text{ ms}$  for clarity of the presentation.

Figure 4.3(b) shows our starting solution, i.e., a single spike followed by ADP. Along this first plateau of the solution branch up to the first downward peak all orbit segments are qualitatively like Figure 4.3(b); in particular the ADP is a small hump. As we follow the solutions into the downward peak the hump of the ADP for the orbit segments stretches out as shown in Figure 4.3(c), which lies at the bottom of the downward peak. Interestingly, as we follow the solution back up along the downward peak, the orbit segment generates a double step in the ADP, as shown in Figure 4.3(d); we selected the orbit segment with the longest double step (with respect to time). As we continue to trace the solution up along the downward peak, the small spike at the end the orbit segment grows into a fully developed spike, while the stretched double step retracts; the orbit segment shown in Figure 4.3(e) is representative for such a solution, and all orbit segments along the second plateau in Figure 4.3(a) are qualitatively like Figure 4.3(e). Figure 4.3(f) represents a solution along the next plateau, which exhibits three spikes that are created via the same process as explained above for the two-spike burst. In fact, the same spike-adding process takes place for all spike-adding transitions via the downward peaks in Figure 4.3(a). We emphasise here that the stretched single- and double-step ADPs, as shown in Figures 4.3(c) and (d), only exist along the downward peaks in Figure 4.3(a), that is, in the extremely small parameter interval during which a spike-adding transition occurs. Hence, such solutions are unlikely to be observed in actual experiments, and they are also very difficult to find in numerical experiments that use initial-value integration methods. The fact that spike-adding transition happens over an extremely small parameter interval, during which the solution measure changes rapidly, suggests that the spike-adding mechanism is organised by the difference in time scales present in system (4.1). Therefore, in order to obtain a better understanding we proceed by using geometric singular perturbation theory (GSPT) (Desroches et al., 2012; Dumortier, 1993; Fenichel, 1979; Hek, 2010; Szmolyan and Wechselberger, 2001;

Wechselberger, 2005).

### 4.3 Spike adding organised by the critical manifold

As mentioned in Section 4.1 the full five-dimensional system (4.1) contains a three-dimensional fast subsystem with variables  $V$ ,  $m_{\text{SI}}$  and  $m_{\text{FO}}$ . Since  $m_{\text{SO}}$  and  $h_{\text{SI}}$  are much slower, the idea of GSPT is to assume that  $m_{\text{SO}}$  and  $h_{\text{SI}}$  do not change at all and treat them as parameters. More precisely, we consider the *singular limit* of system (4.1) and analyse the dynamics of the layer equation

$$\frac{d\mathbf{u}}{dt} = \frac{d}{dt} \begin{pmatrix} V \\ m_{\text{SI}} \\ m_{\text{FO}} \\ m_{\text{SO}} \\ h_{\text{SI}} \end{pmatrix} = \begin{pmatrix} f_1(\mathbf{u}, \lambda, I_{\text{app}}) \\ f_2(\mathbf{u}, \lambda) \\ f_3(\mathbf{u}, \lambda) \\ 0 \\ 0 \end{pmatrix}.$$

Furthermore, because we are interested in spike-adding phenomena *after* the brief current injection, we set  $I_{\text{app}} = 0$ .

The important objects of study in the singular limit are equilibria and periodic orbits. Since  $m_{\text{SO}}$  and  $h_{\text{SI}}$  are parameters, these invariant objects occur in two-parameter families. The  $(m_{\text{SO}}, h_{\text{SI}})$ -dependent families of equilibria are known as the *critical manifold*, which we denote by  $S$ . The equilibria on  $S$  can be stable or unstable, determined with respect to the three-dimensional fast subsystem, and are typically separated by curves of fold or Hopf bifurcations. Similarly, we can expect the existence of  $(m_{\text{SO}}, h_{\text{SI}})$ -dependent families  $P$  of periodic orbits that emanate from a curve of Hopf bifurcations on the critical manifold; these periodic orbits can again be stable or unstable with respect to the three-dimensional fast subsystem. Typically, the stable periodic orbits of the fast subsystem organise the spiking phase of the bursting oscillators (Rinzel, 1987; Smolen et al., 1993; Tsaneva-Atanasova et al., 2010).

The critical manifold  $S$ , when considered in the full five-dimensional phase space of system (4.1), is a two-dimensional surface, or collection of surfaces, and the associated families of periodic orbits form a three-dimensional manifold, or collection of manifolds, that we denote by  $P$ . Together, these collections of manifolds organise the behaviour of solutions of (4.1). If  $m_{\text{SO}}$  and  $h_{\text{SI}}$  vary slowly enough, then GSPT guarantees that a solution of (4.1) (with  $I_{\text{app}} = 0$ ) will approximately trace attracting sheets of  $S$  or  $P$  that correspond to the  $(m_{\text{SO}}, h_{\text{SI}})$ -dependent families of attractors of the fast subsystem (Fenichel, 1979). For example, the transient spikes of system (4.1) trace the manifold  $P^a$  that corresponds to the family of attracting periodic orbits of the fast subsystem, while  $m_{\text{SO}}$  and  $h_{\text{SI}}$  are slowly varying (Rinzel, 1987; Rinzel and Ermentrout, 1998). More precisely, solutions of (4.1) lie on so-called slow manifolds that are perturbations of the different sheets of  $S$  from the singular limit (Fenichel,

	Two-dimensional critical manifold $S$						Three-dimensional manifold $P$	
	$S_1^a$	$S_1^r$	$S_2^a$	$S_2^r$	$S_3^r$	$S_3^a$	$P^r$	$P^a$
dimension stable manifold	5	4	5	4	3	5	4	5
dimension unstable manifold	0	3	0	3	4	0	4	0

**Table 4.2.** Overview of the different sheets and stability properties of the critical manifold  $S$  and the manifold  $P$  of periodic orbits for the simplified model (4.1), with  $g_{\text{SI}} = 0.5615 \text{ mS/cm}^2$ ; the number of sheets, as well as their stability, does not change for any of the other choices of  $g_{\text{SI}}$  considered in this chapter.

1979). Solutions of (4.1) are characterised by fast transitions between, followed by exponential contraction onto the slow manifolds. The essential difference in behaviour during a spike-adding transition is the fact that the solution of (4.1) contains a segment that traces a slow manifold associated with a sheet of  $S$  that is unstable (of saddle type) rather than attracting; see also (Desroches et al., 2012; Dumortier, 1993; Guckenheimer and Kuehn, 2009; Wechselberger, 2005). While technically the solutions of (4.1) trace slow manifolds, we will abuse notation and write ‘sheet of  $S$ ’ where we mean ‘slow manifold corresponding to the sheet of  $S$ ’ (the distance between these two manifolds is of the same order as the ratio between the time scales).

The geometry of  $S$  and  $P$  depends on the values of the other parameters in the system, such as the conductance  $g_{\text{SI}}$ . In order to illustrate the spike generation, we consider the fast subsystem at the fixed value  $g_{\text{SI}} = 0.5615 \text{ mS/cm}^2$ , which is approximately at the first downward peak in Figure 4.3(a) where the solution changes from a one-spike to a two-spike transient burst. Figure 4.4 shows the critical manifold  $S$  for this value of  $g_{\text{SI}}$  from two different viewpoints; in both views, the embedding into the five-dimensional phase space of (4.1) is projected onto the  $(h_{\text{SI}}, m_{\text{SO}}, V)$ -coordinates. The surface was obtained as follows: for ten fixed values of  $m_{\text{SO}}$  uniformly distributed in the interval  $[0, 0.4]$ , we computed the  $h_{\text{SI}}$ -dependent curves of equilibria via standard equilibrium continuation with AUTO (Doedel, 1981; Doedel and Oldeman, 2009), where we allowed  $h_{\text{SI}}$  to extend outside its physiological range of  $[0, 1]$ ; the surface  $S$  was obtained via concatenation of this collection of ten  $m_{\text{SO}}$ -slices and it is shown in Figure 4.4 with  $h_{\text{SI}}$  restricted to the interval  $[-1, 1]$  for the sake of presentation.

The critical manifold  $S$  in Figure 4.4 forms a single manifold, containing four fold curves, and can be divided into six different sheets depending on the stability type of the equilibria; the stable sheets are coloured black and the unstable ones red. The bottom (black) sheet is labelled  $S_1^a$  and it contains the resting potential as a stable equilibrium on  $S$  that is an actual equilibrium of the full five-dimensional system (4.1) with  $I_{\text{app}} = 0$ . The sheet  $S_1^a$  is connected via a curve  $F_0$  of fold bifurcation points to the sheet labelled  $S_1^r$  in Figure 4.4; this fold curve  $F_0$  lies outside  $h_{\text{SI}} \in [-1, 1]$  and is not shown in Figure 4.4. The sheet  $S_1^r$  is a two-parameter family of equilibria with two stable and one unstable eigenvalues. Hence,  $S_1^r$  has a four-dimensional

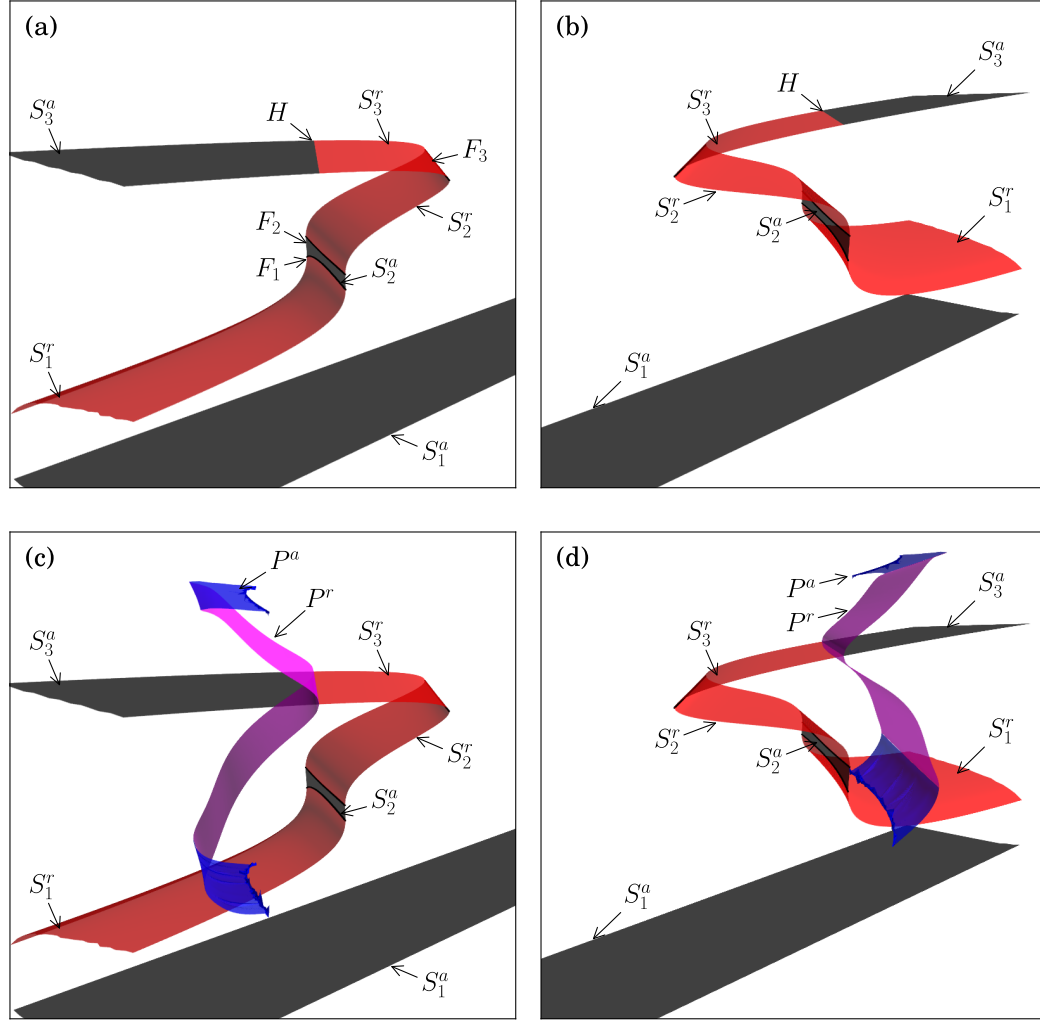


**Figure 4.4.** Critical manifolds for  $g_{\text{SI}} = 0.5615 \text{ mS/cm}^2$  embedded in the five-dimensional phase space of system (4.1); shown are projections onto  $(h_{\text{SI}}, m_{\text{SO}}, V)$ -space of the fast subsystem of (4.1), where the slow variables  $m_{\text{SO}}$  and  $h_{\text{SI}}$  are treated as parameters; panels (a) and (b) show two different view points of the surfaces of equilibria, coloured black when stable and red when not; from the same view points, panels (c) and (d) also show maxima and minima with respect to  $V$  of the two-parameter families of periodic orbits, coloured blue when stable and magenta when not. The equilibrium manifold splits into six sheets labelled  $S_1^a$ ,  $S_1^r$ ,  $S_2^a$ ,  $S_2^r$ ,  $S_3^a$ , and  $S_3^r$ , that are separated by four fold curves  $F_0$  (not shown),  $F_1$ ,  $F_2$ , and  $F_3$ , and a curve of Hopf bifurcations labelled  $H$ ; the saddle and attracting families of periodic orbits are labelled  $P^r$  and  $P^a$ , respectively. See also Table 4.2

stable and a three-dimensional unstable manifold. The next two sheets, labelled  $S_2^a$  and  $S_2^r$  have the same stability types as  $S_1^a$  and  $S_1^r$ , respectively;  $S_2^a$  is connected to  $S_1^r$  via the fold curve  $F_1$  and  $S_2^a$  and  $S_2^r$  are separated by the fold  $F_2$ . Note that the sheet  $S_2^a$  is nearly vertical

(with respect to  $V$ ), as shown in Figure 4.4; this is not an artefact of the chosen projection. The sheet  $S_3^r$  is connected to  $S_2^r$  via the fold curve  $F_3$  and this sheet consists of equilibria with one stable and two unstable eigenvalues, that is,  $S_3^r$  has a three-dimensional stable and a four-dimensional unstable manifold; the sheet  $S_3^r$  ends at the curve  $H$  of Hopf bifurcations, after which it becomes stable again and is labelled  $S_3^a$ . An overview of the different sheets and their stability properties is provided in Table 4.2.

The maxima and minima of the families of periodic orbits originating from  $H$  are shown in Figures 4.4(c) and (d), using the same two view points as in panels (a) and (b), respectively. The Hopf bifurcation is subcritical along the entire curve, so that the emanating family of periodic orbits is unstable (of saddle type), with four-dimensional stable and unstable manifolds; we coloured this family magenta and labelled it  $P^r$ . The family of periodic orbits becomes stable via a fold of periodic orbits, after which it is coloured blue and labelled  $P^a$ , and ends in a homoclinic bifurcation involving equilibria on the sheet  $S_1^r$ . We refer again to Table 4.2 for an overview of the different families and their stability properties.

Figure 4.5 illustrates how orbit segments selected from the first downward peak in Figure 4.3(a) trace the different sheets of the critical manifold  $S$  for  $g_{\text{SI}} = 0.5615 \text{ mS/cm}^2$ ; these orbit segments are all for virtually the same values  $g_{\text{SI}} \approx 0.5615 \text{ mS/cm}^2$  that differ only in the seventh decimal point, during which the manifolds  $S$  and  $P$  almost do not change at all. This extreme sensitivity of  $g_{\text{SI}}$  is a serious challenge for numerical computations, which we overcome by using continuation in AUTO (Doedel, 1981; Doedel and Oldeman, 2009) of the orbit segments defined by Equations (4.5)–(4.8). For clarity of the presentation we show only the segment  $\mathbf{u}_{\text{OFF}}(t)$ , that is, after the current injection, depicted as a blue gradient (cyan to magenta) to visualise its evolution in time. In each panel of Figure 4.5 the orbit segment starts from  $\mathbf{u}_{\text{OFF}}(0) = \mathbf{u}_{\text{ON}}(1)$ , which is located at the top-left in each panel, above the sheet  $S_3^a$ ; since  $g_{\text{SI}}$  hardly changes,  $\mathbf{u}_{\text{OFF}}(0)$  is virtually the same point in all of these panels. The orbit segments  $\mathbf{u}_{\text{OFF}}(t)$  traverse the critical manifold  $S$  before reaching the stable equilibrium of the full system (4.1), which lies on the bottom stable sheet  $S_1^a$ . Recall that the full phase space is five dimensional and Figure 4.5 may show intersections that are due to projection onto the  $(h_{\text{SI}}, m_{\text{SO}}, V)$ -coordinates; Figure 4.5 gives the best possible projection and viewpoint to illustrate the location of the one-dimensional orbit segments relative to  $S$ . Some anomalous intersections remain at isolated points, e.g., the intersection with the sheet  $S_3^a$  of  $S$ , but the observation that  $\mathbf{u}_{\text{OFF}}(t)$  traces sheets of  $S$  is real, also in the full five-dimensional space.

The spike-adding process occurs along the downward peak in Figure 4.3(a), during which the parameter  $g_{\text{SI}}$  remains almost fixed, but the orbit segments of system (4.5)–(4.8) change dramatically. We observe the formation of a stretched ADP, which initially gets increasingly longer, and which shortens again as we follow the orbit segments along the downward peak in Figure 4.3(a). This transition is initiated by the fact that, at the special value  $g_{\text{SI}} \approx 0.5615 \text{ mS/cm}^2$ , the injected current perturbs the orbit segment such that  $\mathbf{u}_{\text{ON}}(1) = \mathbf{u}_{\text{OFF}}(0)$

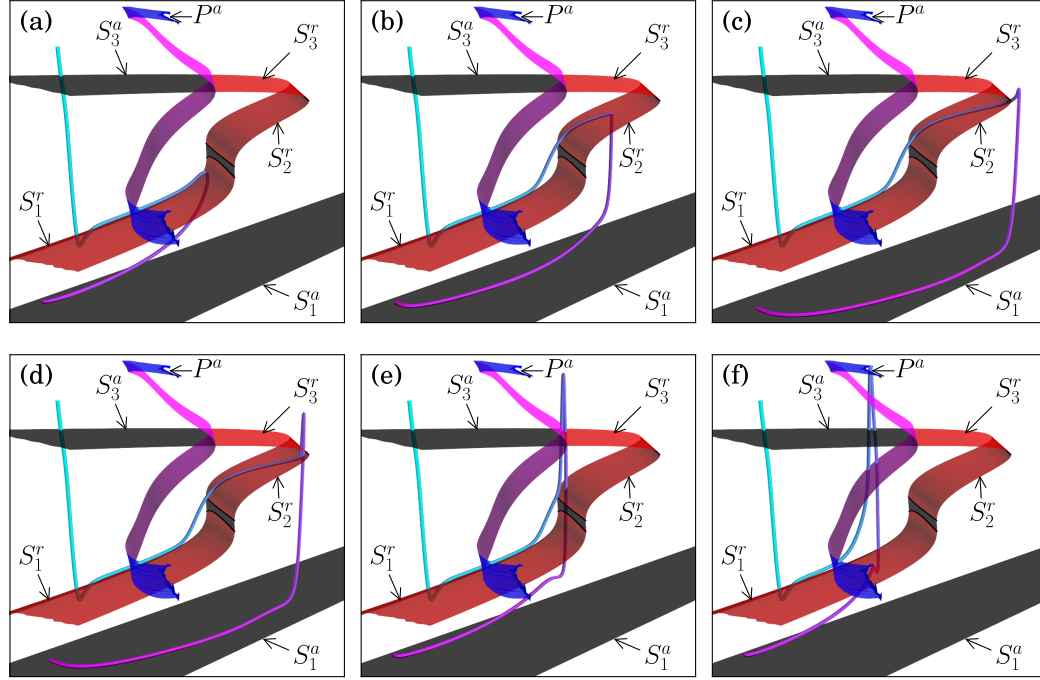


**Figure 4.5.** Orbit segments  $\mathbf{u}_{\text{OFF}}(t)$  of system (4.5)–(4.8) with  $g_{\text{SI}} \approx 0.5615 \text{ mS/cm}^2$  overlaid on the critical manifolds of Figure 4.4 with  $g_{\text{SI}} = 0.5615 \text{ mS/cm}^2$ . The orbit segments are selected along the first downward peak in Figure 4.3(a); panel (a) shows an orbit segment just before the minimum of the peak in Figure 4.3(a) is reached; panel (b) shows one shortly after; panel (c) shows the orbit segments labelled (d) in Figure 4.3(a); and panels (d)–(f) show the spike generation as the orbit segments are continued until the start of the next ‘plateau’ in Figure 4.3(a).

lies almost on the four-dimensional stable manifold of the saddle-unstable sheet  $S^r_1$ ; more precisely,  $S^r_1$  has a corresponding slow manifold with a corresponding finite-time stable manifold that  $\mathbf{u}_{\text{ON}}(1) = \mathbf{u}_{\text{OFF}}(0)$  comes close to. The closer  $\mathbf{u}_{\text{ON}}(1) = \mathbf{u}_{\text{OFF}}(0)$  lies to this four-dimensional manifold, the closer the corresponding orbit segment comes to the slow manifold associated with  $S^r_1$  and the longer it will trace this slow manifold. We approximate the slow manifold by the critical manifold  $S^r_1$  and Figure 4.5(a) shows the orbit segment from Figure 4.3(c), which traces  $S^r_1$  almost up to the fold  $F_1$  before it drops down to  $S^a_1$  and converges to the resting potential.

Figures 4.5(b)–(f) illustrate orbit segments for the second upward part of the downward peak in Figure 4.3(a). Interestingly, a double-step ADP is created via a transition from  $S^r_1$  to  $S^r_2$  as shown. The longest orbit that was previously shown in Figure 4.3(d), traces unstable sheets  $S^r_1$  to  $S^r_2$  of  $S$  all the way up to the fold  $F_3$ . This transition from  $S^r_1$  to  $S^r_2$  is, in fact, a robust part of the spike-adding process that is a continuous (parameter-dependent) variation

of the case where the folds  $F_1$  and  $F_2$  are absent, that is, where  $S_1^r$  connects directly to  $S_3^r$ ; see Section 4.3.2 for more details. After reaching the top fold  $F_3$ , the membrane potential  $V$  initially increases, instead of an immediate decrease down to the stable sheet  $S_1^a$ , and a small spike is created. As we continue to follow the solution up along the downward peak, the spike part of the orbit segment grows and moves back towards the attracting periodic orbit family  $P^a$  as illustrated in Figures 4.5(d)–(e). Finally, as shown in Figure 4.5(f), the orbit segment traces  $S_1^r$  for only a very short time before the second spike occurs; this orbit segment is selected almost at the end of the downward peak, after which orbit segments stop tracing  $S_1^r$  altogether and the transition from a one- to two-spike transient burst ends. We refer to (Govaerts and Dhooge, 2002; Guckenheimer and Kuehn, 2009; Osinga and Tsaneva-Atanasova, 2010) for similar transitions of periodic bursting oscillators.

We remark here that the manner of eventual convergence to the resting potential depends on the nature of the lift-off from the slow manifolds that correspond to the sheets  $S_1^r$  or  $S_2^r$ . Recall that both sheets  $S_1^r$  and  $S_2^r$  of the critical manifold  $S$  have three-dimensional stable manifolds; see Table 4.2. This means that the associated slow manifolds also have a one-dimensional repelling fast component (Fenichel, 1979). Hence, orbit segments that trace these saddle slow manifolds can leave it only along a single fast direction. We can see this in Figure 4.5 as a lift-off from  $S_1^r$  ‘down’ in  $V$ , shown in Figure 4.5(a), or a lift-off from  $S_1^r$  ‘up’ in  $V$ , shown in Figure 4.5(f); this uniquely-defined change in direction along the one-dimensional repelling fast component is real and not just due to the projection onto  $(h_{\text{SI}}, m_{\text{SO}}, V)$ -space. The same holds for the sheet  $S_2^r$ , for which Figures 4.5(b) and (e) are good examples that also show the required lift-off ‘up’ from  $S_1^r$  in order to reach  $S_2^r$ . In what follows, the notions ‘up’ and ‘down’ are with respect to this uniquely-defined change in direction.

The behaviour of the orbit segment of system (4.1), in relation to the critical manifold  $S$  of the fast subsystem that corresponds to the first downward peak in Figure 4.3(a), is representative for what happens along the other downward peaks in Figure 4.3(a). Each time when  $g_{\text{SI}}$  reaches a special value such that the orbit segment comes close enough to the four-dimensional stable manifold of  $S_1^r$ , it gets trapped onto  $S_1^r$  (or, more precisely, the corresponding saddle slow manifold) for increasingly longer times and the next spike-adding transition begins. For the parameters of Table 4.1, we found that this process always includes a transition between two unstable sheets, which organises the double-step ADP solutions. As mentioned before, the two sheets  $S_1^r$  and  $S_2^r$  together are perturbations of a single sheet connected to  $F_3$  that can be obtained continuously via a small parameter variation (using a suitable parameter from Table 4.1, such that the folds  $F_1$  and  $F_2$  disappear in a curve of cusp bifurcations). Therefore, in the next section, we first explain the jump at the end of the canard-like behaviour, that is, the behaviour near the fold  $F_3$  that separates the two unstable sheets  $S_2^r$  and  $S_3^r$ . We then discuss the transition between  $S_1^r$  and  $S_2^r$  in Section 4.3.2. Section 4.3.3 illustrates how the spike-adding mechanism can change when additional equilibria are present.

### 4.3.1 Slow flow on the critical manifold near $F_3$

Let us first focus our attention on the behaviour near the fold  $F_3$ , that is, the transition from Figures 4.5(c) to (d). The behaviour near folds can be explained by analysis of the slow flow on the critical manifold  $S$  (Desroches et al., 2012). The slow flow on  $S$  is defined by the differential algebraic system

$$\begin{pmatrix} 0 \\ 0 \\ 0 \\ \dot{m}_{SO} \\ \dot{h}_{SI} \end{pmatrix} = \begin{pmatrix} f_1(\mathbf{u}, \lambda) \\ f_2(\mathbf{u}, \lambda) \\ f_3(\mathbf{u}, \lambda) \\ f_4(\mathbf{u}, \lambda) \\ f_5(\mathbf{u}, \lambda) \end{pmatrix}. \quad (4.9)$$

Here, we always have  $I_{app} = 0$ . Recall that the gating variables of (4.1) are only coupled through the membrane potential  $V$ . In fact, it is easy to solve equations  $f_2(\mathbf{u}, \lambda) = 0$  and  $f_3(\mathbf{u}, \lambda) = 0$  explicitly, which gives us the solutions for the fast gating variables  $m_{SI} = m_{SI_\infty}(V)$  and  $m_{FO} = m_{FO_\infty}(V)$ . We substitute these solutions into  $f_1$  to obtain

$$\begin{pmatrix} 0 \\ \dot{m}_{SO} \\ \dot{h}_{SI} \end{pmatrix} = \begin{pmatrix} f_1^*(V, m_{SO}, h_{SI}, \lambda) \\ f_4^*(V, m_{SO}, \lambda) \\ f_5^*(V, h_{SI}, \lambda) \end{pmatrix},$$

that is, the slow flow on the two-dimensional critical manifold  $S$  is defined by two ordinary differential equations for  $m_{SO}$  and  $h_{SI}$  and a single algebraic constraint  $f_1^*(V, m_{SO}, h_{SI}, \lambda) = 0$ . Unfortunately,  $S$  is folded with respect to  $V$  so that  $m_{SO}$  and  $h_{SI}$  do not uniquely define  $V$ ; however, the algebraic constraint does uniquely define  $m_{SO}$  or  $h_{SI}$  from given pairs  $(V, m_{SO})$  or  $(V, h_{SI})$ , respectively; compare also Figures 4.4(a) and (b). Hence, it is advantageous to express the slow flow in terms of only one of the slow variables  $m_{SO}$  or  $h_{SI}$  together with the fast variable  $V$ .

We choose to work with  $V$  and  $m_{SO}$ . If we formally differentiate the algebraic constraint we obtain

$$\begin{pmatrix} \dot{V} \\ \dot{m}_{SO} \end{pmatrix} = \begin{pmatrix} \left[ -\frac{\partial f_1^*}{\partial V} \right]^{-1} \left[ \frac{\partial f_1^*}{\partial m_{SO}} f_4^* + \frac{\partial f_1^*}{\partial h_{SI}} f_5^* \right] \\ f_4^* \end{pmatrix}, \quad (4.10)$$

where  $h_{SI}$  is uniquely determined from  $f_1^*(V, m_{SO}, h_{SI}, \lambda) = 0$ . We refer to (Desroches et al., 2012) for more details on this step. Note that (4.10) becomes singular when  $\partial f_1^*/\partial V = 0$ , that is, precisely where  $S$  has folds with respect to  $V$ . We can desingularise the flow by scaling time with the factor  $-\partial f_1^*/\partial V$ . This rescaling reverses the direction of the time whenever

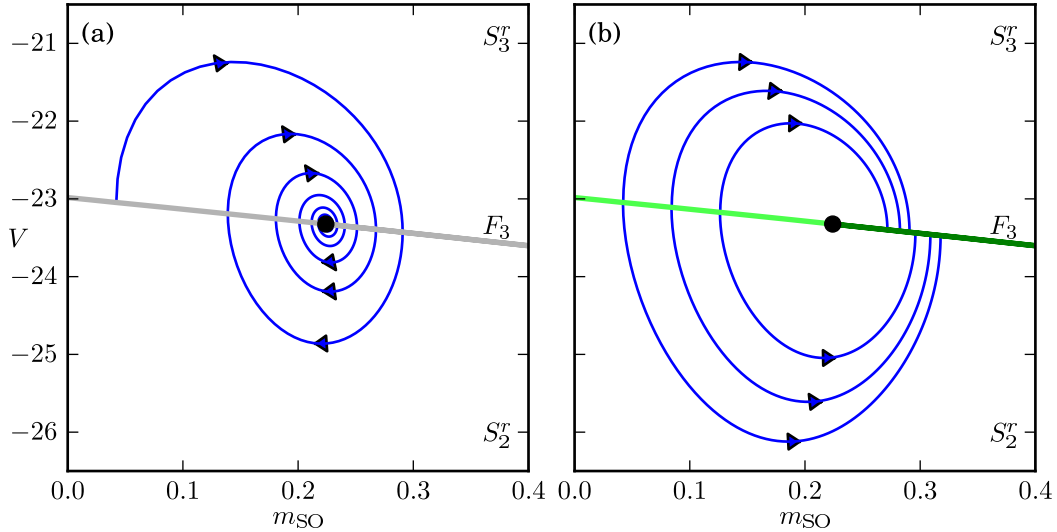


**Figure 4.6.** Phase portraits on the sheets  $S_2^r$  and  $S_3^r$  of the critical manifold  $S$  near the fold  $F_3$ ; panel (a) shows a trajectory of the desingularised slow flow (4.11), which converges to an attracting focus on  $F_3$  (grey line); panel (b) shows projected trajectories of the slow flow (4.9); the repelling and attracting nature of  $F_3$  is indicated by light- and dark-green colours, respectively.

$\partial f_1^*/\partial V > 0$  and we obtain the desingularised slow flow in the form

$$\begin{pmatrix} \dot{V} \\ \dot{m}_{SO} \\ 0 \end{pmatrix} = \begin{pmatrix} \frac{\partial f_1^*}{\partial m_{SO}} f_4^* + \frac{\partial f_1^*}{\partial h_{SI}} f_5^* \\ -\frac{\partial f_1^*}{\partial V} f_4^* \\ f_1^* \end{pmatrix}. \quad (4.11)$$

The actual slow flow on  $S$  is now defined by the desingularised slow flow (4.11), where we must take into account the time reversal in the regimes where  $\partial f_1^*/\partial V > 0$ . Figure 4.6 illustrates this for a neighbourhood of the fold  $F_3$  on  $S$  that separates the sheets  $S_2^r$  and  $S_3^r$ ; we have  $\partial f_1^*/\partial V < 0$  on  $S_3^r$  and  $\partial f_1^*/\partial V > 0$  on  $S_2^r$ . The phase portraits in Figure 4.6 are projected onto the  $(m_{SO}, V)$ -plane. Figure 4.6(a) shows how a trajectory of (4.11) near  $F_3$  (grey line) is attracted to a focus equilibrium of the desingularised slow flow, marked with a black dot on  $F_3$ . Figure 4.6(b) shows the corresponding projection of the slow flow (4.9) on  $S$ ; note the change in direction of the flow for the region where  $\partial f_1^*/\partial V > 0$ . The fold  $F_3$  in Figure 4.6(b) is now divided into two parts, a repelling segment on the left side of the focus equilibrium (light-green line) and an attracting segment on the right side of the focus equilibrium (dark-green line). In fact, the focus equilibrium is no longer a focus; it has become a folded singularity or, more precisely, a folded focus. We refer to (Desroches et al., 2012; Wechselberger, 2005) for more details.

Figure 4.7 shows a zoom of the sheets  $S_2^r$  and  $S_3^r$  of the critical manifold near the folded

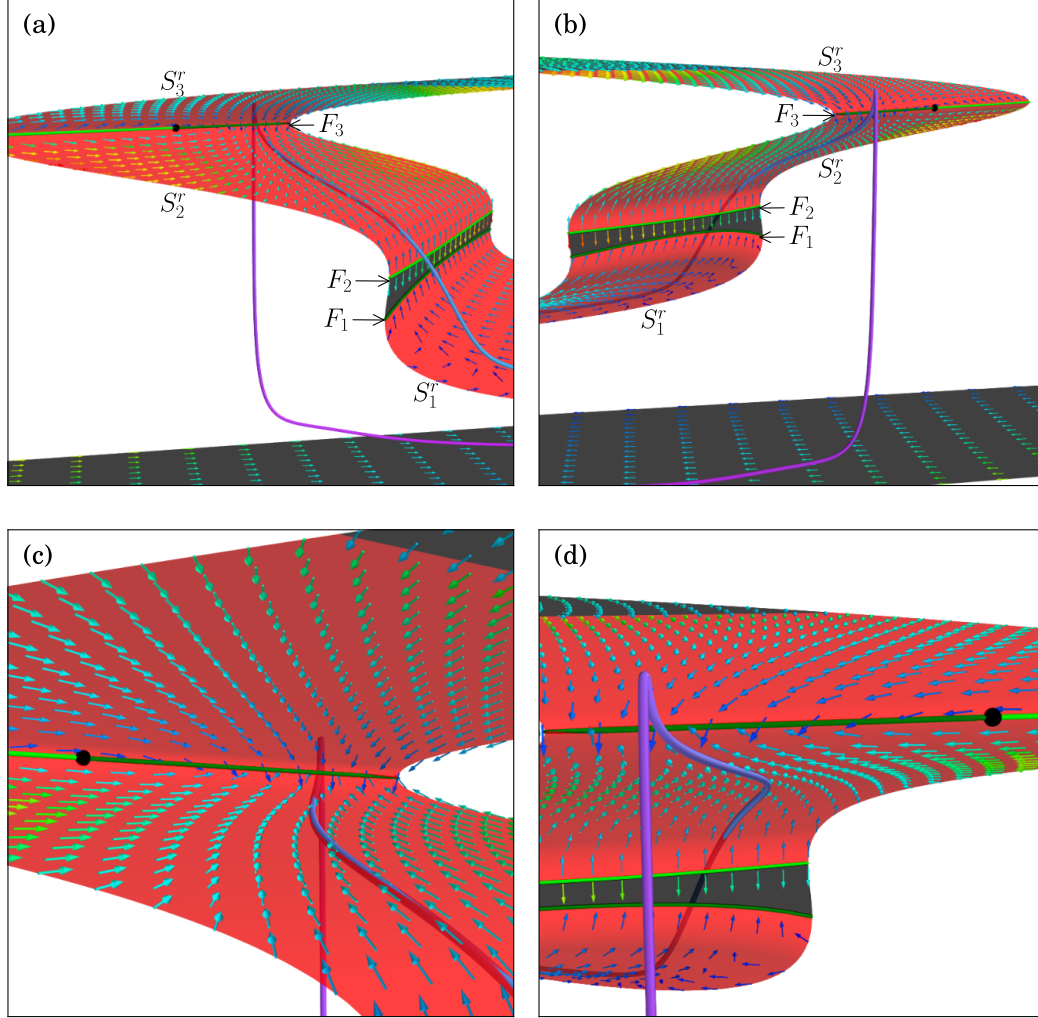


**Figure 4.7.** Vectors of the slow flow on  $S$  near the top fold  $F_3$  together with the orbit segment from Figure 4.5(c); the direction of flow on  $S$  is indicated by the arrows, where hotter colours correspond to vectors with larger magnitudes. The folded focus is the black dot on  $F_3$ , with the uniformly repelling and attracting parts of  $F_3$  coloured light and dark green, respectively. Panels (a) and (b) show the process from two different viewpoints, and panels (c) and (d) show corresponding close-up views near  $F_3$ .

singularity, with the orbit segment from Figure 4.5(c) depicted by a blue-gradient curve as before; panels (a) and (b) provide two different viewpoints and panels (c) and (d) two corresponding close-up views. The slow flow is visualised as a vector field on  $S$ , where hotter colours depict vectors with a higher magnitude (the length of the vectors is constant for clarity of presentation). The fold  $F_3$  in Figure 4.7 is coloured the same dark and light green as in

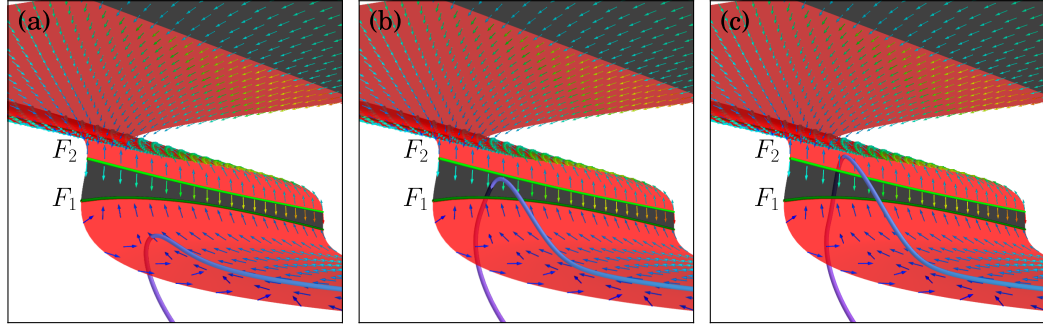
Figure 4.6(b). The inside- and top-view of the critical manifold are presented in Figures 4.7(a) and (b), respectively.

Figure 4.7 shows that the orbit segment follows the slow flow on  $S_2^r$  as it approaches  $F_3$ . As shown in Figures 4.7(a) and (b) in a neighbourhood of the folded focus the slow flow has the form of large semi-cycles that cause the orbit segment to trace  $S_2^r$  laterally and, at the same time, push it toward  $F_3$ . Since the flow on the top sheet  $S_3^r$  also points towards  $F_3$  as shown in Figures 4.7(c) and (d), the orbit segment cannot pass  $F_3$  and reaches a so-called jump point; compare also with Figure 4.6(b). At the jump point, the fast directions of the flow take over, which causes the formation of a small spike as the orbit segment leaves  $S$ ; see also Figure 4.5(c). Let us emphasise here that the behaviour of the orbit segments near  $F_3$  does not involve interactions with the slow flow on  $S_3^r$ ; this impression is given by the projections onto  $(h_{\text{SI}}, m_{\text{SO}}, V)$ -coordinates shown in Figure 4.5, particularly in panels (d) and (e). As mentioned at the end of Section 4.3, the spike-formation that develops as soon as an orbit segment has reached  $F_3$  is due to a lift-off ‘up’ from  $S_2^r$  or  $S_1^r$ , as in Figure 4.5(f), and takes place on the fast time scale; the spike and subsequent drop down to  $S_1^a$  misses both surfaces  $S_3^r$  and  $S_2^r$  entirely.

### 4.3.2 Slow flow of the critical manifold near the folds $F_1$ and $F_2$

The formation of a new well-developed spike occurs over a very small parameter interval around  $g_{\text{SI}} \approx 0.5615 \text{ mS/cm}^2$  for which the effect of the injected current is precisely such that the orbit segment comes close to the four-dimensional stable manifold of  $S_1^r$ . The behaviour of the orbit segment near the top fold  $F_3$  corresponds to the onset of such a new spike, but the process of reaching  $F_3$ , as illustrated in Figures 4.5(a) and (b), as well as the further development of the spike, as illustrated in Figures 4.5(d)–(f), involves the creation of a double-step ADP; this behaviour is organised by a (fast) jump from  $S_1^r$  to another saddle-unstable sheet  $S_2^r$ . Such a jump, which is actually a jump between the two corresponding unstable slow manifolds, is a phenomenon that occurs robustly as part of the spike-adding mechanism and has previously been observed for periodic orbits in planar systems; it was reported as a new type of canard called *fold-initiated canards* in (Guckenheimer and Hoffman, 2000) and a slightly different version termed *ducks with relaxation* is discussed in (Arnol'd et al., 1994, Ch. 4, Sec. 5.4). In fact, the behaviour we observe in our model is essentially planar and very similar to the example discussed in (Guckenheimer and Hoffman, 2000). Indeed, there are no folded singularities on the folds  $F_1$  and  $F_2$ , which means that each fold point has the same effect on the dynamics and the slow flow is essentially one dimensional. Furthermore, the repelling fast component of the slow manifolds associated with  $S_1^r$  and  $S_2^r$  is one dimensional as well.

The presence of the folds  $F_1$  and  $F_2$  results in the formation of a double-step ADP during the spike-adding process; see Figures 4.5(a) and (b). The double-step creation is a direct con-



**Figure 4.8.** Vectors of the slow flow on  $S$  in the vicinity of the two folds  $F_1$  and  $F_2$  that mark the transition of the orbit segment between the two unstable sheets  $S_1^r$  and  $S_2^r$ ; the direction of flow on  $S$  is indicated by the arrows, where hotter colours correspond to vectors with larger magnitudes. The attracting fold  $F_1$  is dark green and the repelling fold  $F_2$  is light green. Panels (a)–(c) show the same perspective with orbit segments that almost reach  $F_1$ , reach  $F_1$  via the attracting sheet  $S_2^a$ , and reach  $F_2$  with a jump from  $S_1^r$  to  $S_2^r$ , respectively.

sequence of the fact that the direction of the slow flow on  $S$  is transverse to both fold curves  $F_1$  and  $F_2$ ; this is illustrated in Figure 4.8. Figure 4.8(a) shows the same orbit segment as in Figure 4.5(a), and Figures 4.8(b) and (c) show two subsequent orbit segments that both occur before the case shown in Figure 4.5(b). As before, the orbit segments are depicted as blue-gradient curves and the colour-coded vectors indicate the slow flow on  $S$ . We observe that the orbit segment in Figure 4.8(a) exhibits a lift-off down from  $S_1^r$  before a fast jump down to  $S_1^a$  returns the system to its resting potential, while the two orbit segments in Figures 4.8(b) and (c) exhibit a lift-off up from  $S_1^r$ . These orbit segments are all part of the same continuously parametrised family of orbit segments that trace  $S_1^r$ ; each orbit segment corresponds to a unique value of  $g_{SI}$ , even though we always have  $g_{SI} \approx 0.5615 \text{ mS/cm}^2$  and the variation is very small, occurring only in the seventh decimal place.

Let us consider this continuously parametrised family of orbit segments as identified by the moment of lift-off (first down and then up) from  $S_1^r$ . At the start of the spike-adding process, orbit segments trace only the saddle-unstable sheet  $S_1^r$  before a lift-off down to  $S_1^a$  returns the system to its resting potential; the example in Figure 4.8(a) shows an orbit segment that almost reaches  $F_1$ . As  $g_{SI} \approx 0.5615 \text{ mS/cm}^2$  increases continuously (but by only very small amount), the orbit segments come increasingly closer to  $S_1^r$  until one actually reaches  $F_1$ ; these orbit segments grow increasingly longer stretched ADPs.

Using the analysis via the desingularised slow flow (4.11) as derived in Section 4.3.1, we can decide what happens when an orbit segment reaches  $F_1$ . We find that the desingularised slow flow (4.11) does not have any equilibria in the neighbourhood of the two folds  $F_1$  and  $F_2$ , which means that there are no folded singularities on either  $F_1$  or  $F_2$ ; the fold curve  $F_1$  is

uniformly attracting, which we indicated by a dark-green colour, and  $F_2$  is uniformly repelling, indicated by a light-green colour. Hence, upon reaching  $F_1$ , the orbit segment simply jumps down toward the resting potential and subsequent orbit segments exhibit a lift-off up from  $S_1^r$ . Since the sheet  $S_2^a$  on the other side of  $F_1$  is attracting, the fast directions will push these orbit segments toward  $S_2^a$ , provided the lift-off up from  $S_1^r$  occurs not too far away from  $F_1$ . Note that the slow flow on  $S_2^a$  points back to  $F_1$ , so these orbit segments that reach  $S_2^a$  will flow to  $F_1$  from the other side and again drop down to  $S_1^a$  that way; an example is shown in Figure 4.8(b).

As we continue to increase  $g_{SI} \approx 0.5615 \text{ mS/cm}^2$  ever so slightly, orbit segments will converge to  $S_2^a$  closer and closer near  $F_2$ , until the lift-off up from  $S_1^r$  happens earlier, far enough from  $F_1$ , such that they may reach  $F_2$ . In order to determine what happens when an orbit segment reaches  $F_2$ , we must remember that system (4.1) and, hence, the slow flow on  $S$  depend continuously on  $g_{SI}$ . This means that the family of orbit segments is also continuous and the orbit segment that reaches  $F_2$  is a continuous variation of an orbit segment that experiences a lift-off up from  $S_1^r$  later, so that it still converges to  $S_2^a$  and flows back to  $F_1$ , as well as an orbit segment that experiences a lift-off up from  $S_1^r$  earlier, so that it misses  $F_2$  altogether and forms a well-developed spike as illustrated in Figure 4.5(f). Therefore, the family of orbit segments must include a subfamily of orbit segments that experience a lift-off from  $S_2^r$ ; just as for  $S_1^r$ , the lift-off will first be down, as a continuous variation from the orbit segments that flow along  $S_2^a$ , and then up, to transform into an orbit segment that misses  $F_2$  altogether. This subfamily exists in a (doubly) very small parameter regime of fold-initiated canard behaviour (Guckenheimer and Hoffman, 2000) and consists of orbit segments that exhibit a double-step ADP.

Another way to understand this phenomenon is in terms of singularity theory, which suggests that  $S_1^r$  and  $S_2^r$  are part of the same surface that unfolds a cusp singularity. Recall that the critical manifold  $S$  is a collection of families of equilibria of the fast subsystem of (4.1); the folds  $F_1$  and  $F_2$  are curves of saddle-node bifurcations that exist robustly in the  $(m_{SO}, h_{SI})$ -parameter plane organised by the two slow variables. Since  $F_1$  and  $F_2$  are typically not parallel, they will meet; note that  $F_1$  and  $F_2$  may need to be extended into an unphysical parameter regime of the  $(m_{SO}, h_{SI})$ -plane. Singularity theory tells us that the two fold curves  $F_1$  and  $F_2$  typically meet at a cusp point and end there, which means that the two sheets  $S_1^r$  and  $S_2^r$  merge into one in this region of the  $(m_{SO}, h_{SI})$ -plane. The existence of a double-step ADP then merely depends on the location relative to the cusp point of the interaction between the orbit segments and the critical manifold  $S$ . We remark that a small change in one or more of the parameters given in Table 4.1 may move the cusp point into the physical regime, or such that  $F_1$  and  $F_2$  no longer exist for physiologically realistic values of  $m_{SO}$  and  $h_{SI}$ ; in the latter case, the spike-adding transition will not feature a double-step ADP.

### 4.3.3 Spike adding when additional equilibria are present

It turns out that the spike-adding mechanism organised by canard-like behaviour during the downward peaks of Figure 4.3(a) always features a double-step ADP stage involving a jump between  $S_1^r$  and  $S_2^r$ . Hence, each downward peak in Figure 4.3(a) corresponds to a qualitatively similar transition as discussed for the first one at  $g_{SI} \approx 0.5615 \text{ mS/cm}^2$ . If we increase  $g_{FO}$  from the fixed value  $g_{FO} = 9.5 \text{ mS/cm}^2$  that was used in Figure 4.3 to the new value  $g_{FO} = 9.6 \text{ mS/cm}^2$  then the nature of spike adding changes due to the presence of additional unstable equilibria of system (4.1). If we again continue the two-point boundary value problem (4.5)–(4.8) as before with  $\lambda = g_{SI}$ , but  $g_{FO} = 9.6 \text{ mS/cm}^2$  set to its new value, we get a bifurcation diagram similar to the one for  $g_{FO} = 9.5 \text{ mS/cm}^2$  shown in Figure 4.3. In fact, the spike-adding mechanism for the first four additional spikes involves a double-step ADP stage as we have seen in the previous section. However, for  $g_{SI} \approx 0.7672 \text{ mS/cm}^2$ , that is, just before the transition from five to six spikes, a saddle-node bifurcation occurs on the saddle-unstable sheet  $S_1^r$ . This creation of two new (unstable) equilibria prevents a double-step ADP stage; the spike-adding mechanism only involves orbit segments exhibiting a stretched ADP with a single step and there is no longer a jump between unstable slow manifolds.

Let us focus on the transition from a burst with five to one with six spikes, which takes place at  $g_{SI} \approx 0.7842 \text{ mS/cm}^2$ . For this value of  $g_{SI}$  there exist three equilibria, but only one is stable so that there is no bistability. The stable equilibrium is the resting potential on  $S_1^a$ . The other two equilibria are saddles, one with one and one with two unstable eigenvalues, denoted  $s_1$  and  $s_2$  respectively; these additional saddle equilibria are located on  $S_1^r$ . We calculate the critical manifold  $S$  of the fast subsystem for  $g_{SI} = 0.7842 \text{ mS/cm}^2$ ; it is shown in Figure 4.9 projected onto  $(h_{SI}, m_{SO}, V)$ -space. Figure 4.9 illustrates that the critical manifold does not change qualitatively for higher values of  $g_{FO}$  and  $g_{SI}$ ; compare with Figure 4.4. Two orbit segments, one selected from the falling slope and one from the rising slope of the downward peak at  $g_{SI} \approx 0.7842 \text{ mS/cm}^2$  are superimposed onto  $S$ ; see Figures 4.9(a) and (b), with enlargements in Figures 4.9(c) and (d), respectively. As before, only the part of the orbit segments that starts after the current injection is shown, so only the downward part of the first of the five spikes is visible. The enlargements in Figures 4.9(c) and (d) also show the slow flow on  $S$  in a neighbourhood of the two equilibria, and better visualise the interaction of the two orbit segments with  $s_1$  and  $s_2$ . The equilibria  $s_1$  and  $s_2$  are both saddles, but with respect to the slow flow on  $S$ , the equilibrium  $s_1$  is stable (black dot) and  $s_2$  is a saddle (red dot).

The value  $g_{SI} \approx 0.7842 \text{ mS/cm}^2$  for this case with  $g_{FO} = 9.6 \text{ mS/cm}^2$  is again special because at the end of the oscillations, when the orbit segment reaches the family of homoclinic orbits where  $P^a$  ends, it lies extremely close to the four-dimensional stable manifold of  $S_1^r$  so that it drops down and traces the unstable sheet  $S_1^r$  of  $S$ . The difference with the spike-adding mechanism illustrated in Figure 4.5 is that the behaviour of the orbit segment on  $S_1^r$

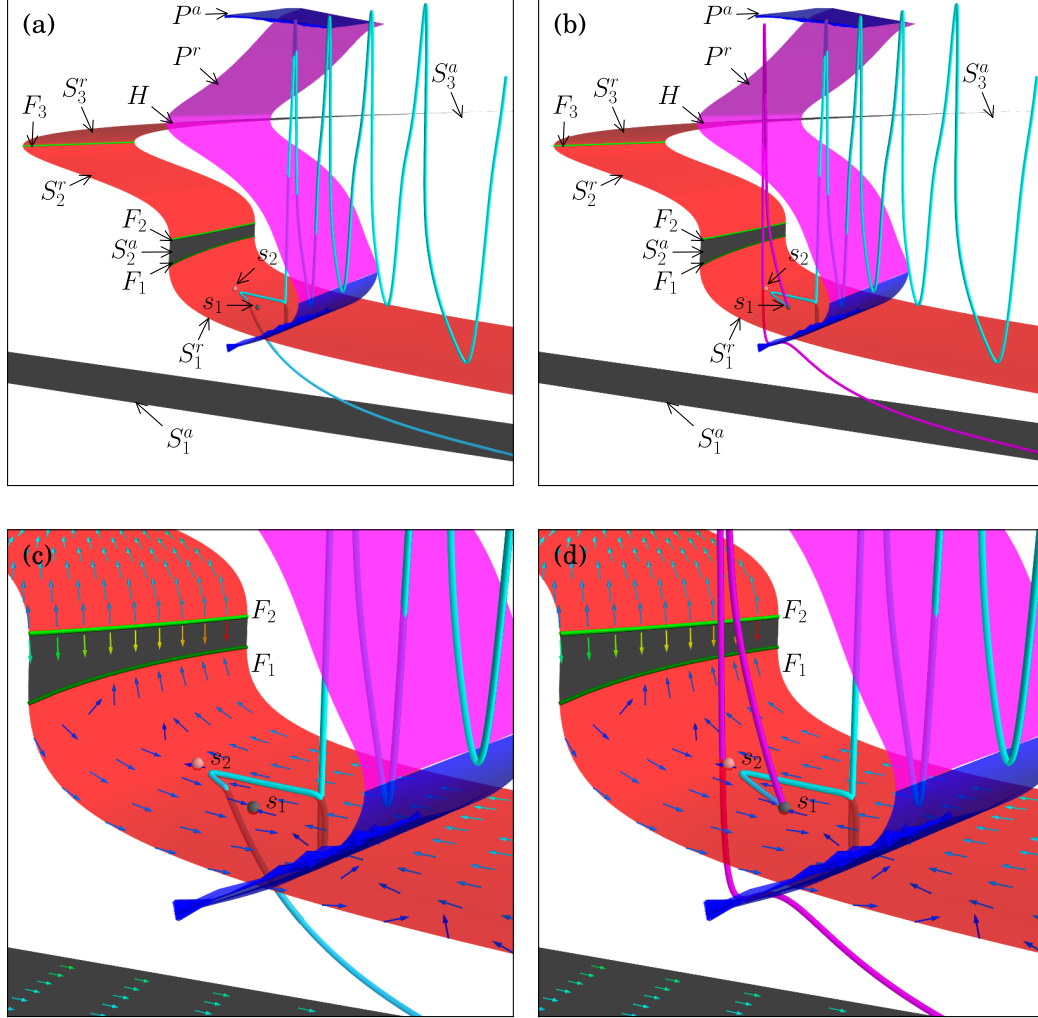


**Figure 4.9.** The critical manifold calculated for  $g_{FO} = 9.6 \text{ mS/cm}^2$  and  $g_{SI} = 0.7842 \text{ mS/cm}^2$  projected onto  $(h_{SI}, m_{SO}, V)$ -space; superimposed in the left and right column are orbit segments with  $g_{SI} \approx 0.7842$  selected from the falling and rising slopes of the downward peak, respectively. Panels (a) and (b) show and overall view and panels (c) and (d) enlargements near  $F_1$  and  $F_2$  along with the associated slow flow. The two unstable equilibria  $s_1$  and  $s_2$  of the full system are marked with black and red dots, because they are an attractor and a saddle on  $S_1^r$ , respectively.

is affected by the presence of the equilibria  $s_1$  and  $s_2$ . With respect to the two-dimensional slow flow on  $S_1^r$ , the equilibrium  $s_1$  is an attractor and all orbit segments on  $S_1^r$  converge to  $s_1$ , provided they lie in its basin of attraction, which is bounded by the one-dimensional stable manifold of the saddle  $s_2$ . In terms of the full five-dimensional flow,  $S_1^r$  is obviously repelling, and orbit segments that come close enough to  $S_1^r$  will behave according to the slow flow for

only a finite amount of time; this means that convergence to  $s_1$  will eventually be followed by a fast repulsion away from  $S_1^r$ . The orbit segment in Figures 4.9(a) and (c) enters a close enough neighbourhood of  $S_1^r$  in the region of the basin of attraction of  $s_1$ ; hence, for the time that it is following the slow flow, it converges to  $s_1$ , but we can clearly see in Figure 4.9(c) that the fast directions take over before it reaches  $s_1$ . Since this orbit segment was selected from the falling slope of the downward peak of the spike-adding mechanism, the orbit segment jumps straight down toward  $S_1^a$ , where it converges to the resting potential. Orbit segments on this slope that lie closer to the minimum of the downward peak would reach  $s_1$ , but still jump down toward  $S_1^a$  when the fast directions take over. On the other hand, orbit segments from the rising slope of the downward peak eventually experience a lift-off ‘up’ from  $S_1^r$ , so that a large action potential occurs before converging back to the resting potential; this change of direction corresponds to the onset of a new spike, which is more dramatic and abrupt than the gradual increase in  $V$  followed by a small-amplitude spike as illustrated in Figure 4.5. Continuity of the vector field (4.1) implies that there exists an orbit segment that actually converges to the saddle  $s_1$  and never relaxes back to the resting potential.

Continuity of the vector field (4.1) implies that there exists an orbit segment that actually converges to the saddle  $s_1$  and never relaxes back to the resting potential. This happens when  $g_{SI} \approx 0.7842 \text{ mS/cm}^2$  is exactly at the value where the perturbed trajectory lies on the four-dimensional stable manifold  $W^s(s_1)$  of the equilibrium  $s_1$ . In contrast to the four-dimensional stable manifold of  $S_1^r$ , the manifold  $W^s(s_1)$  is invariant under the flow of (4.1) and this heteroclinic connection is a well-defined bifurcation for system (4.1). Such heteroclinic connections have been studied extensively in the context of excitability thresholds (Krauskopf et al., 2003; Wieczorek et al., 1999, 2002).

We remark here that the presence of additional equilibria such as  $s_1$  and  $s_2$  in the example discussed only affects the spike-adding mechanism if the orbit segments that trace  $S_1^r$  enter the basin of attraction of  $s_1$ . If such orbit segments trace  $S_1^r$  on the other side of the stable manifold of  $s_2$ , then a double-step ADP stage would occur. We know from our further model analysis (not shown) that the unstable equilibria persists for higher values of  $g_{SI}$  as well as  $g_{FO}$ , and in all cases that we investigated, these additional equilibria on  $S_1^r$  affect the spike generation in the way as described above.

## 4.4 Conclusion

In this chapter we performed a detailed analysis of the mechanisms of spike adding in a transient burst. Based on a reduction of our previous model presented in Chapter 2, we identify these mechanisms using numerical continuation of orbit segments that are solutions to a well-posed boundary value problem. In our analysis we utilised the separation of time scales in

system (4.1). We calculated the two-dimensional critical manifold  $S$  of the fast subsystem, which organises the behaviour of the five-dimensional system. The spike-adding process is characterised by the fact that orbit segments trace unstable slow manifolds that correspond to unstable sheets of  $S$ . More precisely, there are two unstable sheets  $S_1^r$  and  $S_2^r$  on which all points have only a one-dimensional repelling fast component; this means that the lift-off from the associated unstable slow manifolds is characterised by a uniquely-defined direction. The changes in sign of this direction marks the different phases of the spike-adding transition. Moreover, we have shown that at least two variants of spike-adding mechanisms are possible.

In the next chapter we will illustrate how the spiking threshold organised by this canard-like mechanism, which is characterised by the elongated ADP, can be associated with extrema of a slow variable. Namely, after the orbit segment reaches the jump point it retracts back, creating an extremum with respect to one or more of the slow variables. We use this distinctive feature along with numerical continuation to compute the onset of ADP and a spike.

# **Chapter 5**

## **Continuation-based numerical analysis of after-depolarisation and spike-adding threshold**

Our primary motivation in this chapter is to study the transient bursting related to the after-depolarisation (ADP) and how it evolves as a function of neuronal biophysical properties. To study transitions between different behaviours we consider a simplified model of pyramidal neurons previously presented in Chapter 4. We study such transient behaviour via continuation of orbit segment that are solutions of a two-point boundary value problem (2PBVP). We divide trajectories into two parts, one that corresponds to the system with current injection and a subsequent one where the current has been turned off. Each trajectory is the unique solution of a 2PBVP, which consists of two orbit segments, that are linked via boundary conditions. The resulting 2PBVP can be continued in system parameters. We use this formulation to study ADP and burst of a simple bursting neuron model but the formulation is, in fact, quite general and could be applied to other problems. To establish the boundaries of different behaviour we find the onset of ADP and a spike. We show that both ADP and a spike corresponds to extrema of a slow variable of the system. Using numerical continuation we show that such extrema are folds of a bifurcation curve. Consequently, the fold continuation allows us to establish the boundaries of different behaviour of the model in two parameters. Based on our analysis we draw the implications of changes to model parameters for excitability. We also investigate in detail the model behaviour at the computed boundaries.

### **5.1 ADP as a boundary value problem**

We formulate the transient phenomenon of ADP as a boundary value problem using the previously defined system (4.1) in Chapter 4. Similarly, we focus on how the system depends on the

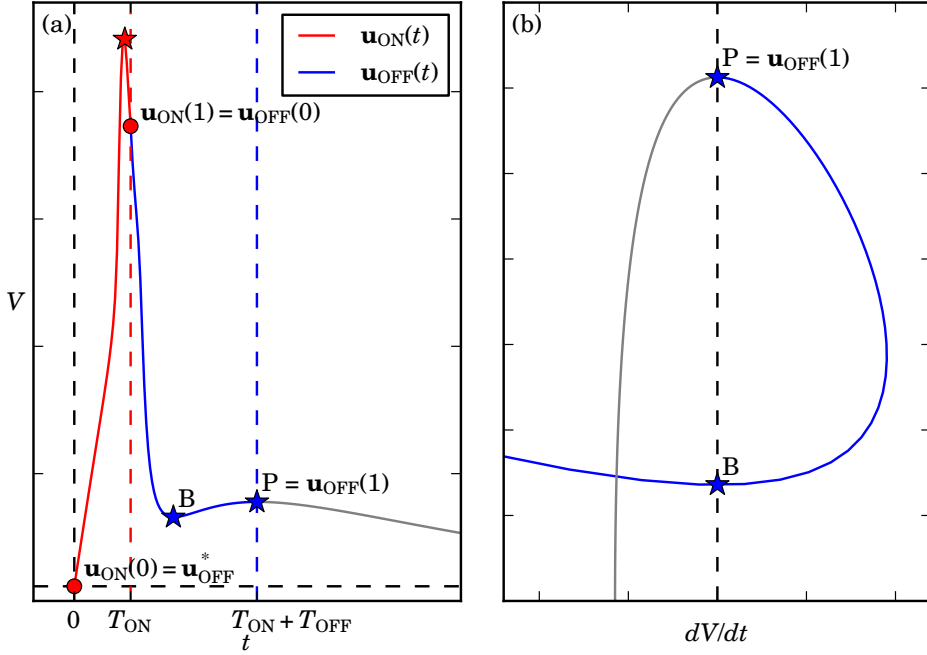


**Figure 5.1.** Illustration of the formulation of ADP in system (4.1) as a boundary value problem (4.5)–(4.8) with (5.1). Panel (a) shows orbit segments  $u_{ON}$  and  $u_{OFF}$  as time series of  $V$ . We assume that initially the system is at the resting potential  $u_{OFF}^*$ , which is an equilibrium of (4.1) with  $I_{app} = 0$  (indicated by the horizontal dashed black line). The first (red) segment is the (scaled) solution  $u_{ON}(t)$  of (4.1) with  $I_{app} = 20\mu\text{A}/\text{cm}^2$  and  $u_{ON}(0) = u_{OFF}^*$ ; the total integration time is  $T_{ON} = 3\text{ms}$ , such that one action potential occurs (its maximum is marked by a red star). Using the scaled Equation (4.5), this segment ends at  $u_{ON}(1)$ . The second (blue) segment is the (scaled) solution  $u_{OFF}(t)$  of (4.1) with  $I_{app} = 0$  and  $u_{OFF}(0) = u_{ON}(1)$ ; the total integration time  $T_{OFF}$  is such that  $u_{OFF}(t)$  exhibits a local minimum, which marks the beginning of ADP (blue star labelled B), and ends at a local maximum, marking the peak of ADP (blue star labelled P). Using the scaled Equation (4.6), this segment ends at  $u_{ON}(1) = P$  when the combined trajectory is integrated up to time  $T_{ON} + T_{OFF}$ . Panel (b) shows the ADP in  $(dV/dt, V)$ -projection; in this projection B and P are clearly associated with crossing the  $V$ -nullcline depicted as a dashed black line.

maximal conductances of  $I_{SI}$  and  $I_{FO}$ , because these parameters are important for shaping the ADP and bursting behaviours. To create the initial spike, we perturb our model from its resting potential with a brief current injection. Recall that for the system (4.1) the current injection is  $I_{app} = 20\mu\text{A}/\text{cm}^2$  and lasts for  $T_{ON} = 3\text{ms}$ , which is enough to create a fully-developed spike; we call this orbit segment  $u_{ON}$ . After 3ms the current is switched off, i.e.  $I_{app} = 0\mu\text{A}/\text{cm}^2$ , and a new orbit segment  $u_{OFF}$  starts to evolve from the initial conditions defined by the end of  $u_{ON}(T_{ON})$  back to its resting potential. The ADP and bursting takes place after the current has been switched off, hence, they are part of the orbit segment  $u_{OFF}$ .

Figure 5.1 shows the formulation of ADP in system (4.1) as a boundary value problem.

Orbit segments  $\mathbf{u}_{\text{ON}}$  and  $\mathbf{u}_{\text{OFF}}$  shown in Figure 5.1(a) are red and blue curves, respectively. Figure 5.1(b) shows the zoom of the ADP in the familiar  $(dV/dt, V)$ -projection, where we can clearly see that the orbit segment crosses the  $V$ -nullcline in the local extrema marked by the stars. The bottom and peak of ADP are marked with B and P, respectively. The orbit segment  $\mathbf{u}_{\text{OFF}}$  terminates at P, which yields total integration time of  $T_{\text{ON}} + T_{\text{OFF}}$ , that depends on the position of P. The grey line originating from P is the remaining part of the orbit segment  $\mathbf{u}_{\text{OFF}}$ , which is not used in our formulation.

The formulation of ADP as 2PBVP is similar to the one presented in Chapter 4, but it has a number of differences to the previously explained one. Therefore, for the clarity of presentation we explain all the elements of the formulation, some of which are identical to the one shown in Chapter 4. To overcome the problem of discontinuity at  $T_{\text{ON}}$ , i.e. when the current injection is switched off, we treat the orbit segments  $\mathbf{u}_{\text{ON}}$  and  $\mathbf{u}_{\text{OFF}}$  as two separate systems, coupled only by the boundary conditions. Namely, both  $\mathbf{u}_{\text{ON}}$  and  $\mathbf{u}_{\text{OFF}}$  are solutions of (4.1), but for different values of  $I_{\text{app}}$  and for different integration times  $T_{\text{ON}}$  and  $T_{\text{OFF}}$ , respectively. Therefore, the system that we solve has, in fact, double the dimensional of the original system, in our case ten dimensional. As in Chapter 4 we formulate a boundary value problem, such that  $\mathbf{u}_{\text{ON}}$  and  $\mathbf{u}_{\text{OFF}}$  are solutions of (4.5) and (4.6), that is,

$$\begin{aligned}\mathbf{u}'_{\text{ON}}(t) &= T_{\text{ON}} \mathbf{f}(\mathbf{u}_{\text{ON}}(t), \lambda, I_{\text{app}}), \\ \mathbf{u}'_{\text{OFF}}(t) &= T_{\text{OFF}} \mathbf{f}(\mathbf{u}_{\text{OFF}}(t), \lambda, 0).\end{aligned}$$

The difference with the approach taken in Chapter 4 is that we subject (4.5) and (4.6) to different boundary conditions. The first two boundary conditions are the same. As in Chapter 4, the boundary conditions for (4.5) are determined by the fact that the current injection perturbs system (4.1) from its resting potential for a fixed duration  $T_{\text{ON}}$  as indicated by the black and red (first two) vertical dashed lines in Figure 5.1(a). Hence, we impose the boundary condition (4.7), that is,  $\mathbf{u}_{\text{OFF}}^* = \mathbf{u}_{\text{ON}}(0)$  is solved implicitly as

$$\mathbf{f}(\mathbf{u}_{\text{ON}}(0), \lambda, 0) = 0.$$

just as in Chapter 4, and  $T_{\text{ON}} = 3 \text{ ms}$  is fixed. The orbit segment  $\mathbf{u}_{\text{OFF}}$  should again satisfy (4.8), that is,

$$\mathbf{u}_{\text{OFF}}(0) = \mathbf{u}_{\text{ON}}(1),$$

but we no longer keep  $T_{\text{OFF}}$  fixed. Instead, we require that  $T_{\text{OFF}}$  is such that  $\mathbf{u}_{\text{OFF}}(1)$  lies precisely at the point where  $\mathbf{u}_{\text{OFF}}$  has a local maximum in  $V$ . Hence,  $T_{\text{OFF}}$  is determined by the fact that  $dV/dt = 0$  at  $\mathbf{u}_{\text{OFF}}(1)$  as shown in Figure 5.1. Therefore, we add the boundary condition

$$f_1(\mathbf{u}_{\text{OFF}}(1), \lambda, 0) = 0, \quad (5.1)$$

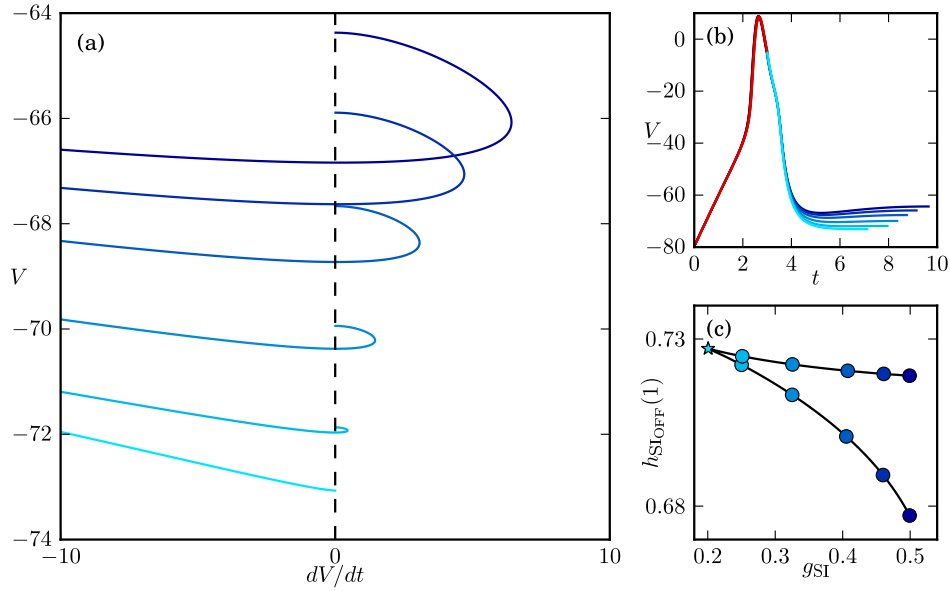


**Figure 5.2.** Continuation of system (4.5)–(4.8) with (5.1) in  $h_{\text{SI OFF}}(1)$ ; panel (a) shows an enlargement of the projection onto the  $(dV/dt, V)$ -plane to illustrate that the end points lie on the  $V$ -nullcline (vertical dashed black line); panel (b) shows the solutions along the bifurcation curve, shown in panel (c), as  $h_{\text{SI OFF}}(1)$  increases; panel (c) shows bifurcations diagram in the  $(g_{\text{SI}}, h_{\text{SI OFF}}(1))$ -plane, with the solutions marked with blue dots; the onset of ADP, which is a fold of the bifurcation curve, is the blue star.

which makes the 2PBVP (4.5)–(4.8) with (5.1) well posed.

As we know from Chapter 4, the behaviour of our model changes with  $g_{\text{SI}}$ ; namely, decreasing  $g_{\text{SI}}$  leads to disappearance of ADP. This means that the point P at the right boundary  $\mathbf{u}_{\text{OFF}}(1)$  of the orbit segment  $\mathbf{u}_{\text{OFF}}$ , varies substantially. In particular, the model has two slow variables  $h_{\text{SI}}$  and  $m_{\text{SO}}$  that are modulating the ADP duration and, consequently, burst termination. As  $V$  increases during the ADP,  $h_{\text{SI}}$  slowly decreases and inactivates  $I_{\text{SI}}$ , thus, lowers the value of  $dV/dt$ . On the other hand  $m_{\text{SO}}$  increases, which yields more  $I_{\text{SO}}$ , which, effectively, lowers the value of  $dV/dt$  as well. Hence, the orbit segment crosses the  $V$ -nullcline in P. Moreover,  $h_{\text{SI}}$  and  $m_{\text{SO}}$  have local extrema in P, namely, a local minimum and a local maximum, respectively; Since the change of  $h_{\text{SI}}$  in the low voltage region is more profound than  $m_{\text{SO}}$ , which is also slightly slower (see Table 4.1), we mostly focus on the local minimum of  $h_{\text{SI}}$  and monitor it at P, which we define as  $h_{\text{SI OFF}}(1)$ . Nonetheless, any of the two slow variables can be used.

In prominent ADP, as shown in Figure 5.1, points B and P are well separated. As the ADP decreases with a parameter change, the distance between B and P goes to zero, which corresponds to disappearance of the ADP. Therefore, the onset of ADP is an inclination point

in which B and P merge together. Continuation of orbit segments allows us to find this onset. We follow the solution shown in Figure 5.1 by continuation in the parameter  $h_{\text{SI}_{\text{OFF}}}(1)$ , but also allow  $g_{\text{SI}}$  to vary. The result of this continuation is shown in Figure 5.2. Figure 5.2(a) shows the last point of the solution  $\mathbf{u}_{\text{OFF}}$  for decreasing  $g_{\text{SI}}$  in  $(dV/dt, V)$ -space; the colour gradients represent the decrease of  $g_{\text{SI}}$  and, thus, the ADP. The associated time traces of the entire solution segments  $\mathbf{u}_{\text{ON}}$  and  $\mathbf{u}_{\text{OFF}}$  are shown in Figure 5.2(b). The relation between the free parameters  $g_{\text{SI}}$  and  $h_{\text{SI}_{\text{OFF}}}(1)$  is illustrated in Figure 5.2(c).

Indeed, as selected parameters change the distance between the point B and P decreases and the points, finally, merge together, as shown in Figure 5.2(a). The solution branch of the continuation grows in  $h_{\text{SI}_{\text{OFF}}}(1)$  as  $g_{\text{SI}}$  decreases. Note that the branch has a fold at  $g_{\text{SI}} \approx 0.2 \text{ mS/cm}^2$  indicating that there is a minimum value of  $g_{\text{SI}}$  below which ADP does not occur, which corresponds to fold bifurcation (Kuznetsov, 1998). This fold point marks the onset of ADP; it corresponds to the lowest curve in Figure 5.2(a). The solution curve has an upper branch, which consists of coexisting solutions of 2PBVP up to the first crossing of the nullcline, i.e., point B, shown in Figure 5.2(a). Note that at B our 2PBVP (4.5)–(4.8) with (5.1) is satisfied. The upper branch goes back in  $g_{\text{SI}}$  as well as in  $h_{\text{SI}_{\text{OFF}}}(1)$  after the fold. Hence, the fold exists in both  $g_{\text{SI}}$  and  $h_{\text{SI}_{\text{OFF}}}(1)$ , i.e., the solution branch has an extreme value for both  $g_{\text{SI}}$  (minimum) and  $h_{\text{SI}_{\text{OFF}}}(1)$  (maximum), as shown in Figure 5.2(a).

As mentioned above, the fold point that is detected during this continuation run corresponds to the onset of ADP. The set-up in AUTO (Doedel, 1981; Doedel and Oldeman, 2009) has the advantage that such folds can be detected automatically. Furthermore, each fold point can be continued in much the same way using a second parameter. Hence, our approach allows us to trace the onset of ADP as a curve in two parameters.

## 5.2 Identifying the onset of a spike in a transient burst

Since decreasing  $g_{\text{SI}}$  in Section 5.1 led to an onset of ADP at the minimum value  $g_{\text{SI}} \approx 0.2 \text{ mS/cm}^2$ , that is, a minimal value for which ADP can exist, we expect that increasing  $g_{\text{SI}}$  leads to the onset of a spike from the ADP. Note that the onset of a spike corresponds to a rise in the peak P of ADP until it reaches a critical threshold of the membrane potential  $V$  (Figure 5.1). In order to continue the onset of a next spike in a burst, we need a definition for threshold. Most classical studies of excitability perceive a threshold as a certain value of membrane potential (Hodgkin and Huxley, 1952; Izhikevich, 2006; Keener and Sneyd, 2009). Hence, the natural approach would be to monitor the value of  $V$  at the end point  $\mathbf{u}_{\text{OFF}}(1)$  in 2PBVP (4.5)–(4.8) with (5.1) and define the onset of a burst as the point where  $g_{\text{SI}}$  is such that  $\mathbf{u}_{\text{OFF}}(1)$  has reached the critical threshold of the membrane potential. However, then one

would have to guess what the value of the critical threshold actually is and make heuristic assumptions, for example, that the critical threshold does not depend on  $g_{\text{SI}}$ . Since obtaining a precise definition of threshold is still an open problem, we propose a different approach that approximates the onset of a spike and, thus, corresponds to a dynamic bursting threshold. In order to do that, we investigate the behaviour of the slow variables during the spike-adding transition. To this end, we first investigate the mechanism of spike generation by considering the continuation of longer orbit segments that extend past the local maximum P of ADP.

Figure 5.3 shows a continuation run starting from  $g_{\text{SI}} = 0.5 \text{ mS/cm}^2$  using system (4.5)–(4.8). Instead of imposing boundary condition (5.1) we fix  $T_{\text{OFF}} = 297 \text{ ms}$ , thus the total duration of the orbit segment time series is  $T_{\text{ON}} + T_{\text{OFF}} = 300 \text{ ms}$ , so that  $\mathbf{u}_{\text{OFF}}(1)$  lies (approximately) at the resting potential. As before, Figure 5.3(a) shows the solution branch using the standard  $L^2$ -norm of AUTO (Doedel, 1981; Doedel and Oldeman, 2009) as a measure, which reflects the changes in the shape of the orbit segment; the value of the  $L^2$ -norm is not important in this case, it is used for illustration purposes. We observe that the solution norm is fairly constant over a relatively large  $g_{\text{SI}}$ -interval, which is followed by a sharp downward peak, in which the parameter variation is only  $\mathcal{O}(10^{-7})$ , before establishing the next ‘plateau’. The constant plateaus in Figure 5.3(a) correspond to the increase in ADP, whereas, the downward peaks indicate the spike-adding transitions, which happen in very small parameter range. The orbit segments of selected solutions along the branch are shown in Figures 5.3(b)–(f) and illustrate that the ‘plateaus’ correspond to solutions with (increasing) fixed numbers of action potentials, while solutions from the peaks exhibit a slowly rising double-step ADP that is quite different from a typical ADP as shown in Figure 4.1. Such sharp peaks of the branch in Figure 5.3(a) are characteristic for spike-adding transitions studied in three-dimensional systems (Terman, 1991; Tsaneva-Atanasova et al., 2010).

Figure 5.3(b) shows the original one spike with ADP, which grows along the first plateau. As  $g_{\text{SI}}$  increases the solution enters the first downward peak where the ADP becomes elongated as shown in Figure 5.3(c). Beyond the bottom of a downward peak development of the second step of this transient ADP begins (Figure 5.3(d)). In fact, the double-step ADP shown in Figure 5.3(d) is the longest one; from this point onwards, the transient ADP retracts back with a new spike as shown in Figure 5.3(e). As the solution reaches the next plateau it has two well-developed spikes as shown in Figure 5.3(f). Figures 5.3(g)–(h) indicate that the process repeats for the subsequent spikes.

We note, that the spike-adding transition takes place for  $\mathcal{O}(10^{-7})$  parameter variation as shown in Figures 5.3. Therefore, in a model simulation, the appearance of a new spike seems to be a practically instantaneous process, with all the details of the transition practically unobservable. The double-step ADP is, in fact, a canard-like transition along the unstable sheets of the critical manifold, which we discussed in Chapter 4.

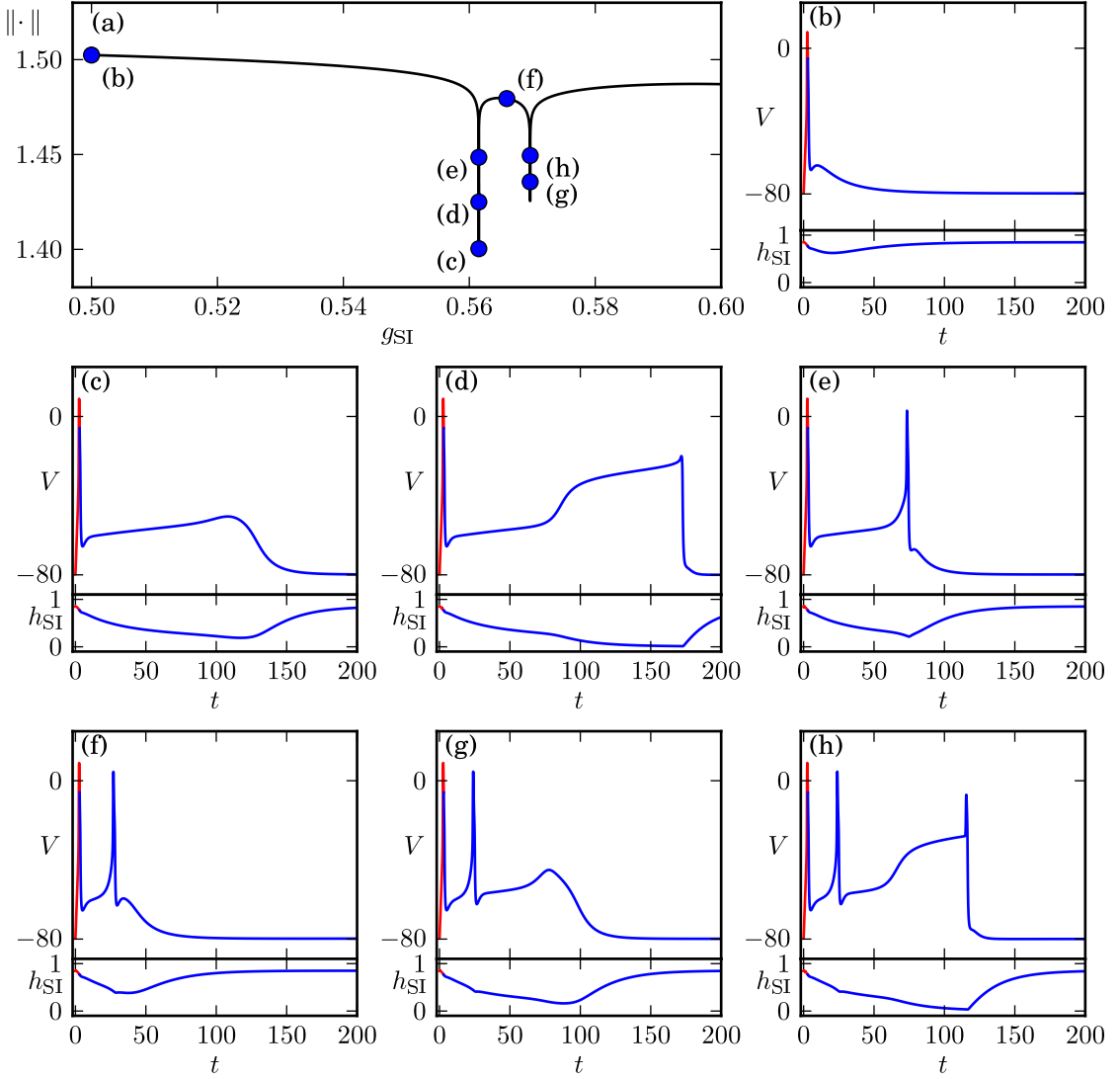


**Figure 5.3.** Continuation for increasing  $g_{\text{SI}}$  of solutions to system (4.5)–(4.8) with  $T_{\text{OFF}} = 297$  ms fixed; panel (a) shows the AUTO (Doedel, 1981; Doedel and Oldeman, 2009)  $L^2$ -norm of the solution branch versus  $g_{\text{SI}}$  and illustrates that the spike-adding mechanism happens suddenly via a pronounced drop in norm; panels (b)–(f) show representative solutions along the branch, indicated by the correspondingly labelled dots in panel (a), and illustrate that solutions during a spike generation exhibit a long plateau before relaxing back to the resting potential; the time trace below  $V$  is the corresponding trace of  $h_{\text{SI}}$ , which has a minimal value that corresponds with the peak of ADP.

The duration of the transient behaviour before relaxation back to the resting potential is substantially longer for the solutions that lie along the peaks of the solution branch, that is, during a spike generation. The natural solution would seem to be finding the orbit segment with maximal time  $T_{\text{OFF}}$  at the peak of ADP. This approach can, however, cause numerical

problems, because  $T_{\text{OFF}}$  is unbounded. Namely, the orbit segment evolution in the state space can be very slow in some cases, thus, the maximal  $T_{\text{OFF}}$  could be very large. On the other hand, this much longer duration of the depolarised state allows  $I_{\text{SI}}$  to inactivate nearly completely. The corresponding plots of inactivation of the slow inward current are  $h_{\text{SI}}$  shown below the time trace of membrane potential in Figures 5.3(b)–(h). As the transition progresses, the value of  $h_{\text{SI}}$  at the peak of the double-step ADP reaches a minimal value when the transient ADP reaches its maximal length. Moreover,  $h_{\text{SI}}$  is biophysically restricted to the interval  $[0, 1]$ . Since we can monitor and detect such long double-step ADP through a minimal value of  $h_{\text{SI}}$ , we can treat it as threshold for spike adding. To find this onset numerically, we use the previously formulated 2PBVP to detect the longest orbit segment  $\mathbf{u}_{\text{OFF}}(t)$ .

Consequently, in order to detect the onset of a spike we use an optimization approach to obtain the local extrema of  $h_{\text{SI}_{\text{OFF}}}$  in the peak of ADP, which we previously defined as  $h_{\text{SI}_{\text{OFF}}}(1)$ . The extrema of  $h_{\text{SI}_{\text{OFF}}}(1)$  are detected as folds using our 2PBVP formulation in AUTO (Doedel, 1981; Doedel and Oldeman, 2009). The extremum in our 2PBVP formulation corresponds to a fold bifurcation (Kuznetsov, 1998), but in our case there are no equilibria; we only consider existence of the solution of 2PBVP. Namely, as  $h_{\text{SI}_{\text{OFF}}}(1)$  decreases it reaches a point where  $\mathbf{u}_{\text{OFF}}$  has a maximal length as shown in Figures 5.3(d) and then  $\mathbf{u}_{\text{OFF}}$  retracts as shown in Figures 5.3(e), which corresponds to an increase in  $h_{\text{SI}_{\text{OFF}}}(1)$ . Hence, the extremum in our 2PBVP is reminiscent of a fold bifurcation (Kuznetsov, 1998). We note that in the case of a spike-adding transition, the fold marking the onset of a spike exists only in the slow variables, in our case  $h_{\text{SI}_{\text{OFF}}}(1)$  but not for  $g_{\text{SI}}$ , as was the case for the onset of ADP. Hence, the onset of a spike is not connected to an actual bifurcation point, but only occurs as a continuous deformation of the orbit segment. Therefore, to detect the onset of a spike,  $h_{\text{SI}_{\text{OFF}}}(1)$ , or an other related parameter monitoring a slow variable, has to be a principal continuation parameter. Note that  $T_{\text{OFF}}$  still remains a free parameter but it is not a principal continuation parameter.

Figure 5.4 shows the outcome of a continuation of the orbit segment. The time traces of  $\mathbf{u}_{\text{ON}}$  and  $\mathbf{u}_{\text{OFF}}$  are shown in Figure 5.4(a) using the same colour scheme as in Figure 5.2. Figure 5.4(b) shows the relation between  $h_{\text{SI}_{\text{OFF}}}(1)$  and  $g_{\text{SI}}$  during the continuation. The value of the membrane potential in the peak of ADP,  $V_{\text{OFF}}(1)$ , as a function of  $h_{\text{SI}_{\text{OFF}}}(1)$  is shown in Figure 5.4(c) to illustrate that the extrema of  $h_{\text{SI}_{\text{OFF}}}(1)$  are, in fact, the folds of a bifurcation curve. The folds are marked with blue-gradient stars in Figures 5.4(b)–(c); the corresponding time traces in Figure 5.4(a) are marked with a thick line. Example solutions along the continuation branch are shown in Figure 5.4(a) and correspond to the values labelled in Figures 5.4(b)–(c) with blue-gradient dots.

As expected, the orbit segment  $\mathbf{u}_{\text{OFF}}(t)$  length increases with  $h_{\text{SI}_{\text{OFF}}}(1)$  and develops a double-step ADP as indicated in Figure 5.4(a). Note that, as before, the orbit segment  $\mathbf{u}_{\text{OFF}}$  terminates at the peak of ADP, thus, it is truncated in Figure 5.4(a). As the system continues

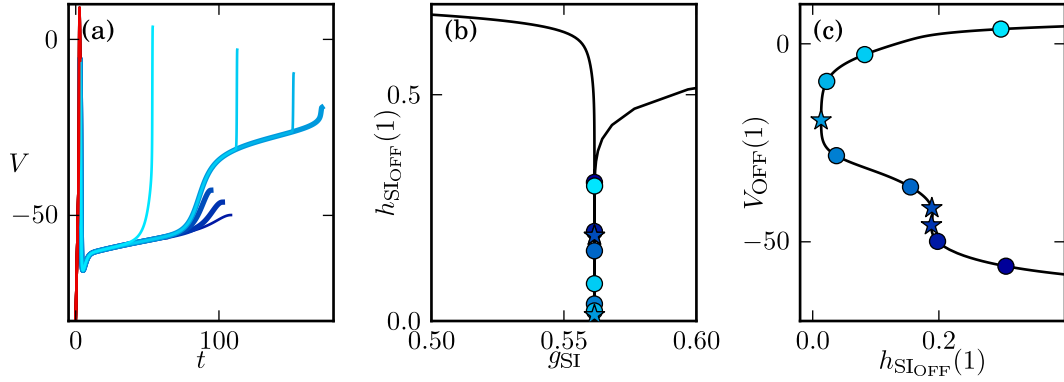


**Figure 5.4.** Continuation to find extrema of  $h_{SI_{OFF}}(1)$ ; panel (a) shows the time series of the solutions; thick lines curves correspond to the extrema of  $h_{SI_{OFF}}(1)$ ; panel (b) and (c) show  $h_{SI_{OFF}}(1)$  versus  $g_{SI}$  and  $h_{SI_{OFF}}(1)$  versus  $V_{OFF}(1)$ , respectively; consequent solutions of the continuation are marked with dots (regular solutions) and stars (extrema of  $h_{SI_{OFF}}(1)$ ).

beyond the last fold the orbit segment  $\mathbf{u}_{OFF}$  retracts with a newly created spike. Figure 5.4(b) corresponds to Figure 5.3(a) and indicates that continuation of  $h_{SI_{OFF}}(1)$  yields the increase of  $g_{SI}$ . Moreover, the characteristic downward peak is clearly visible in this projection, hence, the transition takes place in a very small parameter range. Figure 5.4(c) clearly indicates that the extreme points of  $h_{SI_{OFF}}(1)$  are folds of the bifurcation diagram. Furthermore, comparison of Figure 5.4(b) and (c) shows that the extrema exist only for the slow variable  $h_{SI_{OFF}}(1)$  but not for  $g_{SI}$ , which increases. Note that  $V_{OFF}(1)$  in Figure 5.4(c) also increases, which indicates that the peak of ADP becomes a peak of a newly created spike as shown in Figure 5.4(a). Interestingly, apart from the expected minimum of  $h_{SI_{OFF}}(1)$  corresponding to the longest double-step ADP solution, we encountered a local minimum closely followed by a local maximum as shown in Figures 5.4(b)-(c). This result suggests that the orbit segment retracts slightly during the transition from the first to the second step of ADP.

We have established that the minimum of  $h_{SI_{OFF}}(1)$  approximates the onset of a spike. As before, this onset has been detected automatically in AUTO (Doedel, 1981; Doedel and Oldeman, 2009) as a fold using our continuation method. Again, this allows us to trace the onset of a spike as a curve in two parameters without any major modifications to the formulation.

### 5.3 Establishing the regions of model behaviour

Above, we identified and calculated the onset of ADP and a spike while varying  $h_{SI_{OFF}}(1)$ . and, thus,  $g_{SI}$ . Since these onsets are detected in AUTO (Doedel, 1981; Doedel and Oldeman, 2009) as folds, we can use two-parameter fold continuation to find curves in a two-parameter plane

that mark the transition between different bursting behaviours of the model. As our second parameter we choose the maximal conductance  $g_{FO}$  because our previous study in Chapter 4 shows, that, along with  $g_{SI}$ , it is a very important parameter shaping the behaviour of the model. Namely,  $I_{FO}$  is a strongest inward current that is responsible for the membrane potential return to resting state after a spike. Moreover, the magnitude of  $g_{FO}$  influences the amplitude of ADP and, thus, the overall excitability.

In order to continue the onset of ADP in the  $(g_{FO}, g_{SI})$ -plane, we start the continuation by selecting a fold point that was detected using one-parameter continuation. The main change is that our list of free parameters is extended by  $g_{FO}$ ; all other previously defined free parameters remain unchanged. Similar fold continuations are used to follow the onset of a spike in consecutive bursts. We need to start from a different fold point for each burst boundary that we want to establish. Namely, we perform the continuation procedure illustrated in Figure 5.4 for values of  $g_{SI}$  relatively close to every downward peak in Figure 5.3(a). All the extrema of  $h_{SI^{OFF}}(1)$  for the onset of the next spike are detected as folds (Figure 5.4).

Figure 5.5 shows the regions of behaviour of our simplified model established by a two-parameter continuation of orbit segments. The boundaries between the different regions of behaviour in the  $(g_{FO}, g_{SI})$ -plane are shown as solid lines in Figure 5.5(a). The continuation of the onset of ADP is depicted with a solid green line in Figure 5.5(a). Similarly, the continuation of the onset of the two- to eight-spike bursts are shown in Figure 5.5(a) as solid blue-to-cyan gradient lines for increasing numbers of spikes in a burst, respectively. Simulations for the different values of  $g_{FO}$  and  $g_{SI}$ , labelled in Figure 5.5(a) with blue dots, are presented as time traces in Figures 5.5(b)–(m).

From a physiological point of view all the maximal conductances, including  $g_{FO}$  and  $g_{SI}$ , should be positive. Therefore, only the positive part of  $(g_{FO}, g_{SI})$ -plane is taken into account in the computations of the boundaries shown in Figure 5.5(a). The region of interest is bounded from above by a Hopf bifurcation of the full system (4.1) shown as green dashed curve, that marks the beginning of a regular periodic attractor. Short-current injection pushes the system into the basin of attraction of the periodic attractor, which causes the system to enter into a continuous (tonic) spiking state. Thus, the transient burst that we analyse cease to exist. Hence, in our analysis we consider the Hopf-bifurcation curve as an upper bound for the bursting region.

As illustrated in Figures 5.5(b) and (c), the regions where the model system exhibits one spike with ADP are, indeed, bounded by the computed boundary. For fixed value of  $g_{FO}$ , the model enters the bursting regions as  $g_{SI}$  increases; Figures 5.5(d)–(g) show a typical simulations with parameters values corresponding to the blue dots in Figure 5.5(a). As predicted, the number of spikes in a burst increases with  $g_{SI}$ . The accuracy of the method is illustrated by the region with two spikes in a burst, as shown in Figure 5.5(d). Despite the region being very

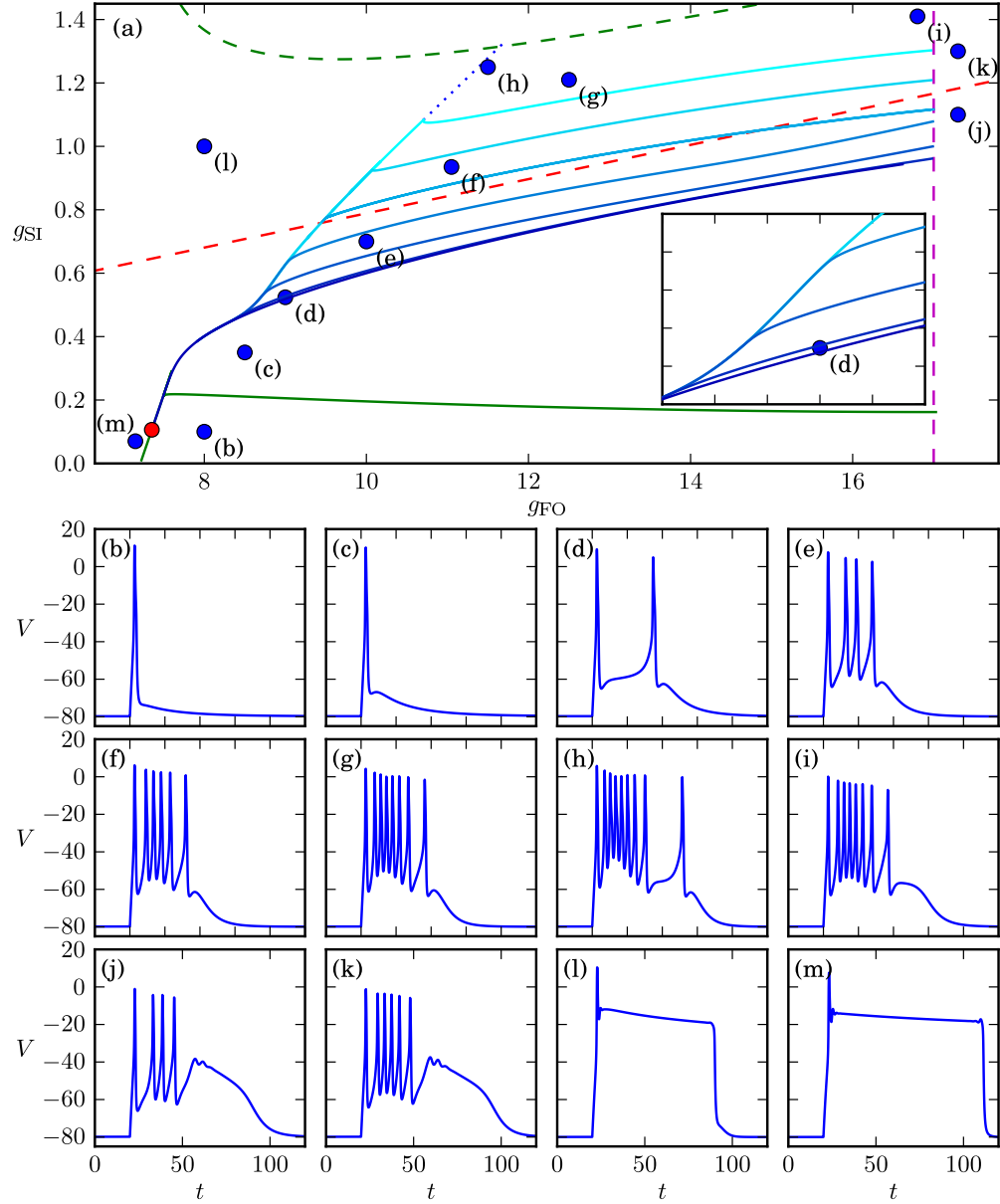


**Figure 5.5.** Regions of a different model behaviour established by a two-parameter continuation of an orbit segment; panel (a) shows the boundary curves in the  $(g_{\text{FO}}, g_{\text{SI}})$ -plane, computed as a well-posed 2PBVP in AUTO (Doedel and Oldeman, 2009), depicted with green and blue-gradient lines for the boundaries of ADP and consequent burst, respectively; the details of the two-spike burst region are shown in the inset axes; two-parameter continuation of fold and Hopf bifurcation of the full system (4.1) is depicted with red and green dashed lines, respectively; the right boundary of the continuation is shown with the rightmost dashed magenta line; the red dot marks the point where the continuation of the boundary of burst terminates; panels (b)–(m) show simulated responses of the simplified ADP model with the  $g_{\text{FO}}$  and  $g_{\text{SI}}$  values marked with the dots in panel (a).

small, our method is able to successfully establish this boundary, which would be very difficult to detect using brute-force simulations.

As shown in Chapter 4, an additional spike-adding mechanism appears when unstable equilibria of the full system coexists with the single stable equilibrium, i.e., the resting potential. In this case the spike is created in a discontinuous way as the orbit segment hits the unstable equilibrium, which is stable in the slow subsystem. In our system, the main feature of such a transition is that the spike is generated from a long single-step ADP, not a double-step ADP. Nonetheless, this transition is also associated with a minimum of a slow variable, i.e.  $h_{\text{SI}_{\text{OFF}}}(1)$  in our case. Therefore, the procedure of detecting the onset of a spike does not change. The fold line marking the appearance of two unstable equilibria of the full system is shown in Figure 5.5(a) as a dashed red line; beyond this line the spike-adding mechanism becomes discontinuous. Nevertheless, our method is able to detect the boundary, again, as a minimum in  $h_{\text{SI}_{\text{OFF}}}(1)$ . The behaviour of the system inside the regions, below and above the (red) fold line, is identical, at least to numerical precision. It is because only the spike-adding mechanism changes but the overall bursting mechanism remains qualitatively the same.

The burst-boundary curves terminate in the area marked with a red dot, while the curve marking the boundary of ADP continues further and closes the region. The boundaries are the minimum of  $h_{\text{SI}_{\text{OFF}}}(1)$ , which is very close to zero, as shown in Figures 5.4(b) and (c). As the boundary curve is being evaluated,  $h_{\text{SI}_{\text{OFF}}}(1)$  goes to zero with the decrease of  $g_{\text{FO}}$  and  $g_{\text{SI}}$ . It is because the ADP during the transition becomes even longer in that region of the  $(g_{\text{FO}}, g_{\text{SI}})$ -plane. The red dot in Figure 5.5(a) marks the place where  $h_{\text{SI}_{\text{OFF}}}(1)$  actually becomes zero. Beyond that point  $h_{\text{SI}_{\text{OFF}}}(1)$  would have to go into the negative region to continue the boundary, but it is constrained by the Boltzmann (in)activation function (4.4) to the biological range of  $[0, 1]$ . This constraint makes it impossible to continue the boundary beyond this point, thus, all boundaries of the onset of a spike terminate here. On the other hand, the onset of ADP takes place for much higher values of  $h_{\text{SI}_{\text{OFF}}}(1)$ . Moreover, this curve lies very close to the other boundary curves, thus, it approximates the position of the other curves. Hence, the curve marking the onset of ADP is able to close the region as shown in Figure 5.5(a). As indicated by a simulation shown in Figure 5.5(m), the boundary of the region is estimated well.

As the number of spikes increase, the complexity of the numerical continuation process also increases. We were able to obtain a meaningful numerical result up to the boundary marking the transition between seven and eight spikes in a burst as shown in Figure 5.5(a). There is a characteristic feature of the the boundary curves, namely, they join together creating a left boundary, which is a relatively regular line. Therefore, we use the slope of this line to extrapolate the left boundary of the regions as depicted in Figure 5.5(a) with a blue dotted line. Indeed, the model simulation in Figure 5.5(h), very close to the extrapolated boundary, indicates that the boundary estimation holds and is relatively precise. Moreover, the burst shown in Figure 5.5(h) has nine spikes, which indicates, that there exist at least one additional

boundary before the Hopf curve. Therefore, the estimated region consists of a bursts with eight or more spikes.

As shown in Figure 5.5(a) all the burst-boundary curves seem to merge together on the left and continue downwards in  $g_{SI}$ . In fact, these curves do not merge; they are separate solutions with different number of spikes that just lie very close to each other in the  $(g_{FO}, g_{SI})$ -plane. Beyond this boundary the spikes in the burst become a depolarised plateau with an infinite number of spikes that have extremely small amplitudes as shown in Figures 5.5(l) and (m). This state corresponds to a slow passage through the Hopf bifurcation that exists in the fast subsystem; see (Ermentrout and Terman, 2010; Izhikevich, 2006; Rinzel, 1987) for more details on this process. Note that this behaviour is also transient and the orbit segment eventually returns to the stable equilibrium, i.e., resting membrane potential as illustrated in Figures 5.5(l) and (m). The behaviour is not influenced by the unstable equilibria of the full system, as the responses in Figures 5.5(l) and (m) are qualitatively the same.

Our study shows that for  $g_{FO} > 17$  the burst response develops a plateau-like ADP with a number of oscillations (ripples) as shown in Figures 5.5(j) and (k), which is different from the normal response shown in Figures 5.5(b)–(i). This behaviour is related to a change of the time scale of  $V$ . The time constant of the membrane potential in the model can be approximated by the time constant of a capacitor, namely,  $\tau_V = C_m/g$ . The reference conductance  $g$  is assumed to be the largest conductance in the system, in our case it would be  $g = g_{FO}$ . Clearly, the increase of  $g_{FO}$ , decreases  $\tau_V$  and, thus, makes  $V$  faster. On the other hand the time scales of the other variables remain constant, thus, as  $\tau_V$  increases the time-scale separation between the other slow variables in the system. For a high value of  $g_{FO}$ , such as  $g_{FO} = 17$ ,  $\tau_V$  changes from  $\mathcal{O}(0.1)$ , for  $g_{FO} = 9.5$ , to  $\mathcal{O}(0.05)$ . Hence, the time-scale separation between  $V$  and the other fast variables,  $m_{SI}$  and  $m_{FO}$ , becomes about two-times larger. Thus, the system has now one fast, two slow and two very slow variables, which would require further investigation in relation to those time scales. Here we limit the continuation to  $g_{FO} = 17$ , which is depicted with a vertical dashed magenta line in Figure 5.5(a). The simulation in Figure 5.5(i) shows that the example burst on the left from the boundary is normal. On the other hand, the simulations shown in Figures 5.5(j) and (k) have ripples on top of ADP and this indicates that the boundary is estimated well.

Having established the regions of different model behaviour, we now focus on the meaning of the form of those regions, that reflects the sensitivity of the model to a change of parameter. Figure 5.5(a) indicates that the region with just one spike and the ADP is the largest one. It agrees with experimental recordings indicating that the response with just one spike followed by an ADP is the most robust (Brown and Randall, 2009). Also, the region with no ADP after the first spike is relatively large, which is in line with the experimental results reported in (Brown and Randall, 2009; Golomb et al., 2006; Yaari et al., 2007). Furthermore, experimental findings suggest that the response of the neuron is more likely to have more than two spikes

in a burst (Brown and Randall, 2009; Golomb et al., 2006; Yaari et al., 2007). Indeed, our continuation results show that the region of two-spike burst is the smallest one. As shown in Figure 5.5(a), the regions of burst with multiple spikes are itself relatively small, but the combined region of bursting behaviour is comparable in size to the region without bursting. Moreover, the results presented in Figure 5.5 indicate that changes of  $g_{SI}$  have a much larger effect on the bursting behaviour than the changes of  $g_{FO}$ . Hence, low-voltage activated slow inward currents seem to have a larger impact on the excitability in our model. Furthermore, our analysis shows that there exists a large area with a highly depolarised state as shown in Figures 5.5(l) and (m); similar behaviour was observed experimentally (Golomb et al., 2006) when  $K^+$ -channel blocker Linopirdine has been applied. Such a prolonged depolarised state is, potentially, very dangerous for the cell. Namely, all the ionic channels are away from their resting state and the ionic balance of the cell is being perturbed rapidly. Potentially, the influx of  $Ca^{2+}$  that may occur in this case can reach toxic levels and, as a result, trigger cell death. This region is relatively large and it directly borders with a physiological burst. Therefore, it suggests that hyper excitable cells (that fire many spikes) could be very easily pushed into this potentially dangerous state. On the other hand, the increase of  $g_{FO}$ , which would seem to be less dangerous as it decreases excitability, leads to a prominent ADP with small oscillations, as shown in Figures 5.5(j) and (k). Such a prolonged ADP can have a similar effect on the influx of  $Ca^{2+}$ . Hence, this behaviour is also potentially dangerous for the cell. Moreover, the oscillations can lead to creation of different behaviours, not considered in this study.

## 5.4 Conclusion

In this chapter we performed a continuation-based numerical analysis for the detection of the onset of ADP as well as a spike in a transient burst. Our 2PBVP formulation mirrors the stimulation protocols used in electrophysiological experimental studies. Hence, analysis of a model can be directly related to the experimental results, without the use of any complex measures or relations. We have shown that onset of ADP and a spike is an extremum of a slow variable of the model. Moreover, the onset of a spike detected with our method is closely related to a spiking threshold. Our 2PBVP formulation detect the onsets of ADP and a spike as folds, that can be continued in two-parameters to establish the regions of different model behaviour. Identification of such regions corresponds to a parameter sensitivity analysis of a model. Our analysis indicates that the area of normal physiological behaviour borders an area of potentially dangerous behaviour characterised by long depolarised plateau responses. Furthermore, it appears that  $I_{FO}$  is an important current for shaping spiking but it does not influence the bursting duration or number of spikes that much. On the other hand, an increase of  $g_{FO}$  results in a prolonged ADP with oscillations, which could also be dangerous for a cell.

# Chapter 6

## Conclusion and outlook

### 6.1 Summary

In this thesis we used tools provided by dynamical systems theory and analysed transient behaviour of neural cells. In particular, we took advantage of the natural time-scale separation, that typically occurs in models written in Hodgkin-Huxley formalism, and applied concepts of geometrical singular perturbation theory to analyse these models. Moreover, the study in this thesis was focused on physiologically-realistic models of neural cells, which were developed in close collaboration with experimentalists using data from electrophysiological studies. Such realistic models are usually relatively high dimensional and their variables often evolve on multiple time-scales. Our study showed how the known theory can be applied to such high-dimensional models.

In Chapter 2 we analysed after-depolarisation, which is a hallmark of excitability and a precursor of transient bursting. We formulated a model of hippocampal pyramidal neurons of areas CA1 and CA3, based on recent experimental data, that focussed on the transient aspects of the behaviour of those cells. We showed the contribution of particular types of ionic currents to transient excitability, which is related to the natural time-scale separation of the gating variables of ionic currents. Moreover, we used nullcline analysis to define ADP mathematically, and illustrate how this definition can be applied to both the model and experimental data.

We applied the ideas of GSPT and extend them to analyse the periodic bursting in a pituitary cell model. In Chapter 3 we calculated the critical manifold using bifurcation analysis of the fast subsystem with one slow variable as a parameter. We used nullcline analysis to study the nature of plateau bursting taking place below the branch of attracting equilibria. Moreover, using continuation of orbit segments we computed the family of stable manifolds arising from a branch of saddle equilibria, which plays the role of separatrix in this system. We showed that termination of the burst occurs as soon as the orbit crosses the stable manifold. The crossing

happens at different stages of the burst, depending on the values of the parameters modulating the duration of the active phase.

We return to the model of CA1/3 pyramidal neurons and analyse the spike-adding mechanism in transient burst using the tools provided by GSPT. Based on the essence of ADP and bursting, that we characterised in Chapter 2, we reduced the model of this phenomenon to a five-dimensional model. Here, we focussed on the spike-adding mechanism in a transient burst that originates from the ADP. To understand the spike adding we performed a continuation of solutions of orbit segments as solutions of the model formulated as a two-point boundary value problem. By overlying these orbit segments on the critical manifold of the fast subsystem parametrised by two slow variables, we showed that spikes are added through a canard-like transition. That is, during the spike-adding transition, the associated orbit segments trace the unstable sheets of the critical manifold up to a regular fold point, after which the fast flow takes over and the behaviour is organised by a family of attracting periodic orbits. Our results suggest at least two mechanisms of spike adding, through a fold of critical manifold and unstable equilibrium of the full system. For a different parameter regime, we found that the spikes can also be added via heteroclinic connection with the saddle equilibria of the full system, when they are present. In contrast to periodic bursting, spike adding in a transient burst does not occur through any bifurcations. We showed that spikes are added through a continuous deformation of the trajectory and not in an abrupt discontinuous transformation.

The analysis of ADP and spike adding enabled us to formulate and compute the onsets of ADP and a spike using orbit segment continuation. In Chapter 5 we have shown that those onsets correspond to extrema of slow variables of the system. The onsets in our formulation are detected as folds, which allows us to establish the boundaries of different model behaviour. This new technique is a form of parameter sensitivity analysis and our formulation in terms of a two-point boundary value problem is general, so that it can be applied to the study of other models.

## 6.2 Future work

In the model presented in Chapter 2 we did not consider  $\text{Ca}^{2+}$ -dynamics due to the focus on quite fast phenomena. Nonetheless, a prominent transient burst can cause a substantial influx of  $\text{Ca}^{2+}$ , which is expected to influence the excitability of the cell. Directions of future work include considering  $\text{Ca}^{2+}$ -dynamics and  $\text{Ca}^{2+}$ -activated currents, which are known to be present in pyramidal cells. This would also account for spike frequency adaptation, that is common in CA3 pyramidal neurons but not present in our model because of the simplification.

Furthermore, in Chapter 2 we have deduced a time-scale separation between the gating variables of inward and outward currents necessary for the existence of the ADP. This prediction could be studied experimentally in more detail. Namely, it is almost impossible to control

the time scales of the ionic currents using pharmacological tools, but modern experimental techniques, such as dynamic clamp, allow us to study more detailed features. Dynamic clamp is a form of current clamp and uses computer equipment to model ionic currents and feed them back to the cell. This allows for the easy manipulation of the current parameters and, thus, introduces a better control into experiment. Hence, dynamic clamp could enable a direct investigation of the time-scale separation present in neural cells and can be used to test predictions of our model.

In our BVP formulation we used a simple short constant-current injection. However, in electrophysiology it is natural to test the cell with currents of different amplitudes and durations, which can be easily done using our method. Moreover, other forms of current stimulation, such as excitatory postsynaptic potential or theta burst stimulation are commonly used in experiments. Our method can be extended to incorporate more complex experimental protocols.

Another natural future extension of this work would be the application of our method to other excitable models. In particular, our main fast outward current is persistent for the sake of the simplification. Using a transient current, which is a more typical main outward current in neural models, could produce interesting new results. Furthermore, our study of the spike-adding mechanism in a transient burst presented in Chapter 4 unveiled the importance of slow flow on the critical manifold. Different models of transient bursts can, potentially, give rise to different dynamics of the slow flow such as the presence of different folded singularities which could bring new possibilities of spike-adding mechanisms.

In Chapter 5 we have shown that onsets of ADP and a spike are related to extrema of slow variable. Our study in Chapter 4 suggests that the canard-like behaviour, and the occurrence of extrema of the slow variables can be relatively typical for spike adding. Since we studied only one model of a transient burst, future analysis of different spike-adding mechanisms could test how often the extrema of slow variables are involved in the spike-adding transition.



## Appendix A

### Summary of pituitary cell model equations

In this appendix we provide the complete details of the model (3.1)–(3.3) for somatotroph cell. The functional dependencies are discussed below, and the values of the parameters used for the model are given in Table A.1.

Equation (3.1),

$$\frac{dV_m}{dt} = -\frac{1}{C_m} I_{\text{ionic}}(V_m, n_{dr}, c),$$

is a capacitance model of  $V_m$ , where  $C_m$  stands for the membrane capacitance and  $I_{\text{ionic}}$  is the sum of ionic currents

$$\begin{aligned} I_{\text{ionic}} = & I_{\text{Ca}_L}(V_m) + I_{\text{Ca}_T}(V_m) + I_{K_{dr}}(V_m, n_{dr}) + I_{K_{ir}}(V_m) \\ & + I_{\text{NS,Na}}(V_m) + I_{\text{BK}_{\text{NEAR}}}(V_m) + I_{\text{BK}_{\text{FAR}}}(V_m, c). \end{aligned}$$

Here,  $I_{\text{Ca}_L}$  and  $I_{\text{Ca}_T}$  are L- and T-type voltage-sensitive  $\text{Ca}^{2+}$ -currents of the form

$$\begin{aligned} I_{\text{Ca}_L}(V_m) &= g_{\text{Ca}_L} m_{\text{Ca}_{L\infty}}^2(V_m)(V_m - V_{\text{Ca}}), \\ I_{\text{Ca}_T}(V_m) &= g_{\text{Ca}_T} m_{\text{Ca}_{T\infty}}^2(V_m) h_{\text{Ca}_{T\infty}}(V_m)(V_m - V_{\text{Ca}}). \end{aligned}$$

The corresponding activation and inactivation functions are given by

$$\begin{aligned} m_{\text{Ca}_{L\infty}}(V_m) &= \frac{1}{1 + \exp\left(\frac{-(V_m - V_{m_L})}{k_{m_L}}\right)}, \\ m_{\text{Ca}_{T\infty}}(V_m) &= \frac{1}{1 + \exp\left(\frac{-(V_m - V_{m_T})}{k_{m_T}}\right)} \text{ and} \\ h_{\text{Ca}_{T\infty}}(V_m) &= \frac{1}{1 + \exp\left(\frac{V_m - V_{h_T}}{k_{h_T}}\right)}. \end{aligned}$$

**Table A.1.** Parameter values used in the simulations.

Parameter	Value	Parameter	Value
$g_{Ca_L}$	0.74 nS	$k_{m_T}$	8 mV
$g_{Ca_T}$	0.105 nS	$V_{h_T}$	-56 mV
$g_{K_{dr}}$	3.85 nS	$k_{h_T}$	5 mV
$g_{K_{ir}}$	15.75 nS	$V_{n_{dr}}$	0 mV
$g_{BK_{NEAR}}$	0.55 nS	$k_{n_{dr}}$	8 mV
$g_{BK_{FAR}}$	10 nS	$k_{BK}$	10 mV
$g_{NS,Na}$	0.1245 nS	$V_{BK_0}$	0.1 mV
$V_{Ca}$	60 mV	$k_{shift}$	18
$V_K$	-80 mV	$k_{Ca_{bk}}$	1.5 $\mu M$
$V_{K_{ir}}$	-83 mV	$A$	0.11
$V_{NS,Na}$	-20 mV	$f$	0.0098
$\sigma_N$	0.002 pA	$p_{ER}$	0.00015 s <sup>-1</sup>
$\tau_{n_{dr}}$	0.09 s	$d_{cell}$	10 $\mu m$
$V_{m_L}$	-25 mV	$V_{PMCA}$	28 $\mu M.s^{-1}$
$k_{m_L}$	12 mV	$K_{PMCA}$	0.08 $\mu M$
$V_{m_T}$	-45 mV	$k_{SERCA}$	0.025 $\mu M.s^{-1}$
$C_m$	0.00314 mF	$Ca_{ER}$	167 $\mu M$

The currents  $I_{K_{dr}}$  and  $I_{K_{ir}}$  are delayed-rectifier and inward-rectifier of  $K^+$ -currents, expressed as

$$\begin{aligned} I_{K_{dr}}(V_m, n_{dr}) &= g_{K_{dr}} n_{dr} (V_m - V_K) \quad \text{and} \\ I_{K_{ir}}(V_m) &= g_{K_{ir}} K_{ir\infty}(V_m) (V_m - V_{K_{ir}}). \end{aligned}$$

The steady-state function for  $I_{K_{ir}}$  is given by

$$K_{ir\infty}(V_m) = \frac{\alpha_{ir}(V_m)}{\alpha_{ir}(V_m) + \beta_{ir}(V_m)},$$

where

$$\begin{aligned} \alpha_{ir}(V_m) &= \frac{0.1}{1 + \exp[0.06(V_m - V_{K_{ir}} - 200)]}, \\ \beta_{ir}(V_m) &= \frac{3 \exp[0.0002(V_m - V_{K_{ir}} + 100)] + \exp[0.1(V_m - V_{K_{ir}} - 10)]}{1 + \exp[-0.5(V_m - V_{K_{ir}})]}. \end{aligned}$$

The currents of the BK channels  $I_{BK_{NEAR}}$  and  $I_{BK_{FAR}}$  are located near and far from the voltage-gated  $Ca^{2+}$ -channels, respectively; they are given by

$$\begin{aligned} I_{BK_{NEAR}}(V_m) &= (1 - b_{BK}) g_{BK_{NEAR}} b_{K_{NEAR\infty}}(V_m) (V_m - V_K) \quad \text{and} \\ I_{BK_{FAR}}(V_m, c) &= (1 - b_{BK}) g_{BK_{FAR}} b_{K_{FAR\infty}}(V_m, c) (V_m - V_K). \end{aligned}$$

The parameter  $b_{BK}$  expresses the fraction of blocked BK channels. The steady-state functions

for these currents are

$$\begin{aligned} b_{K_{NEAR\infty}}(V_m) &= \frac{1}{1 + \exp\left(\frac{-(V_m - V_{BK_{NEAR}}(V_m))}{k_{BK}}\right)} \text{ and} \\ b_{K_{FAR\infty}}(V_m, c) &= \frac{1}{1 + \exp\left(\frac{-(V_m - V_{BK_{FAR}}(c))}{k_{BK}}\right)}, \end{aligned}$$

respectively, where

$$\begin{aligned} V_{BK_{NEAR}}(V_m) &= V_{BK_0} - k_{shift} \ln \frac{Ca_{DOM}(V_m)}{k_{Ca_{BK}}}, \\ V_{BK_{FAR}}(c) &= V_{BK_0} - k_{shift} \ln \frac{c}{k_{Ca_{BK}}} \quad \text{and} \\ Ca_{DOM}(V_m) &= -A(I_{Ca_L}(V_m) + I_{Ca_T}(V_m)). \end{aligned}$$

Finally,  $I_{NS,Na}$  is a non-selective predominantly  $Na^+$ -current, given by

$$I_{NS,Na}(V_m) = g_{NS,Na}(V_m - V_{NS,Na}).$$

The rate of change of the fraction of open delay-rectifier  $K^+$ -channels  $n_{dr}$  follows the dynamics given by Equation (3.2)

$$\frac{dn_{dr}}{dt} = \frac{n_{dr\infty}(V_m) - n_{dr}}{\tau_{n_{dr}}},$$

with the steady-state function defined as

$$n_{dr\infty}(V_m) = \frac{1}{1 + \exp\left(\frac{-(V_m - V_{n_{dr}})}{k_{n_{dr}}}\right)}.$$

The parameter  $\beta$  in Equation (3.3),

$$\begin{aligned} \frac{dc}{dt} &= f\beta(-\alpha(I_{Ca_L}(V_m) + I_{Ca_T}(V_m)) - J_{PMCA}(c)) \\ &\quad + \frac{1}{v_{cell}}(p_{ER}(Ca_{ER}(V_m) - c) - J_{SERCA}(c)), \end{aligned}$$

is the ratio of cell surface area  $A_{cell}$  and volume  $V_{cell}$ , expressed by

$$A_{cell} = \pi d_{cell}^2 \quad \text{and} \quad v_{cell} = \frac{\pi d_{cell}^3}{6},$$

where  $d_{cell}$  is the diameter of the cell. The parameter  $\alpha$  in Equation (3.3) converts the calcium

currents into fluxes and is given by

$$\alpha = \frac{1}{2FA_{\text{cell}}},$$

where  $F$  is Faraday's constant. The individual  $\text{Ca}^{2+}$ -fluxes due to the  $\text{Ca}^{2+}$ -ATP-pumps of the plasma membrane and endoplasmic reticulum (ER) are

$$J_{\text{PMCA}}(c) = V_{\text{PMCA}} \frac{c^2}{c^2 + K_{\text{PMCA}}^2} \quad \text{and} \quad J_{\text{SERCA}}(c) = k_{\text{SERCA}} c.$$

## Bibliography

- P. Andersen, R. Morris, D. Amaral, T. Bliss, and J. O’Keefe. *The hippocampus book*. Oxford University Press, USA, 2007.
- V. I. Arnol’d, V. S. Afraimovich, Y. S. Il’yashenko, and L. P. Shil’nikov. Dynamical Systems V. In R. V. Gamkrelidze, editor, *Encyclopedia of Mathematical Sciences*. Springer-Verlag, New York, NY, 1994.
- S. Baer, T. Erneux, and J. Rinzel. The Slow Passage Through a Hopf Bifurcation: Delay, Memory Effects, and Resonance. *SIAM Journal on Applied Mathematics*, 49(1):55–71, 1989.
- E. Benoît, J.-L. Callot, F. Diener, and M. Diener. Chasse au canard. *Collectanea Mathematica*, 31-32(1-3):37–119, 1981.
- R. Bertram, M. J. Butte, T. Kiemel, and A. Sherman. Topological and phenomenological classification of bursting oscillations. *Bulletin of Mathematical Biology*, 57(3):413–439, 1995.
- T. Blackmer, S. P. Kuo, K. J. Bender, P. F. Apostolides, and L. O. Trussell. Dendritic calcium channels and their activation by synaptic signals in auditory coincidence detector neurons. *Journal of Neurophysiology*, 102(2):1218–26, 2009.
- M. Brøns and K. Bar-Eli. Canard explosion and excitation in a model of the Belousov-Zhabotinskii reaction. *Journal of Physical Chemistry*, 95(22):8706–8713, 1991.
- M. Brøns and K. Bar-Eli. Asymptotic analysis of canards in the EOE equations and the role of the inflection line. *Proceedings of the Royal Society A: Mathematical, Physical and Engineering Sciences*, 445(1924):305–322, 1994.
- J. T. Brown and A. D. Randall. Activity-dependent depression of the spike after-depolarization generates long-lasting intrinsic plasticity in hippocampal CA3 pyramidal neurons. *The Journal of Physiology*, 587(Pt 6):1265–81, 2009.

- J. T. Brown, J. Chin, S. C. Leiser, M. N. Pangalos, and A. D. Randall. Altered intrinsic neuronal excitability and reduced Na(+) currents in a mouse model of Alzheimer's disease. *Neurobiology of Aging*, 2011.
- A. R. Champneys, Y. A. Kuznetsov, and B. Sandstede. HOMCONT: An AUTO86 driver for homoclinic bifurcation analysis (Version 2.0). Technical report, CWI Amsterdam, 1995.
- T. R. Chay and J. Keizer. Minimal model for membrane oscillations in the pancreatic beta-cell. *Biophysical Journal*, 42(2):181–90, 1983.
- S. Chen and Y. Yaari. Spike Ca<sup>2+</sup> influx upmodulates the spike afterdepolarization and bursting via intracellular inhibition of KV7/M channels. *The Journal of Physiology*, 586(5):1351–63, 2008.
- M. Desroches, B. Krauskopf, and H. M. Osinga. The geometry of slow manifolds near a folded node. *SIAM Journal on Applied Dynamical Systems*, 7:1131–1162, 2008a.
- M. Desroches, B. Krauskopf, and H. M. Osinga. Mixed-mode oscillations and slow manifolds in the self-coupled FitzHugh-Nagumo system. *Chaos*, 18(1):015107, 2008b.
- M. Desroches, J. Guckenheimer, B. Krauskopf, C. Kuehn, H. M. Osinga, and M. Wechselberger. Mixed-mode oscillations with multiple time scales. *SIAM Review*, to appear, 2012.
- A. Destexhe and T. Bal. *Dynamic-Clamp: From Principles to Applications*. Springer New York, 2009.
- E. J. Doedel. AUTO: A program for the automatic bifurcation analysis of autonomous systems. *Congressus Numerantium*, 30:265–284, 1981.
- E. J. Doedel. Lecture notes on numerical analysis of nonlinear equations. In *Numerical Continuation Methods for Dynamical Systems*, chapter 1, pages 1–49. Springer, 2007.
- E. J. Doedel and B. E. Oldeman. AUTO-07P: Continuation and bifurcation software for ordinary differential equations, 2009. URL <http://indy.cs.concordia.ca/auto/>.
- R. Douglas, M. Mahowald, and C. Mead. Neuromorphic analogue VLSI. *Annual Review of Neuroscience*, 18:255–81, 1995.
- F. Dumortier. Techniques in the theory of local bifurcations: blow-up, normal forms, nilpotent bifurcations, singular perturbations. In *Bifurcations and Periodic Orbits of Vector Fields*, pages 19–74. Kluwer Academic Publishers, 1993.
- J. Epsztein, M. Brecht, and A. K. Lee. Intracellular determinants of hippocampal CA1 place and silent cell activity in a novel environment. *Neuron*, 70(1):109–20, 2011.

- G. B. Ermentrout. *Simulating, analyzing, and animating dynamical systems: a guide to XPPAUT for researchers and students*. SIAM, 2002.
- G. B. Ermentrout and D. H. Terman. *Mathematical Foundations of Neuroscience*, volume 35 of *Interdisciplinary Applied Mathematics*. Springer, New York, NY, 2010.
- B. Fakler and J. P. Adelman. Control of K(Ca) channels by calcium nano/microdomains. *Neuron*, 59(6):873–81, 2008.
- N. Fenichel. Persistence and smoothness of invariant manifolds for flows. *Indiana University Mathematics Journal*, 21(3):193–226, 1971.
- N. Fenichel. Geometric singular perturbation theory for ordinary differential equations. *Journal of Differential Equations*, 31(1):53–98, 1979.
- R. Fitzhugh. Thresholds and plateaus in the Hodgkin-Huxley nerve equations. *Journal of General Physiology*, 43(5):867, 1960.
- R. Fitzhugh. Impulses and physiological states in theoretical models of nerve membrane. *Bioophysical Journal*, 1(6):445–466, 1961.
- R. M. Ghigliazza and P. J. Holmes. Minimal models of bursting neurons: How multiple currents, conductances, and timescales affect bifurcation diagrams. *SIAM Journal on Applied Dynamical Systems*, 3(4):636, 2004.
- D. Golomb, C. Yue, and Y. Yaari. Contribution of persistent Na<sup>+</sup> current and M-type K<sup>+</sup> current to somatic bursting in CA1 pyramidal cells: combined experimental and modeling study. *Journal of Neurophysiology*, 96(4):1912–26, 2006.
- W. Govaerts and A. Dhooge. Bifurcation, bursting and spike generation in a neural model. *International Journal of Bifurcation and Chaos*, 12(8):1731–1741, 2002.
- N. Gu, K. Vervaeke, H. Hu, and J. F. Storm. Kv7/KCNQ/M and HCN/h, but not KCa2/SK channels, contribute to the somatic medium after-hyperpolarization and excitability control in CA1 hippocampal pyramidal cells. *The Journal of Physiology*, 566(Pt 3):689–715, 2005.
- J. Guckenheimer and K. Hoffman. Numerical computation of canards. *International Journal of Bifurcation and Chaos*, 10(12):2669–2687, 2000.
- J. Guckenheimer and P. Holmes. *Nonlinear Oscillations, Dynamical Systems, and Bifurcations of Vector Fields*. Springer, New York, NY, seventh edition, 2002.
- J. Guckenheimer and C. Kuehn. Computing slow manifolds of saddle type. *SIAM Journal on Applied Dynamical Systems*, 8(3):854, 2009.

- J. Guckenheimer, K. Hoffman, and W. Weckesser. The forced van der Pol equation I: The slow flow and its bifurcations. *SIAM Journal on Applied Dynamical Systems*, 2(1):1, 2003.
- D. Hansel, G. Mato, and C. Meunier. Phase dynamics for weakly coupled Hodgkin-Huxley neurons. *Europhysics Letters*, 23(5):367–372, 1993.
- C. D. Harvey, F. Collman, D. A. Dombeck, and D. W. Tank. Intracellular dynamics of hippocampal place cells during virtual navigation. *Nature*, 461(7266):941, 2009.
- G. Hek. Geometric singular perturbation theory in biological practice. *Journal of Mathematical Biology*, 60(3):347–86, 2010.
- A. L. Hodgkin and A. F. Huxley. A quantitative description of membrane current and its application to conduction and excitation in nerve. *Journal of Physiology*, 105(117):500–544, 1952.
- A. L. Hodgkin, A. F. Huxley, and B. Katz. Measurement of current-voltage relations in the membrane of the giant axon of Loligo. *The Journal of physiology*, 116(4):424–448, 1952.
- J. Hunter. Matplotlib: a 2D graphics environment. *Computing in Science & Engineering*, 2007.
- G. Indiveri, B. Linares-Barranco, T. J. Hamilton, A. van Schaik, R. Etienne-Cummings, T. Delbrück, S.-C. Liu, P. Dudek, P. Häfliger, S. Renaud, J. Schemmel, G. Cauwenberghs, J. Arthur, K. Hynna, F. Folowosele, S. Saighi, T. Serrano-Gotarredona, J. Wijekoon, Y. Wang, and K. Boahen. Neuromorphic silicon neuron circuits. *Frontiers in Neuroscience*, 5:73, 2011.
- E. M. Izhikevich. Neural excitability, spiking and bursting. *International Journal of Bifurcation and Chaos*, 10(6):1171–1266, 2000.
- E. M. Izhikevich. *Dynamical systems in neuroscience: the geometry of excitability and bursting*. The MIT Press, 2006.
- D. B. Jaffe, W. N. Ross, J. E. Lisman, N. Lasser-Ross, H. Miyakawa, and D. Johnston. A model for dendritic Ca<sup>2+</sup> accumulation in hippocampal pyramidal neurons based on fluorescence imaging measurements. *Journal of Neurophysiology*, 71(3):1065–77, 1994.
- C. K. Jones. Geometric singular perturbation theory. In *Dynamical Systems*, volume 1609 of *Lecture Notes in Mathematics*, pages 44–118. Springer Berlin / Heidelberg, 1995.
- E. Jones, T. Oliphant, P. Peterson, et al. SciPy: Open source scientific tools for Python, 2001.  
URL <http://www.scipy.org/>.
- J. P. Keener and J. Sneyd. *Mathematical Physiology: Cellular Physiology*. Springer, New York, NY, second edition, 2009.

- K. B. Kile, N. Tian, and D. M. Durand. Scn2a sodium channel mutation results in hyperexcitability in the hippocampus in vitro. *Epilepsia*, 49(3):488, 2008.
- R. Krahe and F. Gabbiani. Burst firing in sensory systems. *Nature Reviews. Neuroscience*, 5(1):13–23, 2004.
- B. Krauskopf and H. M. Osinga. Computing invariant manifolds via the continuation of orbit segments. In *Numerical Continuation Methods for Dynamical Systems*, pages 117–154. Springer, 2007.
- B. Krauskopf and T. Rieß. A Lin’s method approach to finding and continuing heteroclinic connections involving periodic orbits. *Nonlinearity*, 21(8):1655–1690, 2008.
- B. Krauskopf, K. Schneider, J. Sieber, S. Wieczorek, and M. Wolfrum. Excitability and self-pulsations near homoclinic bifurcations in semiconductor laser systems. *Optics Communications*, 215(4-6):367–379, 2003.
- Y. A. Kuznetsov. *Elements of applied bifurcation theory*, volume 112. Springer-Verlag, New York, second edition, 1998.
- M. T. Lazarewicz, M. Migliore, and G. A. Ascoli. A new bursting model of CA3 pyramidal cell physiology suggests multiple locations for spike initiation. *BioSystems*, 67(1-3):129–137, 2002.
- A. P. LeBeau, A. B. Robson, A. E. McKinnon, and J. Sneyd. Analysis of a reduced model of corticotroph action potentials. *Journal of Theoretical Biology*, 192(3):319–39, 1998.
- A. K. Lee, I. D. Manns, B. Sakmann, and M. Brecht. Whole-cell recordings in freely moving rats. *Neuron*, 51(4):399–407, 2006.
- E. Lee and D. H. Terman. Uniqueness and stability of periodic bursting solutions. *Journal of Differential Equations*, 158(1):48–78, 1999. ISSN 00220396.
- Z. Liu, J. Ren, and T. H. Murphy. Decoding of synaptic voltage waveforms by specific classes of recombinant high-threshold Ca(2+) channels. *Journal of Physiology*, 553(2):473–488, 2003.
- R. R. Llinás. The intrinsic electrophysiological properties of mammalian neurons: insights into central nervous system function. *Science*, 242(4886):1654–1664, 1988.
- S. Martinez-Conde, S. L. Macknik, and D. H. Hubel. The function of bursts of spikes during visual fixation in the awake primate lateral geniculate nucleus and primary visual cortex. *Proceedings of the National Academy of Sciences of the United States of America*, 99(21):13920–5, 2002.

- D. A. McCormick and D. Contreras. On the cellular and network bases of epileptic seizures. *Annual Review of Physiology*, 63(1):815–46, 2001.
- M. Migliore, E. P. Cook, D. B. Jaffe, D. A. Turner, and D. Johnston. Computer simulations of morphologically reconstructed CA3 hippocampal neurons. *Journal of Neurophysiology*, 73 (3):1157–68, 1995.
- S. N. Misra, K. M. Kahlig, and A. L. George. Impaired NaV1.2 function and reduced cell surface expression in benign familial neonatal-infantile seizures. *Epilepsia*, 49(9):1535–45, 2008.
- J. Nagumo and S. Arimoto. An active pulse transmission line simulating nerve axon. *Proceedings of the IRE*, 50(10):2061–2070, 1962.
- B. Naundorf, F. Wolf, and M. Volgushev. Unique features of action potential initiation in cortical neurons. *Nature*, 440(7087):1060–1063, 2006.
- J. Nowacki. XPPy, 2011. URL <http://seis.bris.ac.uk/~enxjn/xppy/>.
- J. Nowacki, S. Mazlan, H. M. Osinga, and K. Tsaneva-Atanasova. The role of large-conductance Calcium-activated K<sup>+</sup> (BK) channels in shaping bursting oscillations of a somatotroph cell model. *Physica D: Nonlinear Phenomena*, 239(9):485–493, 2010.
- J. Nowacki, H. M. Osinga, J. T. Brown, A. D. Randall, and K. Tsaneva-Atanasova. A unified model of CA1/3 pyramidal cells: An investigation into excitability. *Progress in Biophysics and Molecular Biology*, 105(1-2):34–48, 2011a.
- J. Nowacki, H. M. Osinga, and K. Tsaneva-Atanasova. Dynamical systems analysis of spike-adding mechanisms in transient bursts. *Preprint Bristol Centre for Applied Nonlinear Mathematics 1785*, 2011b.
- S. Oldfield, J. Hancock, A. Mason, S. A. Hobson, D. Wynick, E. Kelly, A. D. Randall, and N. V. Marrion. Receptor-mediated suppression of potassium currents requires colocalization within lipid rafts. *Molecular Pharmacology*, 76(6):1279–1289, 2009.
- T. Oliphant. Python for scientific computing. *Computing in Science & Engineering*, 2007.
- H. M. Osinga and K. Tsaneva-Atanasova. Dynamics of plateau bursting depending on the location of its equilibrium. *Journal of Neuroendocrinology*, 22(12):1301–14, 2010.
- J. Rinzel. Bursting oscillations in an excitable membrane model. In B. Sleeman and R. Jarvis, editors, *Ordinary and Partial Differential Equations*, volume 1151 of *Lecture Notes in Mathematics*, pages 304–316. Springer Berlin / Heidelberg, 1985.

- J. Rinzel. A Formal Classification of Bursting Mechanisms in Excitable Systems. In *International Congress of Mathematicians*, pages 1578–1593, 1987.
- J. Rinzel and G. B. Ermentrout. Analysis of Neural Excitability and Oscillations. In C. Koch and I. Segev, editors, *Methods in Neuronal Modelling*, chapter 7, pages 251–292. The MIT Press, 2nd edition, 1998.
- V. F. Safulina, P. Zucchi, M. Taglialetela, Y. Yaari, and E. Cherubini. Low expression of Kv7/M channels facilitates intrinsic and network bursting in the developing rat hippocampus. *Journal of Physiology*, 586(22):5437–53, 2008.
- H. E. Scharfman. Spiny neurons of area CA3c in rat hippocampal slices have similar electrophysiological characteristics and synaptic responses despite morphological variation. *Hippocampus*, 3(1):9–28, 1993.
- A. Shilnikov and M. Kolments. Methods of the quantitative theory for their Hindmarsh-Rose model: A casestudy and a tutorial. *International Journal of Bifurcation and Chaos*, 18(08):2141, 2008.
- P. Smolen, D. H. Terman, and J. Rinzel. Properties of a bursting model with two slow inhibitory variables. *SIAM Journal on Applied Mathematics*, 53(3):861, 1993.
- J. V. Stern, H. M. Osinga, A. LeBeau, and A. Sherman. Resetting behavior in a model of bursting in secretory pituitary cells: distinguishing plateaus from pseudo-plateaus. *Bulletin of Mathematical Biology*, 70(1):68–88, 2008.
- S. S. Stojilkovic, H. Zemkova, and F. V. Goor. Biophysical basis of pituitary cell type-specific Ca<sup>2+</sup> signaling–secretion coupling. *Trends in Endocrinology & Metabolism*, 16(4):152–159, 2005.
- P. Szmolyan and M. Wechselberger. Canards in  $\mathbb{R}^3$ . *Journal of Differential Equations*, 177(2):419–453, 2001.
- J. Tabak, N. Toporikova, M. E. Freeman, and R. Bertram. Low dose of dopamine may stimulate prolactin secretion by increasing fast potassium currents. *Journal of Computational Neuroscience*, 22(2):211–22, 2007.
- D. H. Terman. Chaotic spikes arising from a model of bursting in excitable membranes. *SIAM Journal on Applied Mathematics*, 51(5):1418–1450, 1991.
- D. H. Terman. The transition from bursting to continuous spiking in excitable membrane models. *Journal of Nonlinear Science*, 2(2):135–182, 1992.

- M. J. Thomas, A. M. Watabe, T. D. Moody, M. Makhinson, and T. J. O'Dell. Postsynaptic complex spike bursting enables the induction of LTP by theta frequency synaptic stimulation. *Journal of Neuroscience*, 18(18):7118–26, 1998.
- N. Toporikova, J. Tabak, M. E. Freeman, and R. Bertram. A-type K<sup>+</sup> current can act as a trigger for bursting in the absence of a slow variable. *Neural Computation*, 20(2):436–51, 2008.
- R. D. Traub, R. K. Wong, R. Miles, and H. Michelson. A model of a CA3 hippocampal pyramidal neuron incorporating voltage-clamp data on intrinsic conductances. *Journal of Neurophysiology*, 66(2):635–50, 1991.
- K. Tsaneva-Atanasova, A. Sherman, F. van Goor, and S. S. Stojilkovic. Mechanism of spontaneous and receptor-controlled electrical activity in pituitary somatotrophs: experiments and theory. *Journal of Neurophysiology*, 98(1):131–44, 2007.
- K. Tsaneva-Atanasova, H. M. Osinga, T. Riess, and A. Sherman. Full system bifurcation analysis of endocrine bursting models. *Journal of Theoretical Biology*, 264(4):1133–46, 2010.
- R. A. J. van Elburg and A. van Ooyen. Impact of dendritic size and dendritic topology on burst firing in pyramidal cells. *PLoS Computational Biology*, 6(5):e1000781, 2010.
- F. Van Goor, Y. X. Li, and S. S. Stojilkovic. Paradoxical role of large-conductance calcium-activated K<sup>+</sup> (BK) channels in controlling action potential-driven Ca<sup>2+</sup> entry in anterior pituitary cells. *Journal of Neuroscience*, 21(16):5902–15, 2001a.
- F. Van Goor, D. Zivadinovic, a. J. Martinez-Fuentes, and S. S. Stojilkovic. Dependence of pituitary hormone secretion on the pattern of spontaneous voltage-gated calcium influx. Cell type-specific action potential secretion coupling. *Journal of Biological Chemistry*, 276(36):33840–6, 2001b.
- G. Varoquaux and P. Ramachandran. Mayavi: Making 3D Data Visualization Reusable. In *Proceedings of the 7th Python in Science Conference*, pages 51–56, 2008.
- T. Vo, R. Bertram, J. Tabak, and M. Wechselberger. Mixed mode oscillations as a mechanism for pseudo-plateau bursting. *Journal of Computational Neuroscience*, 28(3):443–58, 2010.
- M. Wechselberger. Existence and bifurcation of canards in  $\mathbb{R}^3$  in the case of a folded node. *SIAM Journal on Applied Dynamical Systems*, 4(1):101, 2005.
- S. Wieczorek, B. Krauskopf, and D. Lenstra. A unifying view of bifurcations in a semiconductor laser subject to optical injection. *Optics Communications*, 172(1-6):279–295, 1999.

- S. Wieczorek, B. Krauskopf, and D. Lenstra. Multipulse excitability in a semiconductor laser with optical injection. *Physical Review Letters*, 88(6):1–4, 2002.
- R. K. Wong and D. A. Prince. Afterpotential generation in hippocampal pyramidal cells. *Journal of Neurophysiology*, 45(1):86–97, 1981.
- J. Xu and C. E. Clancy. Ionic mechanisms of endogenous bursting in CA3 hippocampal pyramidal neurons: A model study. *PLoS ONE*, 3(4), 2008.
- Y. Yaari, C. Yue, and H. Su. Recruitment of apical dendritic T-type Ca<sup>2+</sup> channels by back-propagating spikes underlies de novo intrinsic bursting in hippocampal epileptogenesis. *The Journal of Physiology*, 580(Pt. 2):435–50, 2007.
- C. Yue and Y. Yaari. KCNQ/M channels control spike afterdepolarization and burst generation in hippocampal neurons. *Journal of Neuroscience*, 24(19):4614–4624, 2004.
- C. Yue and Y. Yaari. Axo-somatic and apical dendritic Kv7/M channels differentially regulate the intrinsic excitability of adult rat CA1 pyramidal cells. *Journal of Neurophysiology*, 95(6):3480–95, 2006.
- C. Yue, S. Remy, H. Su, H. Beck, and Y. Yaari. Proximal persistent Na<sup>+</sup> channels drive spike afterdepolarizations and associated bursting in adult CA1 pyramidal cells. *Journal of Neuroscience*, 25(42):9704, 2005.

